Spectroscopic Characterization of Icy Moon Surfaces: Compositions, Origins, and Implications from Jupiter to Neptune

Thesis by
M. Ryleigh Davis

In Partial Fulfillment of the Requirements for the
Degree of
Doctor of Philosophy in Planetary Science

CALIFORNIA INSTITUTE OF TECHNOLOGY
Pasadena, California

2026
Defended April 17, 2026

© 2026

M. Ryleigh Davis
ORCID: 0000-0002-7451-4704

All rights reserved

ACKNOWLEDGEMENTS

Thank you to my advisor, Mike Brown, who has been an incredible mentor these past 5 years. His support and guidance have shaped me as a scientist. Mike has a way of getting to the heart of a problem quickly, and working with him has changed how I think about and approach scientific questions. I am especially grateful for his encouragement of independent and critical thinking, which pushed me to develop both confidence and appropriate skepticism in my own ideas. I deeply appreciate his support when I became a mother during graduate school and as I learned to balance research and family.

I am deeply grateful to Samantha Trumbo for her mentorship, collaboration, and friendship. Sam has had a lasting impact on how I approach science. Although we have not often worked together in person, I have always valued our long conversations at conferences, which have influenced both my research and my broader perspective on this field.

I would like to thank my committee members, Katherine de Kleer, Geoff Blake, and Konstantin Batygin, for their time, feedback, and support. I am also very grateful to Bethany Ehlmann, who served on my committee for most of my Ph.D. and was incredibly generous with her time and advice. I would also like to thank George Rossman for his help and mentorship as I learned mineral spectroscopy. George was always kind, patient, and a true fountain of knowledge, and I feel very grateful to have had the chance to learn from him. He will be greatly missed.

I am thankful for my collaborators and fellow graduate students, who made this experience both intellectually rewarding and genuinely enjoyable. In particular, I would like to thank Abby Keebler for countless coffee runs, work sessions, and weekend adventures with Sophie and I, and for being such a supportive and reliable friend. I am especially grateful to Matthew Belyakov, who has been a close friend, collaborator, and constant source of ideas. Working together—whether developing proposals or talking through ideas and results in the office—has pushed me to think more broadly and has made my science better. I would also like to thank the rest of my research group—William Denman, Matthew Belyakov, Ashma Pandya, Merritt McDowell, Swaroop Chandra, and Kevin Trinh—for many helpful discussions and for making the group such a great place to work.

I am also grateful to my cohort and office mates over the years. Julie Inglis was a

great friend from the very beginning, and I am thankful we went through classes and quals together. I would also like to thank my early office mates—Julie Inglis, Mike McKeon, Nicole Wallack, and Shreyas Vissapragada—and my later office mates—Matthew Belyakov, Merritt McDowell, and Ashma Pandya—for making the office such an enjoyable place to spend long days. Thank you to Maria Camarca and Audrey Martin for always being up for conversations about science, and more broadly, the planetary science graduate student community for creating such a supportive and collaborative environment.

I would also like to thank the Planetary Science administrative staff who keep everything running. In particular, Ruth Loisel and Rachael Danyew were incredibly helpful as the primary administrative support for Mike's group during my time at Caltech, and I am very grateful for everything they did for us. I also thank the GPS department staff, especially Julie Lee, for their support throughout my Ph.D.

I am deeply grateful to my family for their constant support. I would like to thank my mom, Sharri Fitzpatrick, who has gone above and beyond in helping me balance research and parenting. Whether it was coming out for extended visits, watching Sophie while I traveled, or dropping everything to help when things became overwhelming, her support has made an enormous difference. I would also like to thank my dad, Edward Fitzpatrick, for his support throughout my life.

Finally, I want to thank my husband, Erik, for his unwavering support and partnership through everything, and for taking on so much during the busiest parts of my Ph.D. He has been a constant source of stability and encouragement, an incredible father to Sophie, and a true partner—making it possible for me to be both a mom and a graduate student. I truly could not have done this without him. And to my daughter, Sophie—who just turned two—thank you for bringing so much joy, perspective, and balance into my life. You have made these years far more meaningful. I would also like to thank our two cats—Phoebe for her chaos and personality, and Jeffrey for always being there when I needed a snuggle.

ABSTRACT

The surfaces of icy satellites preserve a complex record of the processes that shape their formation and evolution, reflecting a combination of endogenic emplacement, exogenic delivery, and irradiation-driven modification. In this thesis, I use multi-wavelength spectroscopy to disentangle these competing processes and assess the extent to which surface compositions can be used to infer interior chemistry and system history across the outer solar system, from Jupiter to Neptune.

Chapters 2 and 3 focus on Europa, whose surface may provide a window to the subsurface ocean composition, but is strongly altered by irradiation. Using VLT/SINFONI observations, I show that a 2.07 μm absorption feature on Europa's trailing hemisphere correlates with irradiation patterns but not with large-scale geology, indicating a predominantly exogenic origin and challenging models that invoke radiolytically altered ocean-derived salts to explain this band. I then use Galileo/NIMS observations of the young Pwyll and Manann'an craters to constrain the equilibrium timescale of Europa's radiolytic sulfur cycle, finding that hydrated sulfuric acid is depleted in these regions and that equilibrium is reached on timescales $\gtrsim$2–4 Myr—orders of magnitude longer than laboratory estimates.

In Chapter 4, I present near-global ultraviolet–visible spectral mapping of Callisto with HST/STIS. These data reveal absorptions plausibly associated with iron-bearing silicates, organics, and potentially NaCl, and show little evidence for SO_2 or other sulfur-bearing species. The spatial distribution of these spectral features reveals significant compositional heterogeneity, including localized features associated with major impact basins, challenging suggestions that Callisto's dark material is dominated by a thick (~100 m) blanket of irregular satellite dust. Instead, these observations indicate that the dark material reflects a complex mixture of endogenic material excavated by impacts, delivered exogenic material, and radiolytic alteration.

In Chapter 5, I use JWST/NIRSpec observations to show that Neptune's ring-moons exhibit a 2.72 μm absorption diagnostic of Mg-phyllosilicates, indicating extensive aqueous alteration within larger precursor bodies. These results suggest that Neptune's present-day moons are reaccreted fragments of differentiated satellites disrupted during Triton's capture, providing direct access to deep interior material from icy outer solar system bodies.

PUBLISHED CONTENT AND CONTRIBUTIONS

Davis, M. R., M. Belyakov, I. Wong, Z. Milby, and M. E. Brown (2026). "Triton's Wake: Neptune's Shattered Inner Moons Reveal Icy Body Interior Compositions". Submitted to *Science Advances*.
M.R.D. helped conceive of the project, performed the analysis, led the interpretation, and wrote the manuscript.

Davis, M. R., S. K. Trumbo, M. E. Brown, and M. Belyakov (2025). "Spectroscopic Mapping of Callisto with HST/STIS and Implications for Its Surface Composition". *The Planetary Science Journal* 6.7, p. 161. DOI: 10.3847/PSJ/addec7.
M.R.D. influenced the direction of the project, performed the data reduction and analysis, interpreted the results, and wrote the manuscript.

Davis, M. R. and M. E. Brown (2024). "Pwyll and Manannán Craters as a Laboratory for Constraining Irradiation Timescales on Europa". *The Planetary Science Journal* 5.5, p. 107. DOI: 10.3847/PSJ/ad3944.
M.R.D. helped conceive of the project, performed the data reduction and analysis, interpreted the results, and wrote the manuscript.

Davis, M. R., M. E. Brown, and S. K. Trumbo (2023). "The Spatial Distribution of the Unidentified 2.07 μm Absorption Feature on Europa and Implications for Its Origin". *The Planetary Science Journal* 4.8, p. 148. DOI: 10.3847/PSJ/aced96.
M.R.D. influenced the direction of the project, performed the data reduction and analysis, interpreted the results, and wrote the manuscript.

TABLE OF CONTENTS

Acknowledgements iii
Abstract v
Published Content and Contributions vi
Table of Contents vi
List of Illustrations ix
List of Tables xii
Chapter I: Introduction 1
Chapter II: The Spatial Distribution of the Unidentified 2.07 μm Absorption Feature on Europa and Implications for its Origin 9
2.1 Introduction 10
2.2 Observations and Data Reduction 13
2.3 Spatial Distribution 16
2.4 Discussion 23
2.5 Conclusions 27
Chapter III: Pwyll and Manannán Craters as a Laboratory for Constraining Irradiation Timescales on Europa 33
3.1 Introduction 34
3.2 Data Analysis 37
3.3 Results 41
3.4 Discussion 47
3.5 Conclusions 52
Chapter IV: Spectroscopic Mapping of Callisto with HST/STIS and Implications for Its Surface Composition 57
4.1 Introduction 58
4.2 Observations and Data Reduction 60
4.3 Definition of Spectral Features 63
4.4 Spectral Maps 65
4.5 Comparison of Spectral Features to Laboratory Spectra 79
4.6 Implications for Callisto's Surface Composition 97
4.7 Comparison Between Galilean Satellites 103
4.8 Conclusions 107
Chapter V: Triton's Wake: Neptune's Shattered Inner Moons Reveal Icy Body Interior Compositions 120
5.1 Introduction 121
5.2 Observations and Data Reduction 122
5.3 Composition 125
5.4 Origin of the Phyllosilicates 128
5.5 Implications for the Proto-Neptunian System 130
5.6 Implications for Outer Solar System Icy Satellites 130

Chapter VI: Conclusions and Future Directions 140

LIST OF ILLUSTRATIONS

Number *Page*

2.1 VLT/SINFONI near-infrared spectra of Europa's leading and trailing hemispheres showing the 2.07 μm absorption feature present only on the trailing hemisphere. 15

2.2 Map of Europa's trailing hemisphere with four example "rings of constant radiolysis," along with summed spectra and continuum-removed 2.07 μm absorptions by geologic unit for each ring. The absorption depth shows no difference between chaos terrains and ridged plains, but is absent from Pwyll crater and its ejecta. 19

2.3 Trailing hemisphere irradiation patterns and measured 2.07 μm band areas by geologic unit and chaos sub-type for 29 rings of constant radiolysis. No measurable difference in band area is found between chaos terrains and ridged plains; the feature is absent from Pwyll crater. 21

3.1 Global mosaic of Europa showing the locations of Pwyll and Manannán craters, their ejecta systems, and the trailing hemisphere apex. . 35

3.2 Galileo/SSI images of Pwyll and Manannán craters showing their dark proximal ejecta, bright ray ejecta blankets, and surrounding terrain. 36

3.3 Average Galileo/NIMS spectra and best-fit linear spectral models for Pwyll and Manannán craters. 42

3.4 Best-fit spectral model abundance values for sulfuric acid, salts, and water-ice at Pwyll and Manannán craters on Europa, showing depletion in sulfuric acid and enrichment in salts at both craters relative to older terrain. 44

3.5 Sulfuric acid, salt, and water-ice abundance maps from Galileo/NIMS linear spectral modeling for Pwyll and Manannán craters and surrounding terrain. Both craters are depleted in sulfuric acid and the dark proximal ejecta is enriched in salts relative to the bright ray ejecta. 45

4.1 Example HST/STIS spectra from 200 to 1000 nm of representative regions on Callisto's surface, with zoom-ins of individual spectral features. 64

4.2 Maps of Callisto's bolometric albedo and strength of the near-UV downturn (via the 360–410 nm slope), with scatter plots showing their correlation on the leading and trailing hemispheres. 68
4.3 Map of Callisto's NIR spectral slope (700–1000 nm) and scatter plots showing its strong negative correlation with albedo. 70
4.5 Map of the combined 820 and 930 nm absorption band area on Callisto, with scatter plots demonstrating that there is no notable correlation with the relative albedo of the dark material. The combined bands are spatially associated with the Valhalla and Asgard impact basins. 72
4.6 Map of the 320 nm absorption band area on Callisto, showing it is largely constrained to the Asgard and Valhalla impact basin regions on the leading hemisphere. 73
4.7 Maps of two proxies for the 275 nm absorption edge strength on Callisto: the 230–270 nm slope and the integrated band area after dividing by a reference spectrum. The feature is confined to the trailing hemisphere. 76
4.8 Map of the 280 nm ratio feature band area on Callisto, showing it is constrained to the leading hemisphere and strongly anti-correlated with the 275 nm edge and correlated with the 320 nm band. 77
4.9 Comparison of select Callisto HST/STIS spectra with laboratory spectra, showing continuum-removed absorption features at 230, 320, 450, 820, and 930 nm alongside candidate mineral and organic species. 80
4.10 Comparison of Callisto's 280 nm ratio feature with those of Europa and Ganymede, and demonstration that the feature arises from dividing the 320 nm leading hemisphere band by the trailing hemisphere 275 nm absorption edge. No contribution from SO_2 or O_3 is required. 93
4.11 Comparison of HST/STIS UV and visible spectra of the leading and trailing hemispheres of Callisto, Ganymede, and Europa, and a patch of bright material on Io, normalized at 1000 nm. 104
5.1 Representative JWST/NIRSpec IFU images of Larissa showing the locations of Neptune's rings. 124
5.2 JWST/NIRSpec spectra of Neptune's inner moons and rings, revealing a unique 2.72 μm phyllosilicate absorption, with comparison to CM chondrite and asteroid spectra. 127

5.3 Comparison of Proteus' 3 μm OH band with other outer solar system objects lacking clear water-ice overtones, demonstrating its outlier status. 132

LIST OF TABLES

Number *Page*

3.1 Laboratory spectra used in the linear spectral modeling analysis, based on the spectral library of King et al. (2022). 39

3.2 Best-fit spectral modeling abundances for Pwyll and Manannán crater regions with 1σ confidence intervals. 43

4.1 HST/STIS observation details for Callisto spectroscopic mapping program. 61

5.1 JWST NIRSpec/IFU observation details for Neptune's ring-moons, program #4645. 123

Chapter 1

INTRODUCTION

The discovery of Jupiter's four largest moons by Galileo Galilei in 1610 marked a turning point in the history of astronomy. In *Sidereus Nuncius*, Galileo described a set of "stars" near Jupiter whose positions changed from night to night, leading him to conclude that they were not fixed stars, but bodies in orbit around the planet (Galileo, 1610). These objects—Io, Europa, Ganymede, and Callisto—provided the first clear example of one celestial body orbiting another, offering strong support for the Copernican view that not everything in the heavens revolves around the Earth. In the decades following Galileo's discoveries, the recognition that giant planets host their own satellite systems quickly extended beyond Jupiter. Additional moons were identified around Saturn, beginning with Titan by Huygens in 1655 and several others discovered by Cassini in the late 17th century. The large moons of Uranus were discovered in the late 18th and 19th centuries by Sir William Herschel and William Lassell. Around Neptune, Triton was discovered shortly after the planet itself in 1846, though its retrograde orbit hinted early on at a distinct origin compared to the regular satellite systems of the other giant planets (Débarbat, 1997; McKinnon et al., 2014).

In the centuries since, we have begun to understand the stunning diversity of these complex worlds, each with distinct geologic histories and surface compositions. Spacecraft observations in the late 20th and early 21st centuries—most notably by the *Voyager* missions, the *Galileo* spacecraft, and the *Cassini* mission—revealed an extraordinary diversity among these worlds, from Io's active volcanism to the ancient, heavily cratered surface of Callisto, and the geologically active, ocean-bearing environments of moons such as Enceladus and Europa (e.g. Carr et al., 1998; Greeley et al., 2000; Hansen et al., 2006; McEwen et al., 1998). Indeed, a remarkable number of the outer solar systems icy moons are now thought to be "ocean worlds," hosting subsurface oceans beneath their icy shells that make them prime targets in the search for habitable environments and hinting at complex dynamical histories that challenge our understanding of planet formation and evolution (Nimmo et al., 2016).

Spacecraft measurements—including magnetometer detections of induced magnetic

fields and gravity constraints on internal structure—have provided strong evidence for subsurface oceans and differentiated interiors on several moons (e.g. Anderson et al., 1998a,b; Kivelson et al., 2000). However, these measurements provide only bulk constraints on interior properties, and the detailed structures, compositions and chemistries of these interiors are largely inferred from models. Because we cannot directly access their interiors, we must instead rely on the surfaces of these moons as observable records of their internal composition and chemistry, geologic evolution, and formation history. For ocean worlds like Europa, surface materials may provide one of the only accessible windows into the subsurface ocean composition, while for more ancient and geologically inactive bodies such as Callisto, the surface may preserve a record of its early formation and evolution.

However, interpreting what icy satellite surfaces are actually telling us about their interior chemistry or history remains a central challenge. Spectroscopic observations from ultraviolet through infrared wavelengths have revealed a wide diversity of materials on icy satellite surfaces, including water ice, salts, radiolytic products, organics, and silicates (e.g. Brown et al., 2013; Carlson et al., 1999a; Clark et al., 2012, 1980; Dalton et al., 2012; McCord et al., 1997, 1998; Trumbo et al., 2019). However, these materials are often spatially heterogeneous, reflecting both local geologic processes and modification by external (or exogenic) environments (e.g. Bottke et al., 2013; Dalton et al., 2012; Trumbo et al., 2020). For satellites embedded within strong magnetospheric plasma environments, such as Jupiter's Galilean moons, energetic particles deliver new materials and drive extensive chemical alteration, producing species that may not directly reflect their original composition (e.g. Carlson et al., 2002; Cooper et al., 2001; Paranicas et al., 2009). At the same time, impacts and dust delivery bring new exogenic materials and can redistribute material across the surface (e.g. Bottke et al., 2013; Buratti, 1991). As a result, the observed surface composition of even the most geologically active icy satellite is rarely a simple reflection of its interior, but instead represents the integrated outcome of multiple processes operating over a wide range of spatial and temporal scales. Disentangling these competing contributions is essential for interpreting spectroscopic observations and for assessing the extent to which surface compositions can be used to infer interior chemistry, geologic history, and system evolution.

In this thesis, I use multi-wavelength spectroscopic observations from HST, JWST, Galileo/NIMS, and ground-based facilities to investigate how endogenic emplacement, exogenic delivery, and irradiation-driven chemistry shape the observable

surfaces of icy satellites from Jupiter to Neptune. A major theme of this work is not only to identify surface compositions, but to determine how those compositions are produced and modified, and to assess the extent to which they can be used to infer interior properties and system histories.

The first part of this thesis focuses on Europa, where the presence of a subsurface ocean and evidence for recent geologic activity make it a key target for understanding the link between surface composition and interior processes. Beneath its icy shell, Europa's deep global salty ocean is likely in contact with a silicate seafloor, making it one of the most compelling targets for assessing habitability in the outer Solar System (Anderson et al., 1998a; Hand et al., 2009; Kivelson et al., 2000). Our best opportunity to constrain the chemistry of that ocean is through the composition of the surface, particularly in geologically disrupted regions such as chaos terrains, bands, and ridges, where oceanic material may have been directly emplaced (e.g. Collins et al., 2009; Dalton et al., 2012; Greenberg et al., 1999). However, Europa's surface is also strongly modified by exogenic sulfur implantation and irradiation by energetic particles trapped in Jupiter's magnetosphere, especially on the trailing hemisphere (Cooper et al., 2001; Paranicas et al., 2009, 2002). These processes drive a radiolytic sulfur cycle that produces hydrated sulfuric acid and other altered species, overprinting or transforming pre-existing surface material (e.g. Carlson et al., 2002, 2005, 1999b). Distinguishing between endogenic materials that may reflect ocean composition and irradiation products that formed at the surface is therefore one of the central challenges in interpreting Europa's spectroscopy.

In Chapter 2, I investigate the spatial distribution of a weak 2.07 μm absorption feature on Europa's trailing hemisphere using VLT/SINFONI observations. Previous studies have suggested that this feature may arise from radiolytic processing of ocean-derived salts, implying a connection to interior composition and specifically the presence of $MgCl_2$ salts within the ocean (Brown et al., 2013; Ligier et al., 2016). However, by mapping the distribution of this feature and comparing it to both irradiation patterns and geologic units, I show that it is strongly correlated with irradiation but not with large-scale geology, indicating a predominantly exogenic origin and challenging interpretations that link it to the ocean chemistry.

In Chapter 3, I further investigate irradiation processes on Europa by using the young impact craters Pwyll and Manannán as natural laboratories for constraining radiolytic timescales. Using Galileo/NIMS observations, I show that both craters and their ejecta—which expose relatively fresh material from the subsurface—are

depleted in hydrated sulfuric acid relative to nearby older terrain. This suggests that the radiolytic sulfur cycle has not yet reached equilibrium in these regions and places a lower limit on the equilibrium timescale of the sulfur cycle of $\gtrsim$2–4 Myr—several orders of magnitude longer than prevous estimates based on laboratory experiments. At the same time, the presence of irradiation-darkened salts in the crater centers suggests that some alteration processes operate on significantly shorter timescales.

In Chapter 4, I shift focus to Callisto, whose surface shows little evidence for past geologic processing and instead preserves an ancient, heavily cratered record almost as old as the solar system (~4-4.5 Ga) (Bottke et al., 2024; Greeley et al., 2000; Moore et al., 2004). As the only Galilean satellite which may not have a fully differentiated interior, Callisto may offer one of our best windows into the composition of the proto-Jovian disk—the formation environment of the Galilean satellites (Anderson et al., 1998b). However, interpreting that primordial record requires separating the cumulative effects of 4.5 billion years of impact excavation, sublimation-driven landscape modification, irradiation, and exogenic material delivery. It has been proposed that the non-ice material on Callisto's surface may be entirely dominated by a thick ($\gtrsim$100 m) global layer of exogenic dust derived from irregular satellites and deposited over geologic timescales (Bottke et al., 2013). In this scenario, the observed surface composition would largely reflect externally delivered material, obscuring any direct signature of endogenic or primordial components. Distinguishing between this exogenic-dominated model and one in which impact excavation exposes native, potentially primordial, material is therefore critical for assessing whether Callisto's surface can be used to probe its formation environment.

Using near-global ultraviolet–visible spectral mapping with HST/STIS, I identify multiple absorption features, map their spatial distributions across the surface, and discuss the implications for the composition of Callisto's surface. These data reveal significant compositional heterogeneity, including localized features associated with major impact basins such as Asgard and Valhalla. Importantly, the observed spectral variations are inconsistent with models in which Callisto's dark material is dominated by a uniform layer of irregular satellite dust. Instead, the data support a model in which the dark material is a complex mixture of endogenic material excavated by impacts, delivered exogenic material, and irradiation products—with the relative contributions varying regionally.

In Chapter 5, I extend this analysis to the Neptune system, where the relationship

between surface composition and system history may be fundamentally different from that of the Jovian satellites. Neptune's satellite system is dominated by Triton, whose retrograde orbit indicates that it was captured from the Kuiper Belt, rather than formed in place. Dynamical models suggest that Triton's capture would have disrupted any pre-existing system of regular satellites, potentially generating a debris disk from which the present-day inner moons reaccreted (e.g. Ćuk et al., 2005; Goldreich et al., 1989; Rufu et al., 2017). Using JWST/NIRSpec observations of Proteus, Larissa, and Galatea, I identify a distinct 2.72 μm absorption feature diagnostic of Mg-rich phyllosilicates. The presence of these minerals is an exciting surprise, as given the small sizes and cold surface environments of the present-day moons, these materials cannot have formed in situ, implying that they originated in larger differentiated satellites that were subsequently disrupted. These results support a scenario in which Neptune's current inner moons are reaccreted fragments of a previously existing satellite system that was destroyed during Triton's capture. This means that Neptune's ring-moons may be the only place in the solar system with direct access to deep interior material sourced directly from (a) differentiated icy moon(s).

BIBLIOGRAPHY

Anderson, J. D. et al. (1998a). "Europa's Differentiated Internal Structure: Inferences from Four Galileo Encounters". *Science* 281.5385, pp. 2019–2022.

– (1998b). "Distribution of rock, metals, and ices in Callisto". *Science* 280.5369, pp. 1573–1576.

Bottke, W. F. et al. (2024). "The Bombardment History of the Giant Planet Satellites". *The Planetary Science Journal* 5.4, p. 88.

Bottke, W. F. et al. (2013). "Black Rain: The Burial of the Galilean Satellites in Irregular Satellite Debris". *Icarus* 223.2, pp. 775–795.

Brown, M. E. and K. P. Hand (2013). "Salts and Radiation Products on the Surface of Europa". *The Astronomical Journal* 145.4, p. 110.

Buratti, B. J. (1991). "Ganymede and Callisto: Surface Textural Dichotomies and Photometric Analysis". *Icarus* 92.2, pp. 312–323.

Carlson, R. W. et al. (2002). "Sulfuric Acid Production on Europa: The Radiolysis of Sulfur in Water Ice". *Icarus* 157.2, pp. 456–463.

Carlson, R. W. et al. (1999a). "Hydrogen Peroxide on the Surface of Europa". *Science* 283.5410, pp. 2062–2064.

Carlson, R. W. et al. (2005). "Distribution of Hydrate on Europa: Further Evidence for Sulfuric Acid Hydrate". *Icarus* 177.2, pp. 461–471.

Carlson, R. W., R. E. Johnson, and M. S. Anderson (1999b). "Sulfuric Acid on Europa and the Radiolytic Sulfur Cycle". *Science* 286.5437, pp. 97–99.

Carr, M. H. et al. (1998). "Evidence for a Subsurface Ocean on Europa". *Nature* 391.6665, pp. 363–365.

Clark, R. N. et al. (2012). "The Surface Composition of Iapetus: Mapping Results from Cassini VIMS". *Icarus* 218.2, pp. 831–860.

Clark, R. N. and T. B. McCord (1980). "The Galilean Satellites: New Near-Infrared Spectral Reflectance Measurements (0.65–2.5 μm) and a 0.325–5 μm Summary". *Icarus* 41.3, pp. 323–339.

Collins, G. and F. Nimmo (2009). "Chaotic Terrain on Europa". *Europa*. Ed. by R. T. Pappalardo, W. B. McKinnon, and K. Khurana. University of Arizona Press, Tucson AZ, pp. 259–281.

Cooper, J. F. et al. (2001). "Energetic Ion and Electron Irradiation of the Icy Galilean Satellites". *Icarus* 149.1, pp. 133–159.

Ćuk, M. and B. J. Gladman (2005). "Constraints on the Orbital Evolution of Triton". *The Astrophysical Journal* 626.2, p. L113.

Dalton, J. B., J. H. Shirley, and L. W. Kamp (2012). "Europa's Icy Bright Plains and Dark Linea: Exogenic and Endogenic Contributions to Composition and Surface Properties". *Journal of Geophysical Research: Planets* 117.E3.

Débarbat, S. (1997). "Discoveries in the Solar System". *International Astronomical Union Colloquium*. Vol. 165. Cambridge University Press, pp. 133–140.

Galileo, G. (1610). "Siderius Nuncius". Ed. by H. Shapley and H. E. Howarth.

Goldreich, P. et al. (1989). "Neptune's Story". *Science* 245.4917, pp. 500–504.

Greeley, R., J. E. Klemaszewski, and R. Wagner (2000). "Galileo Views of the Geology of Callisto". *Planetary and Space Science* 48.9, pp. 829–853.

Greenberg, R. et al. (1999). "Chaos on Europa". *Icarus* 141.2, pp. 263–286.

Hand, K. P. et al. (2009). "Astrobiology and the Potential for Life on Europa". *Europa*. Ed. by R. T. Pappalardo, W. B. McKinnon, and K. Khurana. University of Arizona Press, Tucson AZ, pp. 589–629.

Hansen, C. J. et al. (2006). "Enceladus' water vapor plume". *Science* 311.5766, pp. 1422–1425.

Kivelson, M. G. et al. (2000). "Galileo Magnetometer Measurements: A Stronger Case for a Subsurface Ocean at Europa". *Science* 289.5483, pp. 1340–1343.

Ligier, N. et al. (2016). "VLT/SINFONI Observations of Europa: New Insights into the Surface Composition". *The Astronomical Journal* 151.6, p. 163.

McCord, T. B. et al. (1997). "Organics and Other Molecules in the Surfaces of Callisto and Ganymede". *Science* 278.5336, pp. 271–275.

McCord, T. B. et al. (1998). "Non-Water-Ice Constituents in the Surface Material of the Icy Galilean Satellites from the Galileo near-Infrared Mapping Spectrometer Investigation". *Journal of Geophysical Research: Planets* 103.E4, pp. 8603–8626.

McEwen, A. S. et al. (1998). "Active volcanism on Io as seen by Galileo SSI". *Icarus* 135.1, pp. 181–219.

McKinnon, W. B. and R. L. Kirk (2014). "Triton". *Encyclopedia of the solar system*. Elsevier, pp. 861–881.

Moore, J. M. et al. (2004). "Callisto". *Jupiter: The Planet, Satellites and Magnetosphere*. Ed. by F. Bagenal, T. E. Dowling, and W. B. McKinnon. Cambridge University Press, pp. 397–426.

Nimmo, F. and R. T. Pappalardo (2016). "Ocean worlds in the outer solar system". *Journal of Geophysical Research: Planets* 121.8, pp. 1378–1399.

Paranicas, C. et al. (2009). "Europa's Radiation Environment and Its Effects on the Surface". *Europa*. Ed. by R. T. Pappalardo, W. B. McKinnon, and K. Khurana. University of Arizona Press, Tucson AZ, p. 529.

Paranicas, C. et al. (2002). “The Ion Environment near Europa and Its Role in Surface Energetics”. *Geophysical Research Letters* 29.5, pp. 18-1–18-4.

Rufu, R. and R. M. Canup (2017). “Triton’s Evolution with a Primordial Neptunian Satellite System”. *The Astronomical Journal* 154.5, p. 208.

Trumbo, S. K., M. E. Brown, and K. P. Hand (2019). “Sodium Chloride on the Surface of Europa”. *Science Advances* 5.6, eaaw7123.

– (2020). “Endogenic and Exogenic Contributions to Visible-Wavelength Spectra of Europa’s Trailing Hemisphere”. *The Astronomical Journal* 160.6, p. 282.

Chapter 2

THE SPATIAL DISTRIBUTION OF THE UNIDENTIFIED 2.07 μm ABSORPTION FEATURE ON EUROPA AND IMPLICATIONS FOR ITS ORIGIN

Davis, M. R., M. E. Brown, and S. K. Trumbo (2023). "The Spatial Distribution of the Unidentified 2.07 μm Absorption Feature on Europa and Implications for Its Origin". *The Planetary Science Journal* 4.8, p. 148.

Abstract

A weak absorption feature at 2.07 μm on Europa's trailing hemisphere has been suggested to arise from radiolytic processing of an endogenic salt, possibly sourced from the interior ocean. However, if the genesis of this feature requires endogenic material to be present, one might expect to find a correlation between its spatial distribution and the recently disrupted chaos terrains. Using archived near-infrared observations from Very Large Telescope/SINFONI with a ~1 nm spectral resolution and a linear spatial resolution ~130 km, we examine the spatial distribution of this feature in an effort to explore this endogenic formation hypothesis. We find that while the presence of the 2.07 μm feature is strongly associated with the irradiation pattern on Europa's trailing hemisphere, there is no apparent association between the presence or depth of the absorption feature and Europa's large-scale chaos terrain. This spatial distribution suggests that the formation pathway of the 2.07 μm feature on Europa is independent of any endogenous salts within the recent geology. Instead, we propose that the source of this feature may simply be a product of the radiolytic sulfur cycle or arise from some unidentified parallel irradiation process. Notably, the 2.07 μm absorption band is absent from the Pwyll crater ejecta blanket, suggesting that radiolytic processing has not had enough time to form the species responsible and placing a lower limit on the irradiation timescale. We are unable to find a plausible spectral match to the 2.07 μm feature within the available laboratory data.

2.1 Introduction

Beneath its icy shell, Jupiter's moon Europa hosts a deep global salty ocean that is likely in direct contact with the silicate mantle. When combined with a possible supply of radiolytically produced oxidants from the surface, this water-rock interaction makes Europa a prime target for astrobiological consideration (e.g. Anderson et al., 1998; Chyba, 2000; Hand et al., 2009; Kivelson et al., 2000). Our current best window into Europa's largely unconstrained ocean chemistry is through the surface composition. Specifically, the recently geologically active chaos terrains, bands, and ridges show clear spectroscopic evidence for the presence of salt hydrates that are likely sourced from the subsurface ocean (e.g. Dalton et al., 2005; Johnson et al., 2002; Leblanc et al., 2002; McCord et al., 1999; Shirley et al., 2010; Trumbo et al., 2019b, 2020). These large scale chaos terrains, characterized by polygonal iceberg like blocks of ice within a matrix (Carr et al., 1998), are interpreted to be areas of focused heat flow and possibly local melting which may have exposed oceanic material (e.g Collins et al., 2009; Greenberg et al., 1999). However, exogenic sulfur ions from Io's volcanoes are continuously deposited onto Europa's trailing hemisphere, and bombardment by magnetospheric ions, protons, and electrons (Cooper et al., 2001; Paranicas et al., 2001, 2009; Pospieszalska et al., 1989) drives a radiolytic sulfur cycle. This cycle chemically alters the surface composition and creates a "bull's-eye" pattern of hydrated sulfuric acid centered at the trailing hemisphere apex (270°W, 0°N) (Carlson et al., 2002, 2005, 1999). Understanding the source and nature of exogenic material and radiolytic processing on Europa's surface and disentangling the original state of the endogenic material is therefore critical for interpreting Europa's surface composition and inferring the properties of its underlying ocean.

Europa's surface composition includes crystalline and amorphous water ice (Hansen et al., 2004), radiolytically produced hydrated sulfuric acid on the trailing hemisphere (Carlson et al., 2005, 1999), and an additional hydrated salt component that is largely constrained to the recently geologically active chaos terrains, bands, and ridges (Dalton et al., 2005, 2012; McCord et al., 1999). The distribution of this additional salt hydrate is consistent with Europa's recent geologic features containing endogenic material sourced from the subsurface. Irradiation produced O_2 and hydrogen peroxide (H_2O_2) (Johnson et al., 2003; Loeffler et al., 2006; Trumbo et al., 2019a) as well as CO_2 (Carlson et al., 2009; Hansen et al., 2008; McCord et al., 1998) have also been confirmed on Europa's surface. Recent observations with HST/STIS revealed the presence of absorption features at 230 and 450 nm, spatially

constrained to the leading hemisphere chaos terrains (Trumbo et al., 2022, 2019b), which closely match color center features produced in laboratory data of irradiated sodium chloride (NaCl) (Brown et al., 2022; Denman et al., 2022; Hand et al., 2015). Together, these results provide strong evidence for the presence of endogenous NaCl in Europa's leading hemisphere chaos.

Additional endogenic salt species, which are spectroscopically distinct from the hydrated sulfuric acid, may also exist within Europa's chaos terrains (e.g. Fischer et al., 2015; Trumbo et al., 2020), however their precise nature is widely debated. Some analyses of Galileo/NIMS spectra have suggested that Europa's endogenous hydrate may be dominated by sulfate salts (e.g. Dalton et al., 2005, 2012; McCord et al., 1998), while more recent studies with higher spectral resolution data sets suggest a chloride dominated composition (Brown et al., 2013; Ligier et al., 2016). Further complicating the picture, the hydrated material of the leading hemisphere chaos is spectroscopically distinct from the hydrated material in the trailing hemisphere chaos, presumably due to the significant exogenous alteration which occurs on the trailing hemisphere (Fischer et al., 2015, 2016; Trumbo et al., 2020). Trumbo et al. (2020) demonstrated that a 360 nm absorption feature and 700 nm slope change strongly correlate to the trailing hemisphere chaos terrains and reflect a combination of endogenous and exogenous processes. They suggest that while relatively unaltered endogenic material may persist in the comparatively sheltered leading hemisphere chaos terrains, it may become progressively more chemically altered towards the trailing hemisphere apex due to radiolytic processing.

A weak absorption feature at 2.07 μm is also present on Europa's trailing hemisphere. It was first noted in the high resolution Keck/OSIRIS observations of Brown et al. (2013), who suggested epsomite ($MgSO_4 \cdot 7\,H_2O$) or magnesium sulfate brine as a plausible spectral match. With no sign of a sulfate absorption on Europa's leading hemisphere, they suggested that magnesium chloride ($MgCl_2$) sourced from Europa's interior may be radiolytically converted into epsomite, a hydrated magnesium sulfate ($MgSO_4$), when in the presence of Iogenic sulfur ions deposited onto the trailing hemisphere. While it is possible that this conceptual model of the alteration of chloride-rich endogenic salts into sulfates via sulfur radiolysis could be consistent with the visible-wavelength data of the trailing hemisphere (Hibbitts et al., 2019; Trumbo et al., 2020), more laboratory data is needed to test this hypothesis. Ligier et al. (2016), on the other hand, used VLT/SINFONI observations to show that the 2.07 μm absorption feature can also be reproduced by certain combinations of

$MgCl_2$ and perchlorate ($Mg(ClO_4)_2$) salts, despite neither one having a distinct absorption on their own. The authors suggested that endogenic magnesium-chloride may be radiolytically converted into magnesium chlorate and perchlorate, rather than sulfate, on Europa's trailing hemisphere.

Both proposed origins for the 2.07 μm absorption feature (magnesium-bearing sulfates versus chlorine salts) share one important characteristic. They require a contribution of endogenic material, presumably tied to the ocean chemistry, which is chemically altered into the species responsible for the absorption by the trailing hemisphere irradiation environment. In both of these scenarios we would expect to find a spatial correlation between the presence and depth of the 2.07 μm feature and the large-scale geologic units or chaos terrains, where we would expect geologic resurfacing to have emplaced endogenic, salty material. The trailing hemisphere chaos terrains are spectroscopically distinct from their leading hemisphere counterparts (Trumbo et al., 2020), presumably due to irradiation induced chemical alteration of this endogenic material. Indeed, the best fit spectral models from Ligier et al. (2016) show an enhancement of $MgCl_2$ in the chaos terrains on both hemispheres and magnesium perchlorate confined mainly to the trailing hemisphere chaos, consistent with the 2.07 μm feature arising from a mixture of endogenic chloride and its irradiation product. However, their models do not map the 2.07 μm absorption feature directly, but rather rely on linear mixture modeling of the largely featureless near infrared continuum, and degeneracies amongst the various salt hydrates make positive identification difficult. A more recent study by King et al. (2022) combined VLT/SPHERE and Galileo/NIMS observations in an attempt to model Europa's surface composition across the near-infrared. Their best fit models include sodium chloride and show distributions for both magnesium sulfate and magnesium bearing chlorine species, which are broadly consistent with both hypotheses. However, they point out that the uncertainties in the model abundances and degenerate fit results for various compositional mixtures mean confident detection of any individual salt species is not feasible with the existing data sets.

Previous observations indicate that irradiated NaCl is likely present and spatially concentrated in the leading hemisphere chaos terrains (Trumbo et al., 2022), and confirmation of endogenic $MgCl_2$ or its radiolytic products could provide crucial information for constraining Europa's ocean and surface chemistry. While atomic sodium and potassium, as well as chlorine ions, likely sputtered from the surface, have been detected in Europa's atmosphere or a nearby pickup cloud (Brown, 2001;

Brown et al., 1996; Volwerk et al., 2001), attempts to measure magnesium in Europa's atmosphere were unsuccessful. Hörst et al. (2013) provide an upper limit on the atmospheric Na/Mg ratio of at least a factor of two less than meteoritic or cosmic abundances, and the presence of magnesium bearing salts on Europa's surface remains unproven. Thus, the detection of $MgCl_2$ along with NaCl on Europa's surface may have important implications for the relative balance of various cation and anion species within Europa's ocean. In the relatively simple freezing models of Johnson et al. (2019), for example, the presence of $MgCl_2$ could suggest a sulfate-poor, sodium, magnesium and chloride rich ocean with a low pH due the presence of magnesium ions.

With two possible origins of Europa's 2.07 μm absorption feature arising from radiolytic processing of endogenic $MgCl_2$ and no clear resolution for the genesis of the feature from spectral modeling, we turn to the spatial distribution of the absorption across Europa's trailing hemisphere in an attempt to gain insight. In this chapter, we use high spatial and moderate spectral resolution archived VLT/SINFONI data to explore the spatial distribution of the 2.07 μm feature and determine whether its presence is associated with the large-scale chaos terrains, which could confirm its suspected relationship to endogenic salts and possibly Europa's ocean chemistry.

2.2 Observations and Data Reduction

We use archived spatially resolved, moderate-resolution, ground-based near-infrared spectra from VLT/SINFONI acquired with adaptive optics during ESO program 088.C-0833(A) at Paranal Observatory and originally published in Ligier et al. (2016). The data were obtained by Ligier et al. (2016) over five nights between October 2011 and January 2012 in the H+K band setting, covering a wavelength range of 1.452 - 2.447 μm at a spectral resolution of ~1 nm ($R \sim \frac{\lambda}{\Delta\lambda} = 1500$). Europa's angular diameter on-sky ranged from 0.897" to 1.083", so to cover the full disk with the 0.8" × 0.8" field of view, integrations were taken in five offset frames and co-added into a single mosaic across the full disk. The on-sky spatial sampling of the SINFONI instrument is 12.5 × 25 mas, resulting in spatial pixels of ~35 × 70 km at the center of Europa's disk. We note that the spatial scale of the SINFONI pixels over-samples the diffraction-limited spatial resolution of the VLT at the wavelengths of interest, which is ~130 km at the center of Europa. More detailed information on these observations can be found in Table 1 in Ligier et al. (2016).

We downloaded the raw data and associated calibration files from the ESO Science Archive Facility and followed a similar reduction routine as Ligier et al. (2016). As a first step in the data reduction process, we used the ESO SINFONI data reduction pipeline v3.3.3 with EsoRex (Modigliani et al., 2007). The pipeline identified bad, non-linear and hot pixels, performed standard dark and flat lamp corrections, corrected for optical distortions in the image slicer slitlets, determined a calibrated wavelength solution, and computed the 2D to 3D mapping to create a 3D data cube with two spatial dimensions and one spectral dimension for each observation. We interrupted the pipeline before the five offset frames were combined into a single mosaic to remove correlated regions of bad-pixel patches, which were not identified by the pipeline, and which were also noted by Ligier et al. (2016). We identified these bad pixel regions using the spectral angle mapping criterion (SAM) (Kruse et al., 1993), which describes the degree of similarity between two spectra. We masked out pixels with a SAM angle that differed by more than ∼10% from the median SAM angle between all individual spectra and the combined median in a 10×10 pixel bounding box centered on the bad pixel. These bad pixel regions, which makeup ∼7% of the total detector pixels, were excluded from the final co-added data cube created after running the remainder of the ESO pipeline. While Ligier et al. (2016) do not indicate what method they used to identify these remaining bad pixel patches, we find that our identified bad pixel patches closely match the pixels which appear to be masked in Figure 3 of Ligier et al. (2016).

Next, we used the standard star observations of the solar-type star HD18681, which were taken immediately before or after the Europa observations on each night, to correct for the instrument response, remove telluric absorption features, and derive a relative reflectance calibration. Due to the range of air masses over which the five Europa cubes and the calibration star were observed each night, an on-sky angular separation between Europa and HD18681 of ∼17°, and possibly changing atmospheric conditions, we found a simple division by the telluric standard was not sufficient. The quality of the telluric correction is particularly important for our analysis of the 2.07 μm absorption, which is just beyond telluric CO_2 and O_2 absorptions between 2.0 and 2.05 μm. We therefore followed a similar telluric correction procedure as described in Brown et al. (2013) and continuum divided the observed telluric spectrum by a best-fit polynomial to construct an atmospheric transmission spectrum. We then empirically determined an exponential scaling factor which adjusts the depths of the telluric absorptions in the transmission spectrum to most closely match the telluric signature in each of the Europa observations,

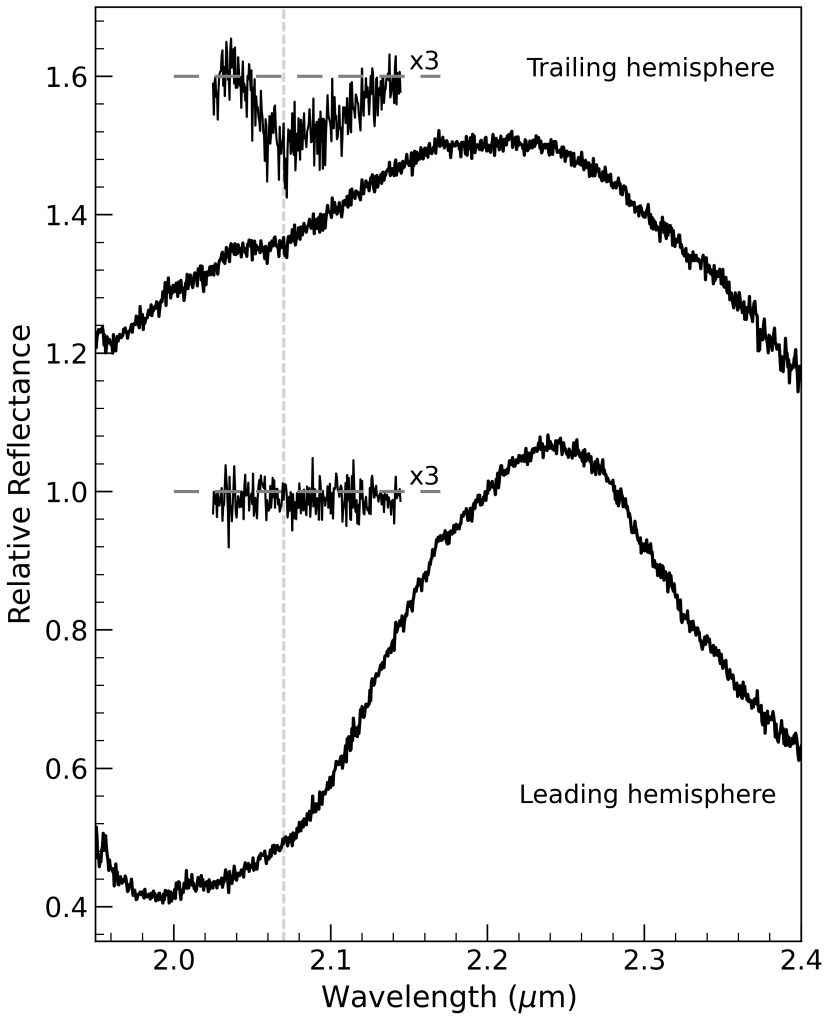

Figure 2.1: Example VLT/SINFONI spectra of Europa's leading and trailing hemispheres showing the 2.07 μm absorption feature, which is only present on Europa's more heavily irradiated trailing hemisphere. The data are normalized to 1.0 at 2.2 μm and the trailing hemisphere spectrum is offset by +0.5 for clarity. The vertical dotted line marks the location of the 2.07 μm band center and the continuum-removed absorption (multiplied by a factor of 3) is included above each spectrum.

paying particular attention to the quality of the telluric removal of the CO_2 and O_2 features between 2.0 and 2.05 μm. Each observation consists of hundreds of spectra, which allowed us to determine the optimal scaling factor to very high precision. The original stellar continuum fit was multiplied by this best-fit atmospheric transmission spectrum to create a new standard star spectrum with an appropriately scaled telluric signature, which was then divided from the Europa observations. As described in Ligier et al. (2016), we used a Lambertian surface to calculate the geometrically corrected reflectance spectrum of each pixel and corrected for

small offsets in the relative reflectance of overlapping regions on Europa's surface obtained during different nights by scaling the band-integrated flux of each observation cube so that the integrated reflectance matched in these overlapping regions. The final data product is a series of data cubes, one for each hemispherical view on Europa (centered at 30°W, 55°W, 130°W, 225°W, and 315°W) with the corresponding relative reflectance spectrum for each pixel[1]. A characteristic leading and trailing hemisphere spectrum, at (90°W, 0°N) and (270°W, 0°N) respectively, are shown in Figure 2.1, with the 2.07 μm absorption feature present only in the trailing hemisphere spectrum.

2.3 Spatial Distribution

With no clear resolution of the source of the 2.07 μm feature from previous studies (Brown et al., 2013; Ligier et al., 2016), we turn to its spatial distribution in order to determine whether its presence is associated with the large-scale chaos terrains, which could confirm its suspected relationship to endogenic salts and possibly Europa's ocean chemistry. We note that endogenic salts are expected within Europa's bands and ridges as well as within the chaos terrains (e.g. Dalton et al., 2012). Indeed, while the exact formation mechanism of these bands and ridges is not known, many proposed mechanisms require a direct link between the ice shell and ocean (e.g. Fagents et al., 2000; Head et al., 1999; Howell et al., 2018; Johnson et al., 2017; Prockter et al., 2009). However, ridges on Europa are typically a few hundred meters to a few kilometers wide (Collins et al., 2009) and bands are no wider than 30 km (Prockter et al., 2002). At the spatial resolution of the VLT (~130 km) the fractional coverage of a band or ridge feature within a single pixel is small. If irradiation of endogenic salts were responsible for the 2.07 μm feature, we would therefore expect to measure a difference in the band strength between the large-scale chaos terrains which fully cover a single VLT spatial resolving element, and the background plains, which are overlaid by bands and ridges that only cover a small fraction of the spatial resolving element and are therefore unresolved. Indeed, the spectral signature of irradiated endogenic material correlated with the trailing hemisphere chaos terrains is seen in the maps of Trumbo et al. (2020) which have a comparable spatial resolution of ~150 km. The 360 nm absorption feature attributed to radiolytically processed endogenic material, for example, is strongest within the large scale chaos terrains and is significantly weaker or absent from the non-chaos pixels on the trailing hemisphere. If confirmed, a similar association of the 2.07 μm

[1]The full, reduced dataset is permanently archived at https://doi.org/10.22002/agga7-v3393

absorption band with Europa's large-scale chaos terrains would therefore support the hypotheses of Brown et al. (2013) and Ligier et al. (2016), which suggest the absorption arises from some radiolytic product of endogenic material.

One common way to examine the spatial distribution of an absorption feature is to map its depth or area. However, the continuum shape between 2.0 and 2.2 μm changes significantly across Europa's surface, largely due to variation in the strength of the 2.0 μm water absorption band. As can be seen in Figure 2.1, the change in the slope, concavity, and overall spectral shape between the leading and trailing hemispheres is larger than the depth of the 2.07 μm feature. The shape of the spectrum in this region varies gradually across Europa's surface, and we find that challenges in precisely defining this changing continuum, combined with significant pixel-to-pixel noise inherent in the IFU data, lead to large uncertainties in the measured band strength. Another option is to compare the depth of the 2.07 μm feature between the chaos and non-chaos terrains integrated over the entire trailing hemisphere. However, the irradiation bullseye is symmetric about the trailing apex while the distribution of the chaos terrains on Europa's trailing hemisphere is not. As a result, the integrated chaos terrain spectrum samples areas on Europa with a sufficiently different continuum spectrum than is sampled by the integrated non-chaos pixels, such that it is difficult to determine whether these continuum differences wash out the signal of a geologic association or if the feature simply does not correlate with Europa's geology. We therefore construct a new technique wherein we consider rings of approximately constant radiolysis, where the overall continuum between ~2 to 2.2 μm is much more constant, and compare the strength of the 2.07 μm feature for integrated spatial pixels that are within different large-scale geologic units and receive a similar irradiation dose.

To perform this spatial analysis, we first define the large-scale geologic units using the new United States Geologic Survey (USGS) global geologic map of Europa, which maps geologic units including craters, chaos terrains, bands, and regional plains at a scale of 1:15M (Leonard et al., 2023). Because the width of the bands and ridges are much smaller than our ~130 km spatial resolution, we exclude these from our large-scale geologic units. We also exclude ten small craters with diameters less than ~100 km and several small patches of discontinuous crater ejecta which are unresolved at the spatial resolution of the VLT. This leaves us with three distinct large-scale geologic units on Europa's trailing hemisphere - chaos terrains, ridged plains, and Pwyll crater including its large ejecta blanket. The chaos terrains can

be further broken down into three sub-types - low albedo chaos, mottled chaos, and knobby chaos as defined in Leonard et al. (2023).

We then define a set of “constant radiolysis rings" which cover the trailing hemisphere, where each ring contains pixels that are expected to receive a similar irradiation dose. While the idea is simple, the exact irradiation geometry on Europa is complex and remains an active area of research (Bagenal et al., 2020; Cassidy et al., 2013; Paranicas et al., 2009). The location dependent irradiation dose depends on a number of factors, including the type of particle, its energy, and the complex interaction between Jupiter’s magnetosphere, the plasma torus, and Europa’s ionosphere and a variety of irradiation patterns is possible (Bagenal et al., 2020). However, sulfuric acid production via the sulfur radiolytic cycle relies on the presence of sulfur ions from the plasma torus as well as radiolytic processing from energetic electrons and light ions, which are important sources of ionization energy that drive surface chemistry changes on Europa (Cassidy et al., 2013; Paranicas et al., 2001, 2009, 2002). The shape of the sulfuric acid bullseye is therefore a simple proxy for the total radiolytic processing from the combined effects of the plasma torus and magnetospheric particle bombardment occurring at a given location on Europa’s trailing hemisphere. To match the shape of the sulfuric acid bullseye, we start with a series of overlapping rings centered on the trailing hemisphere apex and defined by $\cos(\theta)$, where θ is the angular distance from the trailing hemisphere apex. We then empirically determine a latitudinal flattening coefficient of 0.6 so that the shape of the rings matches the sulfuric acid bullseye from Figure 10 in Ligier et al. (2016) and set the width of the rings to match the diffraction-limited spatial resolution of the VLT. Figure 2.2 shows a selection of four example rings distributed across the trailing hemisphere.

Once we have defined our constant radiolysis rings and large-scale geologic units, we assign each data pixel to its respective ring and geologic unit. Data pixels which overlap, typically because they were observed on two separate nights, are separated into multiple polygons and intersecting regions are averaged. In this way, we preserve the maximum possible spatial information from the dataset. In order to account for the wings of the point spread function (PSF), we exclude any spatial pixels whose central coordinates are within one spatial resolving element of a boundary between geologic units. Spatial pixels which cross the boundary of a ring are assigned to whichever ring intersects the largest fraction of the pixel. Pixels with more than 40% of their area in two separate rings are duplicated and assigned

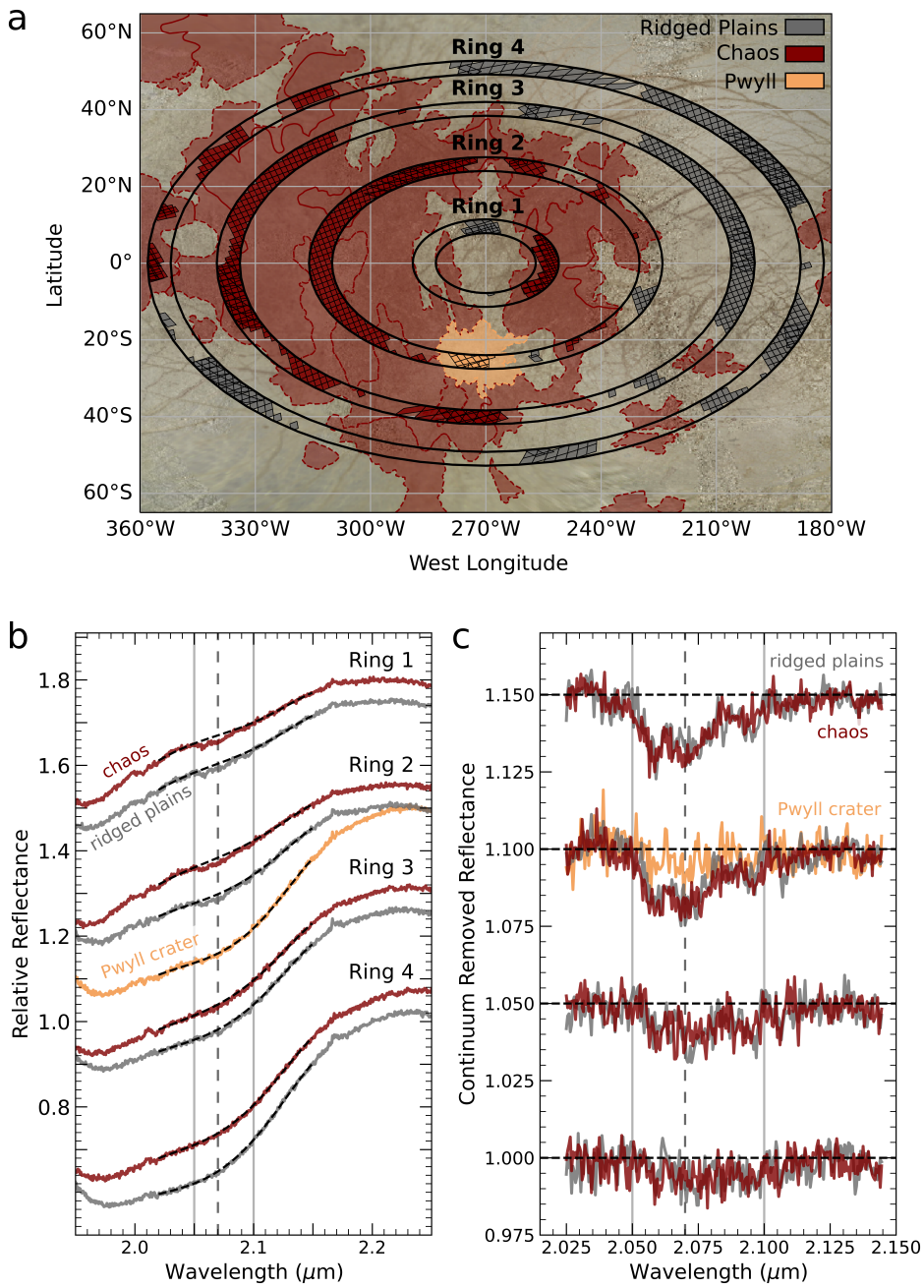

Figure 2.2: (a) A map of Europa's trailing hemisphere, showing a selection of four of the 29 considered "rings of constant radiolysis" outlined in black, which are used to determine whether the weak 2.07 μm absorption feature is associated with Europa's large-scale geologic units. The chaos terrains are shown in red and Pwyll crater and its ejecta are orange. For each ring, projected detector pixels are shown and their assigned geologic unit indicated by color, where chaos terrains are dark red, Pwyll crater and its ejecta are orange, and the ridged plains are gray. (Europa map image credit: NASA/JPL/ Björn Jónsson). (b) Summed spectra, by geologic unit, for all of the pixels within each example ring. Spectra are normalized to 1.0 at 2.12 μm and

Figure 2.2 (cont): offset for clarity. The best-fit polynomial continuum is indicated by a black dashed line. (c) Continuum removed absorption feature, by geologic unit, for the four selected example constant radiolysis rings. The depth of the feature decreases noticeably as we move from Ring 1 outwards, however there is no apparent difference in the depth of the 2.07 μm feature between the chaos terrains (red) and ridged plains (gray) for a given ring. This suggests that the absorption feature is unaffected by the compositional difference between the chaos terrains and ridged plains, and it is therefore unlikely to be related to any of the proposed irradiation products of endogenic material. Instead, the 2.07 μm feature appears to arise from the radiolytic processing of water ice with exogenic material, possibly related to the sulfur radiolytic cycle. One notable exception is that the 2.07 μm absorption feature is entirely absent from Pwyll crater and its ejecta blanket.

to both. Once all of the pixels have been categorized, we sum the spectra from all of the pixels assigned to a given geologic unit and constant radiolysis ring. We then normalize these integrated spectra at 2.12 μm, just past the absorption feature of interest, and plot the spectra for each geologic unit in order to compare the depth of the 2.07 μm feature. Most of the rings only have integrated spectra for the chaos terrains and ridged plains, however a few rings also contain pixels from Pwyll crater and its ejecta blanket. The irradiation pattern is expected to be symmetric about the trailing hemisphere apex (Cassidy et al., 2013; Hendrix et al., 2011; Paranicas et al., 2009), so we do not expect the east-west dichotomy in the terrain types, with significantly more chaos towards the sub-Jovian hemisphere and more plains towards the anti-Jovian hemisphere, to affect the results of our analysis. We also fit a fifth order polynomial continuum to each of the integrated spectra between 1.98 and 2.16 μm, excluding the region between 2.04 and 2.1 μm which contains the absorption feature and compare the continuum removed absorptions for the different geologic units. We choose a fifth order polynomial because it is able to provide a fair visual match to the continuum near the center of the trailing hemisphere as well as in the more icy regions where a third order polynomial produces an artificially deep absorption feature because the polynomial is not able to account for the concavity of the continuum shape, which is strongly influenced by the 2.0 μm water ice absorption feature. We then continuum divide each spectrum and integrate the residual absorption between 2.05 and 2.1 μm to compute an integrated band area.

As can be seen for a selection of four constant radiolysis rings in Figure 2.2, visual inspection of the integrated and continuum removed spectra (panels (b) and (c))

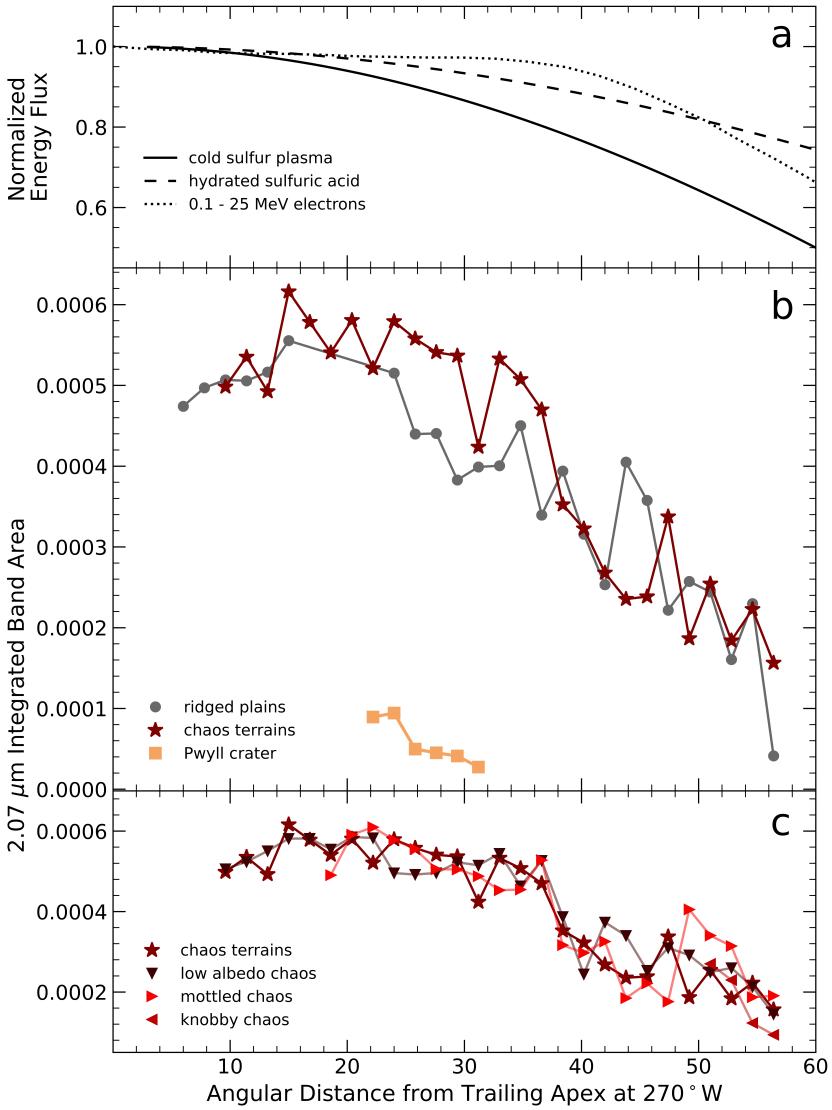

Figure 2.3: (a) Expected trailing hemisphere irradiation patterns as a function of the angular distance from the trailing hemisphere apex for cold sulfur ions (solid) (Cassidy et al., 2013), radiolytically produced hydrated sulfuric acid (dashed) (e.g. Carlson et al., 2002; Ligier et al., 2016), and 0.1 - 25 MeV electrons (dotted) (Paranicas et al., 2009). The estimated energy fluxes are normalized to 1.0 at the trailing hemisphere apex. (b) Calculated band area of the 2.07 μm absorption feature for each of the 29 “rings of constant radiolysis" considered. We find no measurable difference in the absorption depth between the chaos terrains and ridged plains. However, the absorption feature is essentially absent from Pwyll crater and its ejecta blanket. (c) Calculated 2.07 μm band area of the chaos terrains from panel b, with the chaos terrains further subdivided by type as described in Leonard et al. (2023). There is no measurable difference in the 2.07 μm band area between the different types of chaos terrain.

reveals that there is no discernible difference in the depth of the 2.07 μm feature between the chaos terrains (red) and surrounding ridged plains (gray). Indeed, we find no discernible difference in the absorption band between the chaos and ridged plains in any of the 29 rings of constant radiolysis, which completely cover the trailing hemisphere. Likewise, we do not find a measurable difference in the integrated band areas between the chaos and ridged plains units for each ring, as seen in Figure 2.3. We do not include error bars on the measured band areas in Figure 2.3 because we are unable to accurately calculate these uncertainties with the unknown effects of the changing continuum. However, we estimate a rough error of $\sim 10^{-4}$ on the integrated band area based on the scatter in the measured band areas of adjacent, overlapping rings. Figure 2.3 (c) shows the measured band areas for each chaos sub-type, when present in each of the 29 constant radiolysis rings. Separately considering each chaos sub-type (low albedo chaos, mottled chaos, and knobby chaos) identified by Leonard et al. (2023) also reveals no discernible difference in the depth of the 2.07 μm feature between the chaos terrain sub-types. Most of the trailing hemisphere chaos terrains are comprised of low albedo chaos (~64% fractional coverage) and mottled chaos (~32%), with only ~4% of the chaos at larger angular distances from trailing center classified as knobby chaos.

It is interesting to note that the 2.07 μm absorption feature is clearly absent from Pwyll crater and its ejecta blanket, even though Pwyll is located in a region with relatively high amounts of radiolysis. Ring 2 in Figure 2.2 highlights the absence of this feature at Pwyll, and also illustrates that significant differences in the depth of the 2.07 μm feature between different large-scale geologic units are identifiable with our spatial analysis technique. The absence of a 2.07 μm absorption feature within the Pwyll crater ejecta blanket is also clearly seen in Figure 2.3 (b), where the measured band areas for Pwyll are very small compared to the band areas of the chaos terrains and ridged plains within the same constant radiolysis rings.

While the strength of the 2.07 μm absorption feature appears to be constant between the chaos terrains and ridged plains for each constant radiolysis ring, a clear decrease in the strength of the feature is seen as we move from the innermost rings with the highest expected radiolysis rates to the outermost rings where the 2.07 μm feature is no longer seen. This decrease in band area is consistent with radiolytic production of the species responsible for the absorption feature. As a third and final check, we examined the division of the integrated ridged plains by the chaos terrain spectra and found that for some of the rings there was a broad dip in the ratioed spectrum

between ~ 2 to 2.2 μm, which is a clear spectral match to water ice. This subtle difference in the continuum shape seen between the chaos terrains and ridged plains is consistent with a slight excess of water ice and therefore a deeper 2.0 μm water ice absorption band in the ridged plains relative to the chaos terrains. We find no sign of any additional structure in the ratioed spectra between 2.05 and 2.1 μm, further confirming that the 2.07 μm absorption feature is unaffected by the compositional differences between the large-scale chaos terrains and ridged plains on Europa's trailing hemisphere.

2.4 Discussion

Chaos Terrains and Ridged Plains

As evidenced by its absence on Europa's leading, less-irradiated hemisphere, the species responsible for the 2.07 μm feature is most likely a radiolytic product formed via sulfur radiolysis or processing via magnetospheric particle bombardment. Our spatial distribution analysis reveals that the depth of Europa's 2.07 μm feature is spatially associated with the sulfuric acid bullseye on the trailing hemisphere, which we use as a proxy for the amount of radiolytic processing due to the combined effects of the plasma torus and magnetospheric particle bombardment. This distribution is consistent with a radiolytic origin for the absorption feature. However, we find no evidence of any spatial association with the large-scale chaos terrains which would be expected if the formation pathway required radiolytic processing of endogenic salty material. For any given ring of constant radiolysis, we find no measurable difference in the band area of the 2.07 μm absorption feature between the large-scale chaos terrains and the icier ridged plains suggesting that the irradiation process which creates the 2.07 μm absorption is independent of any endogenic material within Europa's recent geology. With both the epsomite hypothesis of Brown et al. (2013) and the magnesium chlorates hypothesis of Ligier et al. (2016) relying on the presence of irradiated endogenic magnesium chloride ($MgCl_2$), and no known exogenic source of magnesium ions to Europa (Bagenal et al., 2020), we find that the spatial distribution of the 2.07 μm absorption band is inconsistent with both of these proposed origins for the absorption feature. Instead, our results suggest that the species responsible for Europa's 2.07 μm absorption feature is a radiolytic product of water ice and exogenically sourced material and is not affected by the presence of whatever endogenic salt component exists within the chaos terrains.

Pwyll Crater

Pwyll crater has an ~26 km diameter with a bright ray ejecta blanket that extends

over 1000 km (Greeley et al., 1998). Pwyll is thought to be young, with estimates for its age ranging from ~3–18 Myr (Bierhaus et al., 2001). The dark, red crater itself has apparently excavated endogenic material from a depth of ~1 km (Garozzo et al., 2010) and high spatial resolution Galileo/NIMS observations show evidence of asymmetric bands interpreted as salt-rich material at very high concentrations (Fanale et al., 2000). However, the composition sharply transitions to be very ice-rich at the crater edge and throughout the ejecta blanket (Fanale et al., 2000). At the spatial resolution of the VLT, we do not resolve the dark salty crater itself, and are dominated by the spectral signature of the bright ice-rich ejecta blanket. The distinct lack of a 2.07 μm absorption feature within the Pwyll crater ejecta blanket, despite its presence in both the chaos terrains and ridged plains, implies that radiolytic processing has not yet had enough time to form the species responsible. The lack of a 2.07 μm absorption within Pwyll may simply mean that the irradiation timescale for the process which produces the absorption feature is longer than the age of Pwyll crater. Or alternatively, there may not have been time for enough exogenic material from the plasma torus or magnetosphere to build up at Pwyll, thus limiting the production of the species responsible for the absorption. In either case, the absence of the absorption within the Pwyll crater ejecta blanket places a strong lower limit of the age of Pwyll on the timescale over which the species responsible for the 2.07 μm absorption forms on Europa.

Comparison with Irradiation Patterns

Figure 2.3 (b) shows the measured band area for each ring of constant radiolysis as a function of the angular distance due north from the trailing hemisphere apex. Panel (a) shows the expected shape of several distinct irradiation patterns on Europa's trailing hemisphere for comparison with the measured band areas. As previously noted, the absorption feature is absent from the Pwyll crater ejecta blanket, but both the chaos terrains and background ridged plains show a clear decrease in the band area with increasing angular distance. The measured fall-off in band area for the 2.07 μm absorption feature with increasing distance from the trailing hemisphere apex is broadly consistent with a formation pathway driven by the irradiation pattern of the sulfur plasma, energetic ions and electrons, or the measured sulfuric acid bullseye. Cold sulfur plasma bombards the trailing hemisphere with a fall-off described by the cosine of the angle from trailing center (Cassidy et al., 2013; Hendrix et al., 2011), which we would expect to see reflected in the measured 2.07 μm band depths if cold sulfur plasma controlled the formation of the absorption. If the formation pathway is instead driven by energetic electrons, we would expect

a fall-off consistent with the shape of the power per unit area contours for 10 keV–25 MeV electrons from Figure 8 in Paranicas et al. (2009). Or, if the formation pathway is driven by a combination of these irradiation patterns as expected for the sulfur radiolytic cycle, we might expect to find a fall-off consistent with the flattened cosine of the sulfuric acid bullseye.

As can be seen in Figure 2.3 (a), the differences in the shapes of these distributions are small near the center of the trailing hemisphere, where the 2.07 μm absorption feature is strongest, and become more pronounced farther out where the feature has all but disappeared. Uncertainties in measuring the band depths for the various rings and a significant change in the continuum shape moving outwards from trailing center are sufficiently large so as to obscure the subtle differences which could differentiate between these irradiation signatures. The measured band areas for the chaos terrains and ridged plains in Figures 2.3 (b) and (c) show a plausible match to all three irradiation patterns shown in panel (a). Our results remain consistent with a variety of radiolytic production pathways and we are unable to determine whether the overall irradiation flux or the presence of any specific exogenic material is the limiting factor in the formation of the 2.07 μm absorption.

Potential Origins for the 2.07 μm Absorption

If the 2.07 μm absorption feature does indeed arise from the radiolytic processing of water ice and exogenically sourced material on Europa's trailing hemisphere, the products of the known sulfur cycle offer an obvious first place to search for a plausible spectral match. Laboratory experiments have shown that various irradiation products can be created in electron or ion irradiated water ice bearing sulfur ions, or via sulfur ion bombardment of pure water ice. However, the specific products produced depend strongly on the temperatures, energies, and projectiles involved (Loeffler et al., 2011; Moore et al., 2007; Strazzulla et al., 2007). While hydrated sulfuric acid (H_2SO_4) is expected to be the dominant irradiation product on Europa, some of the possible intermediate products include sulfur dioxide (SO_2), hydrogen sulfide (H_2S), and various sulfate anions (SO_4^{2-}, SO_3^{2-}, HSO_4^-) which can combine to form species such as sulfonic acid (SO_2H_2) or hydrogen disulfide (H_2S_2). Tribbett et al. (2022) demonstrated that H_2O + H_2S + O_3 ice mixtures at Europa temperatures can undergo thermal oxidation reactions on laboratory timescales, which may affect the steady state composition and intermediary products of the radiolytic sulfur cycle.

Calculations based on laboratory experiments of sulfur ion implantation in water ice have shown that radiolysis can produce the expected concentration of sulfuric acid

hydrate on Europa during $\sim 10^4$ years (Strazzulla, 2011). Therefore, if the feature arises from an intermediary of the sulfur cycle or a parallel irradiation process, it is somewhat surprising that we do not see any evidence for the 2.07 μm absorption feature in Pwyll crater. However, Europa's UV to visible albedo ratio, which is anti-correlated with irradiation induced discoloration on the trailing hemisphere, also shows an enhancement at Pwyll suggesting that the discoloration timescale is longer than the age of Pwyll crater (Burnett et al., 2021) and consistent with the observed absence of the 2.07 μm absorption feature. If the 2.07 μm feature does arise from an intermediary of the radiolytic sulfur cycle, the lack of a feature at Pwyll could suggest that Pwyll crater is much younger than expected, that it has not yet had enough time to build up a sufficient amount of sulfur for sulfur radiolysis to occur, or alternatively that the calculations of Strazzulla (2011) significantly underestimate the timescale over which the sulfur cycle should reach an equilibrium state. Future laboratory work may be crucial for understanding this discrepancy.

Additionally, the 2.07 μm absorption feature may also be explained by a parallel radiolytic cycle or some other unknown irradiation product. For example, the addition of CO_2 ice into various sulfur radiolysis studies produced additional products such as carbonyl sulfide (OCS), carbon disulfide (CS_2), carbonic acid (H_2CO_3), and other carbon and sulfur bearing species (Garozzo et al., 2010; Mahjoub et al., 2017). While CO_2 has been detected on Europa (Carlson et al., 2009; Hansen et al., 2008; McCord et al., 1998), its spatial distribution across the trailing hemisphere is largely unconstrained. It is therefore uncertain whether an irradiation product of a combined carbon-sulfur radiolytic cycle is consistent with our observed spatial distribution, but nevertheless worth investigating.

We completed an extensive literature search of these potential sulfur- and carbon-bearing intermediary species and other possible irradiation products but were unable to find a plausible spectral match for the 2.07 μm absorption amongst existing data sets. We are therefore unable to identify the source of the 2.07 μm absorption feature, highlighting the need for additional irradiation experiments at Europa-like temperatures, particularly those including spectra across the full near-infrared wavelength range, in order to better understand the sulfur radiolytic cycle and determine whether any generated products can explain the 2.07 μm absorption feature.

2.5 Conclusions

Using archived VLT/SINFONI H+K band spectra, we have shown that the presence and band area of the 2.07 μm absorption feature on Europa's trailing hemisphere is not spatially associated with the large-scale geology, except for Pwyll crater and its ejecta blanket which lacks the absorption feature. There is, however, a spatial association between the 2.07 μm absorption band and the trailing hemisphere sulfuric acid bullseye suggesting that the formation of the 2.07 μm feature on Europa is independent of the endogenous salts thought to be present within the chaos terrains and is most likely an irradiation product of water ice and exogenic material. Thus, we find that neither epsomite nor a combination of magnesium chloride and magnesium perchlorate, as proposed by Brown et al. (2013) and Ligier et al. (2016), respectively, are likely to explain the spatial distribution of the 2.07 μm absorption feature and we consider an alternative hypothesis. We propose that the source of this feature may be an intermediary product of the radiolytic sulfur cycle, or something formed during the bombardment of water ice by electrons or the remaining (non-sulfur) ion species. Current laboratory data of relevant radiolytic species is fairly sparse in the 2.0–2.2 μm range and we are unable to identify any plausible spectral matches. This highlights the need for more laboratory data at these wavelengths and at Europa-like conditions in order to identify radiolytic product(s) which may be responsible for the 2.07 μm absorption feature and provide insights into the nature of the sulfur- and possibly carbon-radiolysis occurring on Europa.

Acknowledgments

This research has made use of the services of the ESO Science Archive Facility and is based on observations collected at the European Southern Observatory under ESO program 088.C-0833(A). M.R.D. would like to thank Dr. Erin Leonard for providing up-to-date shape files from the new United States Geologic Survey (USGS) global geologic map of Europa, which we used to define the various geologic units discussed in the text. S.K.T. is supported by the Heising-Simons Foundation through a 51 Pegasi b postdoctoral fellowship.

Facilities: VLT:Yepun (SINFONI)

Software: Astropy (Astropy Collaboration et al., 2018, 2022, 2013), Cartopy (Met Office, 2022), GeoPandas (Jordahl et al., 2022), SciPy (Virtanen et al., 2020), Shapely (Gillies et al., 2023), SpecUtils (Earl et al., 2022)

BIBLIOGRAPHY

Anderson, J. D. et al. (1998). "Europa's Differentiated Internal Structure: Inferences from Four Galileo Encounters". *Science* 281.5385, pp. 2019–2022.

Astropy Collaboration, A. M. Price-Whelan, et al. (2018). "The Astropy Project: Building an Open-Science Project and Status of the v2.0 Core Package". *The Astronomical Journal* 156.3, p. 123.

Astropy Collaboration, A. M. Price-Whelan, et al. (2022). "The Astropy Project: Sustaining and Growing a Community-Oriented Open-Source Project and the Latest Major Release (v5.0) of the Core Package". *The Astrophysical Journal* 935.2, p. 167.

Astropy Collaboration, T. P. Robitaille, E. J. Tollerud, et al. (2013). "Astropy: A Community Python Package for Astronomy". *Astronomy & Astrophysics* 558, A33.

Bagenal, F. and V. Dols (2020). "The Space Environment of Io and Europa". *Journal of Geophysical Research: Space Physics* 125.5.

Bierhaus, E. B. et al. (2001). "Pwyll Secondaries and Other Small Craters on Europa". *Icarus* 153.2, pp. 264–276.

Brown, M. E. and K. P. Hand (2013). "Salts and Radiation Products on the Surface of Europa". *The Astronomical Journal* 145.4, p. 110.

Brown, M. E. (2001). "Potassium in Europa's Atmosphere". *Icarus* 151.2, pp. 190–195.

Brown, M. E., W. T. P. Denman, and S. K. Trumbo (2022). "The Mid-UV Spectrum of Irradiated NaCl at Europa-Like Conditions". *The Planetary Science Journal* 3.2, p. 28.

Brown, M. E. and R. E. Hill (1996). "Discovery of an Extended Sodium Atmosphere around Europa". *Nature* 380.6571, pp. 229–231.

Burnett, E. R. and P. O. Hayne (2021). "Europa's Hemispheric Color Dichotomy as a Constraint on Non-Synchronous Rotation". *Icarus* 364, p. 114438.

Carlson, R. W. et al. (2002). "Sulfuric Acid Production on Europa: The Radiolysis of Sulfur in Water Ice". *Icarus* 157.2, pp. 456–463.

Carlson, R. W. et al. (2005). "Distribution of Hydrate on Europa: Further Evidence for Sulfuric Acid Hydrate". *Icarus* 177.2, pp. 461–471.

Carlson, R. W. et al. (2009). "Europa's Surface Composition". *Europa*. Ed. by R. T. Pappalardo, W. B. McKinnon, and K. Khurana. University of Arizona Press, Tucson AZ, p. 283.

Carlson, R. W., R. E. Johnson, and M. S. Anderson (1999). "Sulfuric Acid on Europa and the Radiolytic Sulfur Cycle". *Science* 286.5437, pp. 97–99.

Carr, M. H. et al. (1998). "Evidence for a Subsurface Ocean on Europa". *Nature* 391.6665, pp. 363–365.

Cassidy, T. A. et al. (2013). "Magnetospheric Ion Sputtering and Water Ice Grain Size at Europa". *Planetary and Space Science* 77, pp. 64–73.

Chyba, C. F. (2000). "Energy for Microbial Life on Europa". *Nature* 403.6768, pp. 381–382.

Collins, G. and F. Nimmo (2009). "Chaotic Terrain on Europa". *Europa*. Ed. by R. T. Pappalardo, W. B. McKinnon, and K. Khurana. University of Arizona Press, Tucson AZ, pp. 259–281.

Cooper, J. F. et al. (2001). "Energetic Ion and Electron Irradiation of the Icy Galilean Satellites". *Icarus* 149.1, pp. 133–159.

Dalton, J. B. et al. (2005). "Spectral Comparison of Heavily Hydrated Salts with Disrupted Terrains on Europa". *Icarus* 177.2, pp. 472–490.

Dalton, J. B., J. H. Shirley, and L. W. Kamp (2012). "Europa's Icy Bright Plains and Dark Linea: Exogenic and Endogenic Contributions to Composition and Surface Properties". *Journal of Geophysical Research: Planets* 117.E3.

Denman, W. T. P., S. K. Trumbo, and M. E. Brown (2022). "The Influence of Temperature and Photobleaching on Irradiated Sodium Chloride at Europa-Like Conditions". *The Planetary Science Journal* 3.2, p. 26.

Earl, N., E. Tollerud, C. Jones, et al. (2022). *astropy/specutils: V1.9.1*. Version v1.9.1.

Fagents, S. A. et al. (2000). "Cryomagmatic Mechanisms for the Formation of Rhadamanthys Linea, Triple Band Margins, and Other Low-Albedo Features on Europa". *Icarus* 144.1, pp. 54–88.

Fanale, F. P. et al. (2000). "Tyre and Pwyll: Galileo Orbital Remote Sensing of Mineralogy versus Morphology at Two Selected Sites on Europa". *Journal of Geophysical Research: Planets* 105.E9, pp. 22647–22655.

Fischer, P. D., M. E. Brown, and K. P. Hand (2015). "Spatially Resolved Spectroscopy of Europa: The Distinct Spectrum of Large-Scale Chaos". *The Astronomical Journal* 150.5, p. 164.

Fischer, P. D. et al. (2016). "Spatially Resolved Spectroscopy of Europa's Large-Scale Compositional Units at 3–4 μm with Keck NIRSPEC". *The Astronomical Journal* 153.1, p. 13.

Garozzo, M. et al. (2010). "The Fate of S-bearing Species after Ion Irradiation of Interstellar Icy Grain Mantles". *Astronomy and Astrophysics* 509, A67.

Gillies, S. et al. (2023). *Shapely: Manipulation and Analysis of Geometric Objects*. Version v2.0.1. toblerity.org.

Greeley, R. et al. (1998). “Europa: Initial Galileo Geological Observations”. *Icarus* 135.1, pp. 4–24.

Greenberg, R. et al. (1999). “Chaos on Europa”. *Icarus* 141.2, pp. 263–286.

Hand, K. P. and R. W. Carlson (2015). “Europa’s Surface Color Suggests an Ocean Rich with Sodium Chloride”. *Geophysical Research Letters* 42.9, pp. 3174–3178.

Hand, K. P. et al. (2009). “Astrobiology and the Potential for Life on Europa”. *Europa*. Ed. by R. T. Pappalardo, W. B. McKinnon, and K. Khurana. University of Arizona Press, Tucson AZ, pp. 589–629.

Hansen, G. B. and T. B. McCord (2004). “Amorphous and Crystalline Ice on the Galilean Satellites: A Balance between Thermal and Radiolytic Processes”. *Journal of Geophysical Research: Planets* 109.E1.

– (2008). “Widespread CO2 and Other Non-Ice Compounds on the Anti-Jovian and Trailing Sides of Europa from Galileo/NIMS Observations”. *Geophysical Research Letters* 35.1.

Head, J. W., R. T. Pappalardo, and R. Sullivan (1999). “Europa: Morphological Characteristics of Ridges and Triple Bands from Galileo Data (E4 and E6) and Assessment of a Linear Diapirism Model”. *Journal of Geophysical Research: Planets* 104.E10, pp. 24223–24236.

Hendrix, A. R. et al. (2011). “Europa’s Disk-Resolved Ultraviolet Spectra: Relationships with Plasma Flux and Surface Terrains”. *Icarus* 212.2, pp. 736–743.

Hibbitts, C. A. et al. (2019). “Color Centers in Salts—Evidence for the Presence of Sulfates on Europa”. *Icarus* 326, pp. 37–47.

Hörst, S. M. and M. E. Brown (2013). “A Search for Magnesium in Europa’s Atmosphere”. *The Astrophysical Journal Letters* 764.2, p. L28.

Howell, S. M. and R. T. Pappalardo (2018). “Band Formation and Ocean-Surface Interaction on Europa and Ganymede”. *Geophysical Research Letters* 45.10, pp. 4701–4709.

Johnson, B. C. et al. (2017). “Porosity and Salt Content Determine If Subduction Can Occur in Europa’s Ice Shell”. *Journal of Geophysical Research: Planets* 122.12, pp. 2765–2778.

Johnson, P. V. et al. (2019). “Insights into Europa’s Ocean Composition Derived from Its Surface Expression”. *Icarus* 321, pp. 857–865.

Johnson, R. E. et al. (2002). “Energy Distributions for Desorption of Sodium and Potassium from Ice: The Na/K Ratio at Europa”. *Icarus* 156.1, pp. 136–142.

Johnson, R. E. et al. (2003). “The Production of Oxidants in Europa’s Surface”. *Astrobiology* 3.4, pp. 823–850.

Jordahl, K., J. Van den Bossche, M. Fleischmann, et al. (2022). *geopandas*. Version v0.12.2.

King, O., L. N. Fletcher, and N. Ligier (2022). "Compositional Mapping of Europa Using MCMC Modeling of Near-IR VLT/SPHERE and Galileo/NIMS Observations". *The Planetary Science Journal* 3.3, p. 72.

Kivelson, M. G. et al. (2000). "Galileo Magnetometer Measurements: A Stronger Case for a Subsurface Ocean at Europa". *Science* 289.5483, pp. 1340–1343.

Kruse, F. A. et al. (1993). "The spectral image processing system (SIPS)—interactive visualization and analysis of imaging spectrometer data". *Remote Sensing of Environment* 44.2–3, pp. 145–163.

Leblanc, F., R. E. Johnson, and M. E. Brown (2002). "Europa's Sodium Atmosphere: An Ocean Source?" *Icarus* 159.1, pp. 132–144.

Leonard, E. J., D. A. Patthoff, and D. A. Senske (2023). "The Europa Global Geologic Map". *USGS Scientific Investigations Map*.

Ligier, N. et al. (2016). "VLT/SINFONI Observations of Europa: New Insights into the Surface Composition". *The Astronomical Journal* 151.6, p. 163.

Loeffler, M. J. et al. (2011). "Radiolysis of Sulfuric Acid, Sulfuric Acid Monohydrate, and Sulfuric Acid Tetrahydrate and Its Relevance to Europa". *Icarus* 215.1, pp. 370–380.

Loeffler, M. J. et al. (2006). "Synthesis of Hydrogen Peroxide in Water Ice by Ion Irradiation". *Icarus* 180.1, pp. 265–273.

Mahjoub, A. et al. (2017). "Production of Sulfur Allotropes in Electron Irradiated Jupiter Trojans Ice Analogs". *The Astrophysical Journal* 846.2, p. 148.

McCord, T. B. et al. (1998). "Non-Water-Ice Constituents in the Surface Material of the Icy Galilean Satellites from the Galileo near-Infrared Mapping Spectrometer Investigation". *Journal of Geophysical Research: Planets* 103.E4, pp. 8603–8626.

McCord, T. B. et al. (1999). "Hydrated Salt Minerals on Europa's Surface from the Galileo near-Infrared Mapping Spectrometer (NIMS) Investigation". *Journal of Geophysical Research: Planets* 104.E5, pp. 11827–11851.

Met Office (2022). *Cartopy: A Cartographic Python Library with a Matplotlib Interface*. Version v0.21.1.

Modigliani, A. et al. (2007). "The SINFONI Pipeline". *arXiv preprint astro-ph/0701297*.

Moore, M. H., R. L. Hudson, and R. W. Carlson (2007). "The Radiolysis of SO2 and H2S in Water Ice: Implications for the Icy Jovian Satellites". *Icarus* 189.2, pp. 409–423.

Paranicas, C., R. W. Carlson, and R. E. Johnson (2001). "Electron Bombardment of Europa". *Geophysical Research Letters* 28.4, pp. 673–676.

Paranicas, C. et al. (2009). "Europa's Radiation Environment and Its Effects on the Surface". *Europa*. Ed. by R. T. Pappalardo, W. B. McKinnon, and K. Khurana. University of Arizona Press, Tucson AZ, p. 529.

Paranicas, C. et al. (2002). “The Ion Environment near Europa and Its Role in Surface Energetics”. *Geophysical Research Letters* 29.5, pp. 18-1–18-4.

Pospieszalska, M. K. and R. E. Johnson (1989). “Magnetospheric Ion Bombardment Profiles of Satellites: Europa and Dione”. *Icarus* 78.1, pp. 1–13.

Prockter, L. M. et al. (2002). “Morphology of Europan Bands at High Resolution: A Mid-Ocean Ridge-Type Rift Mechanism”. *Journal of Geophysical Research: Planets* 107.E5, pp. 4-1–4-26.

Prockter, L. M. and G. W. Patterson (2009). “Morphology and Evolution of Europa’s Ridges and Bands”. *Europa*. Ed. by R. T. Pappalardo, W. B. McKinnon, and K. Khurana. University of Arizona Press, Tucson AZ, pp. 237–258.

Shirley, J. H. et al. (2010). “Europa’s Ridged Plains and Smooth Low Albedo Plains: Distinctive Compositions and Compositional Gradients at the Leading Side–Trailing Side Boundary”. *Icarus* 210.1, pp. 358–384.

Strazzulla, G. (2011). “Cosmic Ion Bombardment of the Icy Moons of Jupiter”. *Nuclear Instruments and Methods in Physics Research Section B: Beam Interactions with Materials and Atoms* 269.9, pp. 842–851.

Strazzulla, G. et al. (2007). “Hydrate Sulfuric Acid after Sulfur Implantation in Water Ice”. *Icarus* 192.2, pp. 623–628.

Tribbett, P. D. and M. J. Loeffler (2022). “Thermal Reactions between H2S and O3: Implications for Europa Surface Chemistry”. *The Planetary Science Journal* 3.10, p. 233.

Trumbo, S. K. et al. (2022). “A New UV Spectral Feature on Europa: Confirmation of NaCl in Leading-Hemisphere Chaos Terrain”. *The Planetary Science Journal* 3.2, p. 27.

Trumbo, S. K., M. E. Brown, and K. P. Hand (2019a). “H2O2 within Chaos Terrain on Europa’s Leading Hemisphere”. *The Astronomical Journal* 158.3, p. 127.

– (2019b). “Sodium Chloride on the Surface of Europa”. *Science Advances* 5.6, eaaw7123.

– (2020). “Endogenic and Exogenic Contributions to Visible-Wavelength Spectra of Europa’s Trailing Hemisphere”. *The Astronomical Journal* 160.6, p. 282.

Virtanen, P., R. Gommers, T. E. Oliphant, et al. (2020). “SciPy 1.0: Fundamental Algorithms for Scientific Computing in Python”. *Nature Methods* 17, pp. 261–272.

Volwerk, M., M. G. Kivelson, and K. K. Khurana (2001). “Wave Activity in Europa’s Wake: Implications for Ion Pickup”. *Journal of Geophysical Research: Space Physics* 106.A11, pp. 26033–26048.

Chapter 3

PWYLL AND MANANNÁN CRATERS AS A LABORATORY FOR CONSTRAINING IRRADIATION TIMESCALES ON EUROPA

Davis, M. R. and M. E. Brown (2024). "Pwyll and Manannán Craters as a Laboratory for Constraining Irradiation Timescales on Europa". *The Planetary Science Journal* 5.5, p. 107.

Abstract

We examine high spatial resolution Galileo/NIMS observations of the young (~1 My - ~20 My) impact features, Pwyll and Manannán craters, on Europa's trailing hemisphere in an effort to constrain irradiation timescales. We characterize their composition using a linear spectral modeling analysis and find that both craters and their ejecta are depleted in hydrated sulfuric acid relative to nearby older terrain. This suggests that the radiolytic sulfur cycle has not yet had enough time to build up an equilibrium concentration of H_2SO_4, and places a strong lower limit of the age of the craters on the equilibrium timescale of the radiolytic sulfur cycle on Europa's trailing hemisphere. Additionally, we find that the dark and red material seen in the craters and proximal ejecta of Pwyll and Manannán show the spectroscopic signature of hydrated, presumably endogenic salts. This suggests that the irradiation-induced darkening and reddening of endogenic salts thought to occur on Europa's trailing hemisphere has already happened at Pwyll and Manannán, thereby placing an upper limit on the timescale by which salts are irradiation reddened.

3.1 Introduction

Europa's trailing hemisphere surface composition reflects a complex interplay between endogenic material present within the recently geologically active chaos terrains and linea (e.g. Dalton et al., 2012, 2005; McCord et al., 2010, 1999; Trumbo et al., 2020), exogenic material deposited by the Jovian magnetosphere (e.g. Cooper et al., 2001; Paranicas et al., 2001, 2009; Pospieszalska et al., 1989), and irradiation-induced alteration of both the endogenically and exogenically sourced material (e.g. Brown et al., 2013; Carlson et al., 1999; Trumbo et al., 2020). Endogenic material within the chaos terrains and linea, thought to contain salts exhumed from Europa's subsurface (e.g. Dalton et al., 2012, 2005; McCord et al., 2010, 1999; Trumbo et al., 2022, 2019), appear to be irradiation darkened and reddened on Europa's trailing hemisphere, turning progressively redder toward the trailing hemisphere apex where the irradiation flux is strongest (Carlson et al., 2009; Johnson et al., 1988; McEwen, 1986; Nelson et al., 1986). A classic example of irradiation-induced alteration of exogenic material is the so-called radiolytic sulfur cycle, where Iogenic sulfur ions captured in Jupiter's magnetosphere are deposited on Europa's trailing hemisphere and subsequent irradiation produces hydrated sulfuric acid (H_2SO_4) along with a variety of potential sulfur-bearing intermediary products in a "bull's-eye" pattern centered at the trailing hemisphere apex (0° N, 270° W) (Carlson et al., 2002, 2005, 1999). Because of the intense irradiation environment on Europa's trailing hemisphere, these sulfur-bearing compounds are expected to be in radiation-induced equilibrium, with H_2SO_4 continuously produced and destroyed in some steady state concentration (Carlson et al., 1999). The timescale for reaching this irradiation-induced equilibrium on Europa's trailing hemisphere is not well known, however various estimates based on laboratory experiments have suggested timescales on the order of $\sim 10^4$ yr (Carlson et al., 2002; Ding et al., 2013; Strazzulla, 2011; Strazzulla et al., 2007).

Young impact features may offer a unique opportunity for constraining irradiation timescales on Europa's trailing hemisphere. Pwyll crater and its ejecta, for example, show an enhancement in the UV-to-visible albedo ratio, which otherwise is anti-correlated with irradiation-induced discoloration on Europa's trailing hemisphere (Burnett et al., 2021). Burnett et al. (2021) suggest that the timescale for irradiation-induced discoloration on Europa must therefore be longer than the age of Pwyll crater. Hendrix et al. (2011) also found that a 280 nm absorption feature attributed to SO_2, a likely product of the radiolytic sulfur cycle, had a low band strength near Pwyll, with the band strength generally increasing away from the crater and toward

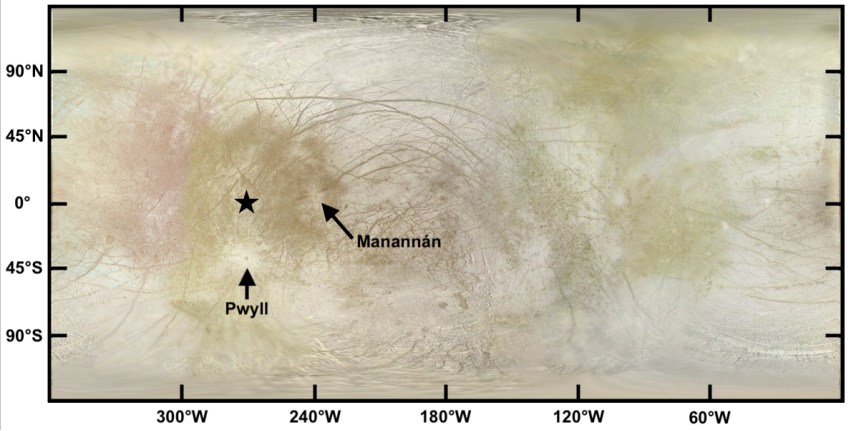

Figure 3.1: Global mosaic of Europa showing the locations of Pwyll and Manannán craters. Pwyll crater, one of Europa's youngest impact features, is ~27 km in diameter, surrounded by a dark ring of proximal ejecta, and has an extensive bright ray ejecta which extends as far as 1000 km and stands in stark contrast to the darker reddish surface of Europa's trailing hemisphere. Manannán crater is ~23 km in diameter, also has a dark, red ring of proximal ejecta, and is surrounded by a much less extensive bright ray system which extends up to ~120 km and covers nearby young terrain including chaos terrains in Dyfed Regio and the triple band Belus linea. The location of the trailing hemisphere apex (0°N, 270°W) is indicated with a star. This mosaic map, created by Steve Albers, blends an existing color map from NASA/JPL/Björn Jónsson created using color images from Voyager and Galileo, the high-resolution black and white mosaic from USGS, and additional higher resolution imagery from Galileo and Juno.

the older nearby chaos terrain. More recent work has revealed that Pwyll crater and its large ejecta blanket also lacks an unassigned absorption feature at 2.07 μm which appears to be formed via irradiation and is ubiquitous across the rest of Europa's trailing hemisphere (Davis et al., 2023).

Pwyll and Manannán craters are two of the youngest impact features on Europa. As can be seen in Figures 3.1 and 3.2 (a), Pwyll is a visually striking ~27 km diameter impact feature on Europa's trailing hemisphere (25°S, 271°W) with a dark, reddish crater center surrounded by extensive bright white ejecta with rays that extend up to 1000 km from the impact site (Moore et al., 1998). It has a dark, red, pedestal-like proximal ejecta with an outward-facing steep slope or scarp which extends approximately half a crater diameter from the rim (Moore et al., 1998) and is thought to contain endogenic material excavated from a depth of ~1 km (Fanale et al., 2000) (see Figure 3.2 (a) and (b)). As can be seen in the global map of Europa (Figure 3.1), Pwyll is the only large crater which still has such an extensive ray system (Bierhaus et al., 2009), which overlaps nearby chaos terrains in Dyfed Regio

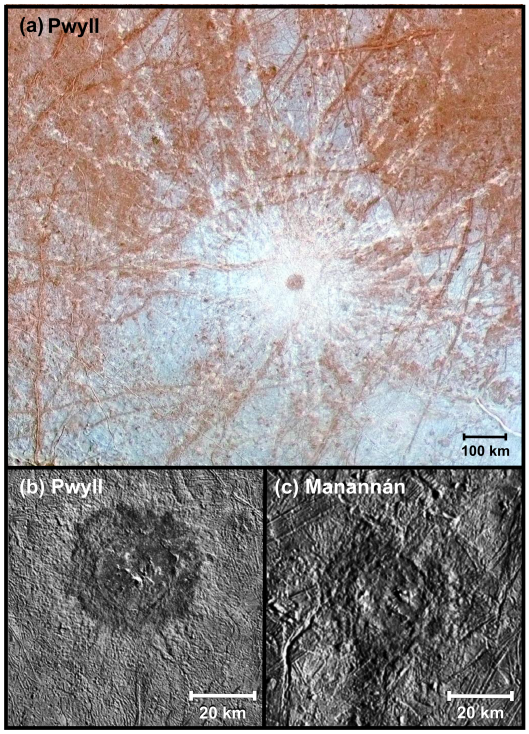

Figure 3.2: (a) Enhanced color image constructed from Galileo/SSI images of Pwyll crater and the surrounding regions on Europa's trailing hemisphere. The dark, red crater and proximal ejecta are seen near the center of the image surrounded by an extensive bright ejecta blanket with rays extending over a thousand kilometers from the impact site. This bright ice-rich ejecta stands in stark contrast to the darker, reddish surface of Europa's trailing hemisphere. This image is from NASA/JPL/University of Arizona. (b) Galileo/SSI image of Pwyll crater, taken with the clear filter. This image is from NASA/JPL/DLR. (c) Galileo/SSI image of Manannán crater taken with the clear filter. This image is from NASA/JPL/DLR. In all three panels, north is towards the top of the image. For panels (b) and (c), the sun illuminates the surface from the right.

and Annwn Regio (Doggett et al., 2009), suggesting it is likely to be very young. Indeed, estimates for its age range from $\lesssim$1–18 Myr (Bierhaus et al., 2001, 2009).

Manannán crater (3°N, 240°W), shown in Figures 3.1 and 3.2 (c), has a crater diameter of ~23 km (Moore et al., 1998). It has a partially preserved dark, red ring of proximal ejecta which may contain material excavated from Europa's subsurface that correlates with a pedestal-like slope break ~7 km beyond the crater rim (Moore et al., 1998). Lower-lying regions on the crater floor are bluer than the surrounding material and proximal ejecta, suggesting an origin as impact melt (Moore et al., 2001; Schenk et al., 2009). The rim is generally weakly expressed and even absent in some areas (Schenk et al., 2009), with evidence for lobate flows of material over the rim (Moore et al., 2001, 1998). Bright ray ejecta is seen extending up to ~120 km from the impact, covering nearby chaos terrain in Dyfed Regio as well as part of the nearby triple band Belus linea, suggesting that Manannán is younger than all of the nearby terrains (Moore et al., 1998). However, based on ray preservation, Manannán is expected to be older than Pwyll because at similar solar illumination, Manannán's bright rays are much less prominent, significantly more degraded, and

they cover a much smaller region (Moore et al., 2001; Schenk et al., 2009).

In this chapter, we investigate the composition of the Pwyll and Manannán impact features using existing high-spatial-resolution Galileo/Near-Infrared Mapping Spectrometer (NIMS) observations. We perform a simple linear spectral modeling analysis in order to better understand the composition of these craters and attempt to constrain irradiation timescales on Europa's trailing hemisphere.

3.2 Data Analysis

We used the highest-spatial-resolution data available from Galileo/NIMS and associated images from the Solid State Imager (SSI) in order to examine the composition of Pwyll and Manannán craters and the surrounding regions, with the aim of gaining insight into the various irradiation timescales operating on Europa's trailing hemisphere. In particular, we used a linear spectral modeling approach to explore the spatial distribution of water-ice, hydrated sulfuric acid, and salty "non-ice" material in and around each crater and its ejecta.

Galileo/SSI

Bland et al. (2021) recently updated the available Galileo/SSI dataset of Europa to account for uncertainties in the spacecraft's position and pointing which resulted in poor alignment of overlapping images, with some images displaced by more than 100 km from their correct location. We used the individual processed and projected "level 2" Galileo/SSI images with updated spatial information from Bland et al. (2021), which we acquired from the USGS-hosted SpatioTemporal Asset Catalog (STAC, https://stacspec.org/). We selected three images for our analysis. The first is a cutout from a larger image taken on 19 December 1996. We selected a region near Pwyll crater which covers an area ~700 km wide with a spatial resolution ~1.3 km/pixel and shows the low-albedo crater and proximal ejecta surrounded by an extensive blanket of bright ray ejecta. The second image, taken on 16 December 1997, shows a close-up view of Pwyll, including the dark crater and proximal ejecta at a spatial resolution of ~150 m/pixel. The last image, taken on 29 March 1998, shows Manannán crater, Belus linea, and the surrounding region at a spatial resolution of ~1.65 km/pixel. All of the selected SSI images were taken with the clear filter at a relatively high solar illumination angle, which allowed for the best visible contrast between the dark material in the craters and proximal ejecta and the higher-albedo material of the bright ray systems. These SSI images can be seen in Figure 3.5 (a), (d), and (g), respectively.

Galileo/NIMS

We used both of the existing high-spatial-resolution Galileo/NIMS observations of Pwyll crater and its ejecta. The first is NIMS cube 12ENCPWYLL01A taken on 16 December 1997 which covers the crater, the dark proximal ejecta, and only a very small amount of the surrounding bright ray ejecta at a spatial resolution of ∼1.5 km/pixel. We also used NIMS cube E6ENSUCOMP01A taken on 20 February 1997 which covers a larger area to the west of Pwyll crater and includes the bright ray ejecta and some older background terrain at a spatial resolution of ∼4.5 km/pixel. Finally, we used NIMS cube C3ENLINEA01B taken on 6 November 1996 which covers Manannán crater, its ejecta, and much of the surrounding terrain, including Belus linea, at a spatial resolution of ∼11 km/pixel. The NIMS cube 12ENCPWYLL01A has been previously analyzed by Fanale et al. (2000), while the other two NIMS observations have remained unpublished. The data were downloaded from the NASA Planetary Data Archive (Carlson, 1998) as calibrated I/F mosaics. From the Galileo/NIMS spectral image cubes PDS data set (Carlson, 1998), we used the individual PDS products E6ENSUCOMP01A-MSY02.IOF, 12ENCPWYLL01A-MSY02.IOF, and C3ENLINEA-01B-MSY04.IOF.

The included spatial information was calculated based on projection onto Europa according to spacecraft position, target position, and scan platform orientation, which are known to have relatively large uncertainties. We found that there were small offsets between the spatial information in the NIMS cubes and the recently updated SSI images from Bland et al. (2021). We therefore applied small shifts in latitude and longitude to each of the NIMS data cubes to more closely match the SSI images. We empirically determined the optimal offsets using the results of our linear spectral modeling efforts (see Section 3.2 below). In particular, we mapped the total water-ice abundance of each pixel where the higher water-ice abundances should correspond to the higher-albedo regions such as the bright ray ejecta in the SSI images (e.g. Fanale et al., 2000) and the lower water-ice abundances correspond with the darker, less icy regions such as the crater interior, proximal ejecta, and older background terrains. The shapes of the bright ray ejecta are taken from Leonard et al. (2024). We applied an offset of -0.25° in latitude and $+0.75^\circ$ in longitude for cube 12ENCPWYLL01A, $+0.2^\circ$ in latitude and -0.25° in longitude for cube E6ENSUCOMP01A, and -0.75° in latitude and -0.75° in longitude for cube C3ENLINEA01B. All of these applied offsets are small when compared with the field of view for their respective observations.

Species	Formula	Grain Size	Temp.	Source
Water-ice	Crystalline	5, 50, 200, 1000 µm	120 K	Mastrapa et al. (2008)
(refractive indices)	Amorphous	5, 50, 200, 1000 µm	>70 K	"
Sulfuric acid	$H_2SO_4{\cdot}6.5H_2O$	50 µm	80 K	Carlson et al. (1999)
	$H_2SO_4{\cdot}8H_2O$	5, 50 µm	80 K	"
Magnesium chloride	$MgCl_2{\cdot}2H_2O$		80 K	Hanley et al. (2014)
	$MgCl_2{\cdot}4H_2O$		80 K	"
	$MgCl_2{\cdot}6H_2O$		80 K	"
Magnesium chlorate	$Mg(ClO_3)_2{\cdot}6H_2O$		80 K	"
Magnesium perchlorate	$Mg(ClO_4)_2{\cdot}6H_2O$		80 K	"
Magnesium sulfate	$MgSO_4$ (*aq*)	50–100 µm	100 K	Dalton et al. (2005)
Hexahydrite	$MgSO_4{\cdot}6H_2O$	50–100 µm	100 K	"
Epsomite	$MgSO_4{\cdot}7H_2O$	25–200 µm	120 K	Dalton et al. (2012)
Mirabilite	$Na_2SO_4{\cdot}10H_2O$	50–100 µm	100 K	Dalton et al. (2005)
Sodium chloride	NaCl		80 K	Hanley et al. (2014)
Sodium perchlorate	$NaClO_4$		80 K	Hanley et al. (2014)
	$NaClO_4{\cdot}2H_2O$		80 K	"

Table 3.1: Laboratory spectra used in our linear spectral modeling analysis, based on the spectral library of King et al. (2022). When available, the temperature and grain size of each laboratory spectrum is listed.

Spectral Modeling

We performed a simple linear spectral modeling analysis to explore the relative contributions of water-ice, hydrated sulfuric acid, and salts to the spectra in and around Pwyll and Manannán craters. We based our spectral library on that of King et al. (2022), who modeled much of Europa's surface from a combination of global Galileo/NIMS and Very Large Telescope/SPHERE observations. This spectral library includes crystalline and amorphous water-ice, several hydration states of sulfuric acid, and a variety of cryogenic salts. The specific laboratory spectra included in the library and their relevant properties are listed in Table 3.1. Water-ice spectra, for both crystalline and amorphous water-ice, were calculated using laboratory optical constants (Mastrapa et al., 2008) and the Shkuratov model (Shkuratov et al., 1999) for grain sizes of 5 µm, 50 µm, 200 µm, and 1 mm and a volume filling fraction of 0.7.

Each NIMS spectrum was analyzed by fitting a linear combination of laboratory

spectra from the reference library (Table 3.1), where the model spectrum, M_λ, is described by

$$M_\lambda = C \sum_i w_i \cdot S_{i,\lambda} \quad \text{where} \quad \sum_i w_i = 1 \tag{3.1}$$

where w_i are the weights associated with each laboratory end-member spectrum, S_i. The additional scalar scaling factor, C, accounts for small variations in the reflectance between the calibrated NIMS observations and the measured laboratory spectra. These differences may be due to photometric effects caused by differing illumination of the laboratory samples and Europa's surface, as well as errors associated with the use of a linear mixing model. Typical values of C range from ~0.4–0.7 for NIMS cube 12ENCPWYLL01A, ~0.3–0.5 for NIMS cube E6ENSUCOMP01A, and ~0.8–1.2 for NIMS cube C3ENLINEA01B. We used the non-negative least squares algorithm implemented in SciPy v1.10.1 to solve for the best-fit spectral model at each NIMS pixel.

We map the relative contribution of sulfuric acid and salts to the best-fit spectral models for each NIMS cube. We calculate the abundance of sulfuric acid in each pixel by summing the individual coefficients of all three laboratory sulfuric acid spectra, which have different grain sizes and hydration states. Similarly, we report the relative abundance of the "salty" material by summing the coefficients of all of the salts included in our spectral library. While our library includes a variety of hydrated salts which are potentially present on Europa's surface, the specific composition of Europa's dark endogenic material is not well known. The near-infrared spectra of Europa's dark hydrate material, as well as many of the candidate salt species, are mainly characterized by asymmetric distortions to the water-ice bands and lack specific characteristic absorptions. This lack of distinguishing spectral features, particularly at the low spectral resolution of NIMS, results in degeneracies between various salt endmembers, which make positive identification of specific species on Europa's surface difficult (e.g. King et al., 2022). We therefore choose not to report the specific coefficients for each individual salt, but rather only consider the total contribution of the non-water-ice and non-sulfuric-acid "salty" hydrated material to the spectral model, hereafter referred to as the salt abundance.

The measurement uncertainty in the NIMS observations is not well known, and the influence of non-quantifiable radiation noise means that a simple error estimate based on the inherent scatter of each spectrum cannot robustly predict the true error. We therefore adopt a Monte Carlo bootstrap method to estimate the error in our model abundances, where we use the idea of a constant chi-squared boundary to

predict the 1σ confidence limit for each of our model weights, as described in Press et al. (1992) section 15.6. We first use a bootstrap sampling method to generate 1000 synthetic spectra for each NIMS spectrum, with the same number of data points as the original spectrum, by drawing N (wavelength, I/F) pairs with replacement from the original spectrum. We then use the same spectral library and chi-squared minimization algorithm as before to estimate a new set of model abundances for each synthetic spectrum and calculate a set of corresponding chi-squared values, with respect to the original NIMS spectrum for which we want to find error bars. Each of these new chi-squared values, calculated for a set of model coefficients which have been perturbed away from the best-fit abundances, are necessarily larger than the minimum chi-squared for the original NIMS spectrum. As described in Press et al. (1992), there is some region within which the χ^2 value increases by no more than a set $\Delta\chi^2$ which defines an M-dimensional confidence region. We find the approximate location of the constant $\Delta\chi^2$ boundary that corresponds to the 1σ confidence region by considering the range of model abundances which have a corresponding chi-squared value in the lowest 68% of the set of chi-squared values. We then use the range of model abundances present in the set to estimate 1σ error bars for each of the M model abundances corresponding to the specific library spectra, as well as the error bars for our combined compositional categories of water-ice, sulfuric acid, and salts. These estimated 1σ error bars are reported throughout the paper along with the best-fit abundance values.

3.3 Results

Figure 3.3 shows average NIMS spectra for specific compositional units along with their best-fit spectral models for Pwyll (panel a) and Manannán (panel b), respectively. The NIMS pixels included in each average spectrum are shown in the inset maps. The best-fit model abundances for sulfuric acid, salts, and water-ice for each of these average spectra are reported in Table 3.2 and shown graphically in Figure 3.4. The estimated 1σ error bars are included in Table 3.2. We note that NIMS cube E6ENSUCOMP01A, which includes many of the bright ray ejecta pixels and all of the background terrain pixels near Pwyll, was taken with a lower spectral resolution (~0.026 μm) than the other cube which covers Pwyll crater and the proximal ejecta (~0.015 μm). To compute the average spectrum for Pwyll's bright ray ejecta, which includes pixels in both NIMS cubes, we interpolate the lower-resolution spectra to match the wavelengths of the higher-resolution observation.

In Figure 3.3 (a), the average spectra of the Pwyll crater interior and proximal ejecta

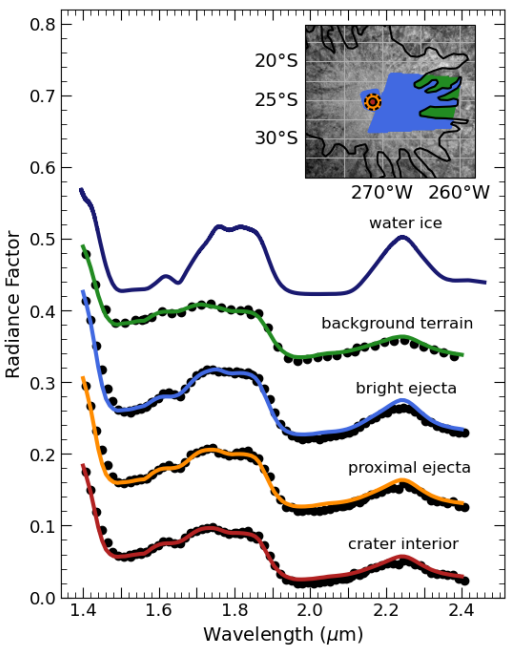

Figure 3.3 (a): Average spectra of Pwyll crater, its dark proximal ejecta, bright ray ejecta, and the nearby surrounding terrain along with their best-fit spectral models. The NIMS pixels included in the average spectra are shown in the inset map with the crater interior in red, the dark proximal ejecta in orange, the bright ray ejecta in blue, and the older background terrain in green. A laboratory-derived spectrum of pure water-ice with 200 μm grains from Mastrapa et al. (2008) is also included for comparison. For clarity, the spectra are offset by +0.0, +0.1, +0.2, +0.3, and +0.4, respectively.

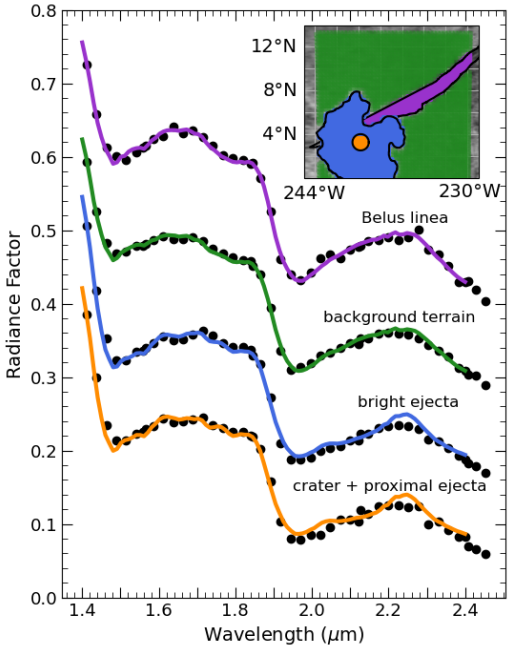

Figure 3.3 (b): Average spectra and best-fit spectral models of Manannán crater and its dark proximal ejecta, bright ray ejecta, and the nearby surrounding terrain along with Belus linea. The NIMS pixels included in the average spectra are shown in the inset map with the crater interior and dark proximal ejecta in orange, the bright ray ejecta in blue, the older background terrain in green, and Belus linea in purple. For clarity, the spectra are offset by +0.0, +0.1, +0.2, and +0.3, respectively.

show strong distortions to the water-ice absorption bands, particularly in the ~2–2.2 μm range, which is indicative of hydrated, presumably endogenic salts while the bright ray ejecta most closely resembles a pure water-ice spectrum. The low-albedo material in the crater and proximal ejecta are apparently enriched in salts relative to the bright ray ejecta. Indeed, the best-fit spectral model for the average spectrum of the crater and proximal ejecta show an abundance of salts (11^{+15}_{-8}% and 10^{+12}_{-9}%) which is around twice that of the average spectrum of the bright ray ejecta (5^{+20}_{-5}%). The spectral signature of hydrated sulfuric acid can be seen most prominently in the average spectrum of the older background terrain, which has a model abundance of

	Sulfuric Acid	Salts	Water-Ice
Pwyll (Figure 3.3 (a)):			
Crater interior	24^{+14}_{-14}%	11^{+15}_{-8}%	65^{+7}_{-26}%
Proximal ejecta	22^{+15}_{-14}%	10^{+12}_{-9}%	68^{+9}_{-21}%
Bright ray ejecta	24^{+13}_{-19}%	5^{+20}_{-5}%	71^{+12}_{-17}%
Background terrain	44^{+12}_{-29}%	17^{+26}_{-10}%	39^{+23}_{-25}%
Manannán (Figure 3.3 (b)):			
Crater+proximal ejecta	41^{+11}_{-22}%	29^{+32}_{-10}%	30^{+25}_{-17}%
Bright ray ejecta	45^{+11}_{-25}%	26^{+22}_{-24}%	29^{+24}_{-16}%
Background terrain	55^{+8}_{-21}%	42^{+7}_{-20}%	3^{+16}_{-3}%
Belus linea	45^{+19}_{-26}%	47^{+14}_{-19}%	8^{+27}_{-8}%

Table 3.2: Best-fit spectral modeling results for the average spectra of specific compositional units of the Pwyll and Manannán regions from Figure 3.3. The estimated 1σ confidence region for the best-fit model abundances are also reported.

44^{+12}_{-29}% sulfuric acid, as compared with 22^{+15}_{-14}–24^{+13}_{-19}% sulfuric acid found in the average crater and ejecta spectra. This suggests that Pwyll crater and its ejecta are depleted in sulfuric acid relative to the older nearby terrain.

The NIMS observations of Manannán crater are at sufficiently low spatial resolution (~11 km/pixel) that it is difficult to distinguish between the crater interior and dark proximal ejecta. We therefore combine these units and consider the crater interior and proximal ejecta together. As seen in 3.3 (b) and Figure 3.4, the average spectrum of the crater/proximal ejecta and bright ray ejecta of Manannán appear to be somewhat depleted in sulfuric acid (41^{+11}_{-22}% and 45^{+11}_{-25}%) relative to the nearby background terrain (55^{+8}_{-21} %), although less significantly than at Pwyll crater. The average spectrum of the nearby Belus linea is also depleted in sulfuric acid when compared with the background terrain. Additionally, the average spectrum of the Manannán crater and proximal ejecta, as well as the bright ray ejecta, appear to contain a higher abundance of salts than is seen at Pwyll. At both Pwyll and Manannán, the average background terrain spectra have a higher best-fit abundance of salt than the crater and ejecta material, although there is a significantly higher salt abundance seen in the background terrain near Manannán (42^{+7}_{-20}%) than Pwyll (17^{+26}_{-10}%). Belus linea contains an even stronger salt signature (47^{+14}_{-19}%) than the

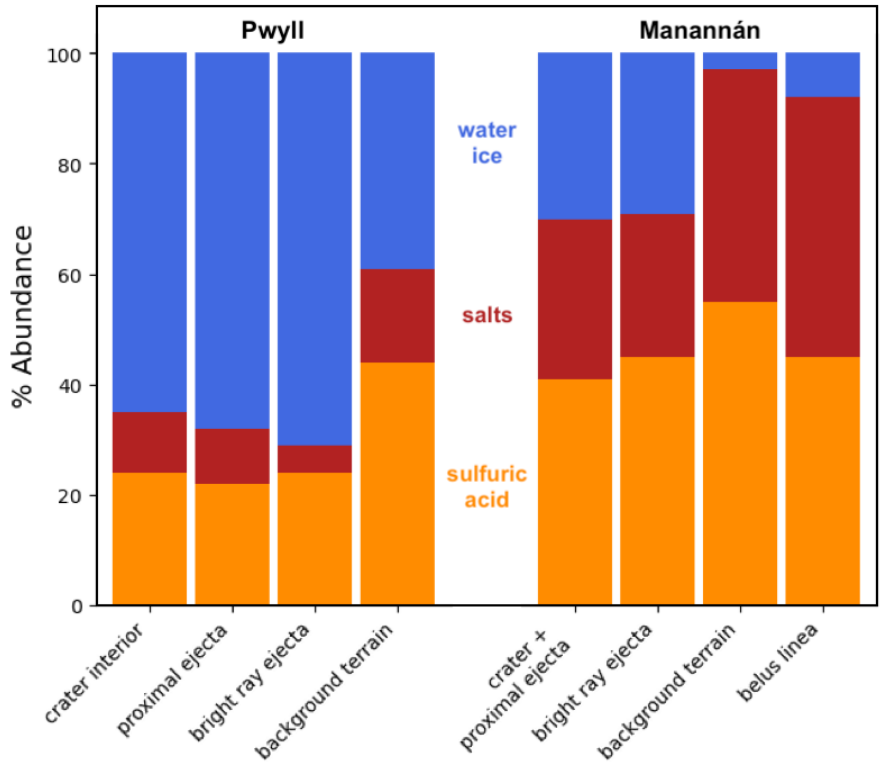

Figure 3.4: Abundance values for the best-fit spectral models of the average spectra of specific geologic units in the Pwyll and Manannán regions. These abundance values and estimated 1σ error bars are reported in Table 3.2 and correspond to the models shown in color in Figure 3.3. At both Pwyll and Manannán, the average spectra of the crater, proximal ejecta, and bright ray ejecta are all depleted in sulfuric acid relative to the background terrain. The dark material in both of the craters and proximal ejecta contain a higher abundance of salts than the bright ray ejecta, although the background terrains appear to have the highest concentration of salty material. Manannán crater and the surrounding region shows a higher concentration of both salts and sulfuric acid, and therefore less pure water-ice than Pwyll.

background terrain near Manannán.

Figure 3.5 maps the pixel-specific results of our linear spectral modeling analysis for hydrated sulfuric acid, the non-ice, non-sulfuric-acid "salty" component, and water-ice, respectively. The compositional trends seen in the average spectra of Figure 3.3 are generally consistent with those seen in the compositional maps of Figure 3.5, although the additional spatial information in the compositional maps provides further insight. As can be seen in Figure 3.5 (b), (f), and (j), Pwyll and Manannán craters, their dark proximal ejecta, and their bright ray ejecta are all depleted in sulfuric acid relative to the nearby background terrains, as expected based on the average spectra shown in Figure 3.3. At Pwyll, the crater and proximal

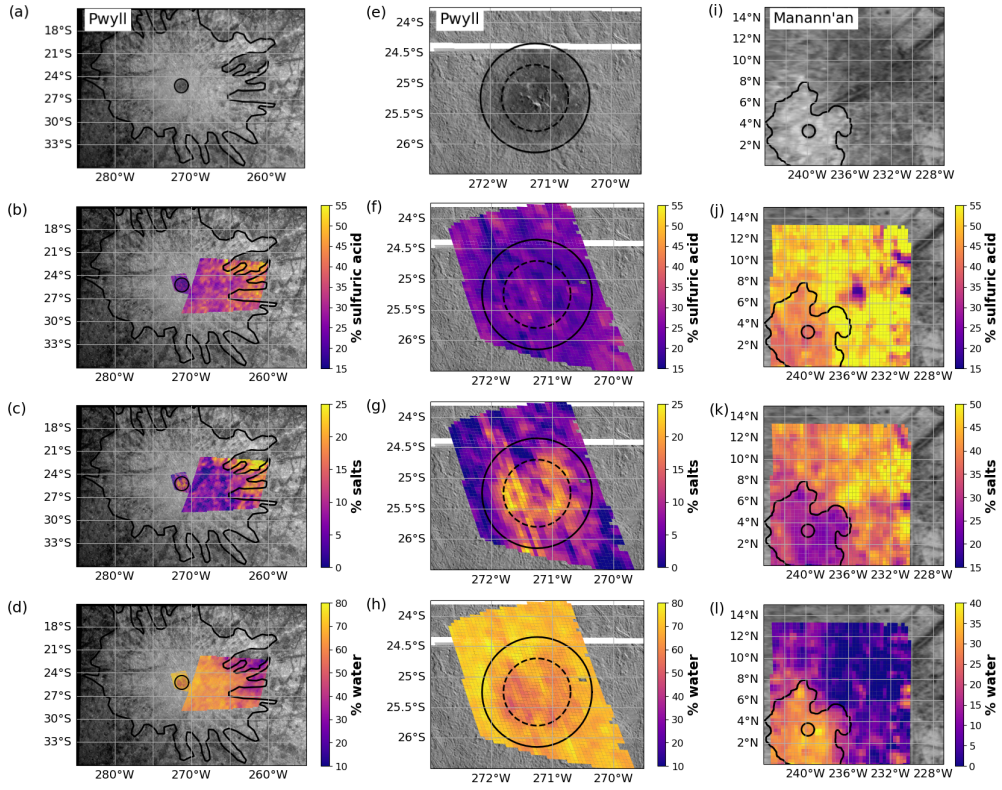

Figure 3.5: Sulfuric acid, salt, and water-ice concentration maps for Pwyll and Manannán craters. Panels (a) and (e) show the Galileo/SSI images of Pwyll crater, with the estimated sulfuric acid abundance from the corresponding NIMS cubes displayed in panels (b) and (f), the salt abundance in panels (c) and (g), and the water-ice abundance in panels (d) and (h). The crater rim is shown as the dashed circle, the extent of the dark proximal ejecta is indicated by the solid circle, and the bright white ejecta blanket is outlined in solid black. Likewise, panel (i) shows the SSI image of Manannán crater and the corresponding sulfuric acid, salt, and water-ice maps are shown in panels (j), (k), and (l), respectively. The extent of the dark ejecta is indicated by the solid circle, and the bright white ejecta blanket is outlined in black. The maps report the percent contribution of sulfuric acid, salts, or water-ice to the best-fit linear spectral model for each NIMS pixel. Note the different scale bars between the Pwyll and Manannán maps. Both Pwyll and Manannán craters and their ejecta appear to be depleted in sulfuric acid relative to nearby older terrains, suggesting that the radiolytic sulfur cycle has not yet had enough time to reach an equilibrium concentration of H_2SO_4 at either crater. At both Pwyll and Manannán, the crater and dark proximal ejecta appear to be enriched in salts relative to the bright white ejecta blanket, suggesting that the dark material exhumed by the impacts is relatively salt-rich. The dark albedo and reddish coloration seen in the SSI images of both craters suggests that this salty material has already been irradiation reddened. As seen in panels (j) and (k), the nearby triple band, Belus linea, is significantly enhanced in salts and depleted in sulfuric acid relative to the background terrain.

ejecta have best-fit modeled sulfuric acid abundances ranging from ~15–35%, while the bright ray ejecta ranges from ~20–40%, and the older background terrain ranges from ~40–55%. There appears to be a slight gradient in the sulfuric acid abundance of the bright ray ejecta, with higher sulfuric acid concentrations farther from the crater. The bright ray ejecta also appears to be relatively optically thin, with some portions of the darker background terrain showing through in Figure 3.5 (a). This is consistent with the continuous ejecta blanket becoming progressively thinner at greater distance from the crater, and an increasing contribution to the spectrum from the underlying terrain increasing the measured sulfuric acid abundance. There are also small regions of somewhat enhanced sulfuric acid concentration (up to ~40%) within the bright ray ejecta which roughly correlate with darker patches in the SSI image where the underlying, older terrain shows through. It is also possible that sulfuric acid already present on the older terrain has been partially mixed into the bright ejecta blanket, perhaps through impact gardening. In either case, we expect that the slight increase in sulfuric acid concentration within Pwyll's bright ray ejecta, particularly in regions farther from the crater, is likely due to the older terrain showing through.

As shown in Figure 3.5 (j), the Manannán crater/proximal ejecta and bright ray ejecta are also clearly depleted in sulfuric acid relative to the background terrain. The background terrain has a modeled sulfuric acid abundance which ranges from ~45–65%, while the crater/proximal ejecta show modeled sulfuric acid abundances from ~35–45% and the bright ray ejecta ranges from ~35–55%. Like at Pwyll, Manannán's bright ray ejecta shows a stronger signature of sulfuric acid farther from the crater, where it is more optically thin, indicating there is likely to be a contribution from the underlying terrain. Additionally, the Manannán crater and ejecta appear to be somewhat less depleted in sulfuric acid than Pwyll crater and its ejecta, relative to their respective backgrounds. This is consistent with Manannán's older age, and thus more time for the radiolytic sulfur cycle to have produced hydrated sulfuric acid at Manannán. It is interesting to note that the triple band, Belus linea, is also depleted in sulfuric acid (panel j). While Belus linea must be older than the Manannán impact, it appears to be even more depleted in sulfuric acid, particularly near (235°W, 7°N) where there is a circular patch of low-albedo material with sulfuric acid concentrations as low as 14^{+5}_{-5}%. The large amount of endogenic "salty" material within the triple band, as seen in Figure 3.5 (k), may inhibit the radiolytic production of sulfuric acid, although we cannot rule out the possibility of post-impact geologic processes having altered the composition of this

area.

As can be seen in Figure 3.5 (c) and (g), the Pwyll bright ray ejecta has a very low concentration of salts, ranging from ~0–10%, while the crater itself and dark proximal ejecta are relatively enhanced in salts, with modeled abundances between ~10–25%. Parts of the older background terrain near Pwyll also show a high concentration of salts, with abundances ranging from ~10–25%. Figure 3.5 (k) reveals that the Manannán crater and ejecta as well as the nearby background terrain generally have a higher salt concentration than Pwyll, consistent with the average spectra shown in Figure 3.3. The Manannán crater and proximal ejecta show concentrations ranging from ~25–35%. While the salt concentration of the bright ray ejecta ranges from ~20–35%, the brighter and thicker regions of the ray ejecta closest to the crater show the lowest salt abundances (~20–25%), suggesting that the background terrain may be contributing to the measured salt abundance in the thinner or more heavily degraded regions of the bright ray ejecta. If we consider the salt abundance of the bright ray ejecta closest to the crater, the Manannán dark crater/proximal ejecta appears to be enhanced in salts relative to the bright ray ejecta. At both Pwyll and Manannán, the low-albedo material in the crater and proximal ejecta have a higher concentration of salts than the higher-albedo material in the bright ray ejecta, suggesting that the low-albedo material thought to be excavated from Europa's subsurface likely contains endogenic salts. This is consistent with the analysis of Fanale et al. (2000) who found that the visually dark and red material in the Pwyll crater floor and proximal ejecta correspond with a spectrally red unit characterized by asymmetric absorption bands. The background terrain near Manannán is quite salty, with abundance values ranging from ~30–50%, likely due to endogenic material present within the Dyfed Regio chaos terrains. The highest salt concentrations are seen in the Belus linea triple band, with concentrations ranging from ~45–55%. We note that while there appears to be some instrumental artifacts and correlated noise in the NIMS observations (e.g. possible vertical striping in panel (g)), the magnitude of these artifacts are smaller than the contrast seen in the model abundances between the different geologic units and should therefore have a minimal effect on our scientific results.

3.4 Discussion

Sulfuric Acid Production

At both Pwyll and Manannán, the dark material in the crater floor and proximal ejecta, and the bright ray ejecta blankets are depleted in sulfuric acid relative to

nearby older terrain. Pwyll, the younger of the two craters, appears to be more significantly depleted in sulfuric acid. Assuming the background terrain concentrations represent the equilibrium concentration of sulfuric acid for the irradiation environment near each crater, this suggests that the radiolytic sulfur cycle has not yet had enough time to build up an equilibrium concentration of H_2SO_4 at either Pwyll or Manannán. This is consistent with the results of Hendrix et al. (2011), who found that a 280 nm absorption feature attributed to SO_2, a possible byproduct of the radiolytic sulfur cycle, had a lower band strength near Pwyll with increasing band depth farther from the crater. Together, these results place a strong lower limit of the age of Pwyll and Manannán craters on the equilibrium timescale of the sulfuric acid cycle operating on Europa's trailing hemisphere.

While the exact ages of Pwyll and Manannán craters remain unknown, we can use their estimated ages and make some simplifying assumptions to calculate a rough, order of magnitude estimate for the equilibrium timescale of Europa's radiolytic sulfur cycle. Bierhaus et al. (2001) estimate Pwyll is ~3-18 Myr old based on solar system cratering rates. However, estimates of ion sputtering erosion from Paranicas et al. (2001) indicate that the top 1 cm of ice should be redistributed in approximately 0.6 Myr, which we would expect to degrade Pwyll's hemisphere-crossing bright rays and suggests that Pwyll may be even younger, perhaps less than 1 Myr (Bierhaus et al., 2009). This young age is consistent, within a factor of 2, with the Zahnle et al. (2003) estimate that a 20 km crater should form once every ~2 Myr and that Pwyll appears to be the freshest and youngest large crater on Europa. While a concrete age estimate for Manannán crater does not exist in the literature, Manannán is expected to be relatively young, postdates all nearby terrains including Belus linea, and likely formed under similar ice shell properties as Pwyll (Schenk et al., 2009), suggesting it may be the second youngest crater >20 km on Europa. We therefore use the cratering rates of Zahnle et al. (2003) to roughly estimate its age to be ~2 Myr older than Pwyll. This is generally consistent with its observed limited rays, which may be the remnants of a once larger ray system which have subsequently been degraded by sputtering erosion, but has not yet fully degraded.

Considering the low end of the age estimates for Pwyll and Manannán, we assume that Pwyll is ~1 Myr old and Manannán is ~3 Myr old. We now carry out a very simple calculation to estimate a lower bound on the equilibrium timescale of the sulfuric acid cycle on Europa. As seen in Figure 3.5, Pwyll appears to have reached a sulfuric acid concentration which has a model abundance of ~50% the

equilibrium abundance of the background terrain. If we assume that a 50% deficit in the best-fit spectral model corresponds to a 50% deficit in the physical concentration of sulfuric acid, then, assuming a linear growth in concentration, we would expect it to take at least 2 Myr to reach the equilibrium concentration at Pwyll. Similarly, the Manannán crater and ejecta has a sulfuric acid abundance of ~70% of its equilibrium abundance. If it has taken ~3 Myr to produce this amount of sulfuric acid, then we might expect to reach an equilibrium concentration at Manannán after ~4.3 Myr. Taking these together, we suggest that the equilibrium timescale for the radiolytic sulfur cycle on Europa's trailing hemisphere is likely to be at least a few million years, and perhaps even longer depending on the true ages of Pwyll and Manannán craters.

It is important to note that the equilibrium timescale for the radiolytic sulfur cycle may not be consistent across Europa's trailing hemisphere. Differences in the flux of bombarding particles and changes in the surface composition may lead to differences in the equilibrium concentration of hydrated sulfuric acid and the timescale for reaching that concentration. Pwyll and Manannán are located at similar angular distances from the trailing hemisphere apex (25° and 30°, respectively). We therefore expect both craters to receive a similar flux of cold sulfur ions, based on the irradiation models of Cassidy et al. (2013), who suggest that the flux of cold sulfur plasma to Europa's trailing hemisphere drops off by a $\cos\theta$ relationship, where θ is the angular distance from trailing apex. However, in our simple spectral models the background terrain near Manannán has a higher equilibrium concentration of hydrated sulfuric acid (~50-65%) than the terrain near Pwyll (~40-55%), consistent with the overall distribution of sulfuric acid hydrate found by Ligier et al. (2016). This suggests that the equilibrium concentration of sulfuric acid, and likely the timescale to reach that concentration, may depend on more than the sulfur ion flux. For example, the flux of 0.1–25 MeV electrons, as estimated by Paranicas et al. (2009), is expected to be higher at Manannán than Pwyll and may help explain the higher equilibrium concentration of sulfuric acid near Manannán. This is consistent with the hypothesis proposed by Dalton et al. (2013) that the production and steady-state concentration of hydrated sulfuric acid may depend on both the concentration of iogenic sulfur ions and the flux of energetic electrons.

Laboratory estimates for the sulfur cycle equilibrium timescale on Europa's trailing hemisphere are typically ~10^4 yr (e.g. Carlson et al., 2002; Ding et al., 2013; Strazzulla et al., 2007). However, our results suggest that it may take several orders

of magnitude longer to reach an equilibrium concentration of H_2SO_4 on Europa. It is very unlikely that both Pwyll and Manannán craters are young enough to be consistent with a sulfuric acid equilibrium timescale of a few thousand years, so we must conclude that the equilibrium timescale for the radiolytic sulfur cycle is significantly underestimated by these laboratory estimates. Strazzulla et al. (2007) and Ding et al. (2013) calculate these timescales using their experiment-derived reaction rates, estimates for the column density of hydrated H_2SO_4 molecules in the observable surface layers on Europa from Carlson et al. (1999), and estimates for the KeV-MeV sulfur ion flux from Cooper et al. (2001) and Dalton et al. (2013), respectively. These calculations would therefore underestimate the equilibrium timescale if the actual sulfuric acid column density at Europa was higher than that estimated by Carlson et al. (1999), or if the real sulfur ion flux is lower than that estimated by Cooper et al. (2001) and Dalton et al. (2013). However, it is difficult to achieve a 2 order of magnitude increase in the equilibrium timescale by simply adjusting the sulfuric acid column density and sulfur ion flux, which suggests that understanding the discrepancy between our observational constraints and the equilibrium timescales derived from laboratory experiments may require more careful analysis.

Laboratory experiments must necessarily replicate Europa's irradiation environment over much shorter timescales, perhaps reaching an equivalent irradiation dose of a few thousand to a million years on Europa in a matter of hours. Additionally, most laboratory experiments are performed for a single bombarding particle and energy, while various species and energies are acting simultaneously at Europa. Indeed, laboratory experiments have demonstrated that the specific intermediary products and steady-state concentration of H_2SO_4 may depend strongly on the temperature, energies, and projectiles involved (e.g. Loeffler et al., 2011; Moore et al., 2007; Strazzulla et al., 2007). Thus, using a laboratory-derived reaction rate for a single bombarding particle and energy may not provide a robust estimate for the actual equilibrium timescale at Europa, which may help explain the discrepancy between our observational constraints and the estimates of Carlson et al. (2002), Strazzulla et al. (2007), and Ding et al. (2013). Additionally, while radiolysis is responsible for the formation of H_2SO_4 on Europa, it can also destroy these molecules once formed. The balance of the production and destruction of hydrated H_2SO_4 on Europa is not well known, but is likely to be heavily particle and energy dependent. If H_2SO_4 is more readily destroyed within the complex irradiation environment on Europa's trailing hemisphere than in laboratory experiments with single-particle

bombardment, then these destructive processes may act to prolong the timescale over which sulfuric acid reaches a steady-state concentration on Europa. Additionally, it is possible that thermal processes which are unimportant at laboratory timescales may become important on Europa, and could serve to slow down the equilibrium timescale of the radiolytic sulfur cycle. Indeed, Tribbett et al. (2022) demonstrated that H_2O + H_2S + O_3 ice mixtures at Europa temperatures can undergo thermal oxidation reactions, even on laboratory timescales, which suggests that thermal reactions may affect both the steady-state composition and intermediary products of the radiolytic sulfur cycle.

Irradiation-Induced Reddening of Salts

We find that the dark, red material in the crater and proximal ejectas of both Pwyll and Manannán contain higher salt abundances than the surrounding bright ray ejecta. This dark material was likely excavated from Europa's subsurface during impact (Moore et al., 1998; Schenk et al., 2009), and is therefore expected to contain endogenic material which may have been further concentrated via preferential vaporization of ice during the impact process (Tomlinson et al., 2022). Indeed, Fanale et al. (2000) analyzed the NIMS observations shown in Figure 3.5 (f), (g), and (h) and found that the visually dark and red material in the crater floor and proximal ejecta have a spectral signature dominated by asymmetric absorption bands, which they broadly attributed to non-ice hydrated material. In the framework of our spectral modeling analysis, these asymmetric bands can be explained by a variety of hydrated salts but are not well reproduced by a simple combination of water-ice and hydrated sulfuric acid. Endogenic, presumably salty material within Europa's other geologically young features like the chaos terrains, bands, and ridges become progressively darker and redder toward the trailing hemisphere apex, potentially due to irradiation-induced reddening of salts. We expect that the endogenic salts within the Pwyll and Manannán craters and proximal ejecta have also been darkened and reddened via irradiation, based on their low-albedo and visually red coloration in the Galileo/SSI false-color images. If this is the case, the timescale for irradiation-induced reddening of salts on Europa's trailing hemisphere is apparently shorter than the ages of Pwyll and Manannán craters. Taking the lower end of the age estimates for Pwyll, as in Section 3.4, we can place an approximate upper limit of $\sim$1 Myr on the irradiation-induced reddening timescale of salts on Europa's trailing hemisphere.

3.5 Conclusions

We have performed a simple linear spectral modeling analysis on the available high-spatial-resolution Galileo/NIMS observations of Pwyll and Manannán craters in order to constrain the irradiation timescales of the radiolytic sulfur cycle and irradiation-induced reddening of salts operating on Europa's trailing hemisphere. Both Pwyll and Manannán craters and their ejecta are depleted in hydrated sulfuric acid relative to nearby older terrain. The radiolytic sulfur cycle has apparently not yet had enough time to build up an equilibrium concentration of H_2SO_4 at either crater, placing a strong lower limit of the age of these craters on its equilibrium timescale. Based on these NIMS observations and a rough estimate for the ages of Pwyll and Manannán, we estimate that the equilibrium timescale for the production of hydrated sulfuric acid on Europa's trailing hemisphere is likely to be at least a few million years. This is several orders of magnitude longer than previous estimates of $\sim 10^4$ yr based on laboratory experiments and suggests that simultaneous production and destruction of H_2SO_4 and perhaps thermal processes may be important for understanding the radiolytic sulfur cycle on Europa.

We also find that the dark and red material in the craters and proximal ejecta of Pwyll and Manannán contain an abundance of hydrated salts, presumably endogenic in origin. This salty material has apparently already been darkened and reddened via irradiation. We are therefore able to place an upper limit of the age of Pwyll crater, perhaps $\sim$1 Myr, on the timescale for irradiation-induced reddening of salts on Europa's trailing hemisphere.

Acknowledgments

The authors would like to thank Samantha K. Trumbo, William T. Denman, and Matthew Belyakov for helpful discussions.

Software: Cartopy (Met Office, 2022), GeoPandas (Jordahl et al., 2022), SciPy (Virtanen et al., 2020), Shapely (Gillies et al., 2023)

BIBLIOGRAPHY

Bierhaus, E. B. et al. (2001). "Pwyll Secondaries and Other Small Craters on Europa". *Icarus* 153.2, pp. 264–276.

Bierhaus, E. B., K. Zahnle, and C. R. Chapman (2009). "Europa's Crater Distributions and Surface Ages". *Europa*. Ed. by R. T. Pappalardo, W. B. McKinnon, and K. Khurana. University of Arizona Press, Tucson AZ, pp. 161–180.

Bland, M. T. et al. (2021). "Improving the Usability of Galileo and Voyager Images of Jupiter's Moon Europa". *Earth and Space Science* 8.12, e2021EA001935.

Brown, M. E. and K. P. Hand (2013). "Salts and Radiation Products on the Surface of Europa". *The Astronomical Journal* 145.4, p. 110.

Burnett, E. R. and P. O. Hayne (2021). "Europa's Hemispheric Color Dichotomy as a Constraint on Non-Synchronous Rotation". *Icarus* 364, p. 114438.

Carlson, R. W. et al. (2002). "Sulfuric Acid Production on Europa: The Radiolysis of Sulfur in Water Ice". *Icarus* 157.2, pp. 456–463.

Carlson, R. W. et al. (2005). "Distribution of Hydrate on Europa: Further Evidence for Sulfuric Acid Hydrate". *Icarus* 177.2, pp. 461–471.

Carlson, R. W. et al. (2009). "Europa's Surface Composition". *Europa*. Ed. by R. T. Pappalardo, W. B. McKinnon, and K. Khurana. University of Arizona Press, Tucson AZ, p. 283.

Carlson, R. W., R. E. Johnson, and M. S. Anderson (1999). "Sulfuric Acid on Europa and the Radiolytic Sulfur Cycle". *Science* 286.5437, pp. 97–99.

Carlson, R. W. (1998). *Galileo NIMS Spectral Image Cubes: Jupiter Operations*. Data set. NASA Planetary Data System.

Cassidy, T. A. et al. (2013). "Magnetospheric Ion Sputtering and Water Ice Grain Size at Europa". *Planetary and Space Science* 77, pp. 64–73.

Cooper, J. F. et al. (2001). "Energetic Ion and Electron Irradiation of the Icy Galilean Satellites". *Icarus* 149.1, pp. 133–159.

Dalton, J. B. et al. (2013). "Exogenic Controls on Sulfuric Acid Hydrate Production at the Surface of Europa". *Planetary and Space Science* 77, pp. 45–63.

Dalton, J. B. and K. M. Pitman (2012). "Low Temperature Optical Constants of Some Hydrated Sulfates Relevant to Planetary Surfaces". *Journal of Geophysical Research: Planets* 117.E9.

Dalton, J. B. et al. (2005). "Spectral Comparison of Heavily Hydrated Salts with Disrupted Terrains on Europa". *Icarus* 177.2, pp. 472–490.

Davis, M. R., M. E. Brown, and S. K. Trumbo (2023). "The Spatial Distribution of the Unidentified 2.07 μm Absorption Feature on Europa and Implications for Its Origin". *The Planetary Science Journal* 4.8, p. 148.

Ding, J. J. et al. (2013). "Implantation of Multiply Charged Sulfur Ions in Water Ice". *Icarus* 226.1, pp. 860–864.

Doggett, T. et al. (2009). "Geologic Stratigraphy and Evolution of Europa's Surface". *Europa*. Ed. by R. T. Pappalardo, W. B. McKinnon, and K. Khurana. University of Arizona Press, Tucson AZ, pp. 137–159.

Fanale, F. P. et al. (2000). "Tyre and Pwyll: Galileo Orbital Remote Sensing of Mineralogy versus Morphology at Two Selected Sites on Europa". *Journal of Geophysical Research: Planets* 105.E9, pp. 22647–22655.

Gillies, S. et al. (2023). *Shapely: Manipulation and Analysis of Geometric Objects*. Version v2.0.1. toblerity.org.

Hanley, J. et al. (2014). "Reflectance Spectra of Hydrated Chlorine Salts: The Effect of Temperature with Implications for Europa". *Journal of Geophysical Research: Planets* 119.11, pp. 2370–2377.

Hendrix, A. R. et al. (2011). "Europa's Disk-Resolved Ultraviolet Spectra: Relationships with Plasma Flux and Surface Terrains". *Icarus* 212.2, pp. 736–743.

Johnson, R. E. et al. (1988). "Analysis of Voyager Images of Europa: Plasma Bombardment". *Icarus* 75.3, pp. 423–436.

Jordahl, K., J. Van den Bossche, M. Fleischmann, et al. (2022). *geopandas*. Version v0.12.2.

King, O., L. N. Fletcher, and N. Ligier (2022). "Compositional Mapping of Europa Using MCMC Modeling of Near-IR VLT/SPHERE and Galileo/NIMS Observations". *The Planetary Science Journal* 3.3, p. 72.

Leonard, E. J., D. A. Patthoff, and D. A. Senske (2024). *Global Geologic Map of Europa*. Tech. rep. US Geological Survey.

Ligier, N. et al. (2016). "VLT/SINFONI Observations of Europa: New Insights into the Surface Composition". *The Astronomical Journal* 151.6, p. 163.

Loeffler, M. J. et al. (2011). "Radiolysis of Sulfuric Acid, Sulfuric Acid Monohydrate, and Sulfuric Acid Tetrahydrate and Its Relevance to Europa". *Icarus* 215.1, pp. 370–380.

Mastrapa, R. M. et al. (2008). "Optical Constants of Amorphous and Crystalline H2O-ice in the Near Infrared from 1.1 to 2.6 μm". *Icarus* 197.1, pp. 307–320.

McCord, T. B. et al. (2010). "Hydrated Minerals on Europa's Surface: An Improved Look from the Galileo NIMS Investigation". *Icarus* 209.2, pp. 639–650.

McCord, T. B. et al. (1999). "Hydrated Salt Minerals on Europa's Surface from the Galileo near-Infrared Mapping Spectrometer (NIMS) Investigation". *Journal of Geophysical Research: Planets* 104.E5, pp. 11827–11851.

McEwen, A. S. (1986). “Exogenic and Endogenic Albedo and Color Patterns on Europa”. *Journal of Geophysical Research: Solid Earth* 91.B8, pp. 8077–8097.

Met Office (2022). *Cartopy: A Cartographic Python Library with a Matplotlib Interface*. Version v0.21.1.

Moore, J. M. et al. (2001). “Impact Features on Europa: Results of the Galileo Europa Mission (GEM)”. *Icarus* 151.1, pp. 93–111.

Moore, J. M. et al. (1998). “Large Impact Features on Europa: Results of the Galileo Nominal Mission”. *Icarus* 135.1, pp. 127–145.

Moore, M. H., R. L. Hudson, and R. W. Carlson (2007). “The Radiolysis of SO2 and H2S in Water Ice: Implications for the Icy Jovian Satellites”. *Icarus* 189.2, pp. 409–423.

Nelson, M. L. et al. (1986). “Europa: Characterization and Interpretation of Global Spectral Surface Units”. *Icarus* 65.1, pp. 129–151.

Paranicas, C., R. W. Carlson, and R. E. Johnson (2001). “Electron Bombardment of Europa”. *Geophysical Research Letters* 28.4, pp. 673–676.

Paranicas, C. et al. (2009). “Europa’s Radiation Environment and Its Effects on the Surface”. *Europa*. Ed. by R. T. Pappalardo, W. B. McKinnon, and K. Khurana. University of Arizona Press, Tucson AZ, p. 529.

Pospieszalska, M. K. and R. E. Johnson (1989). “Magnetospheric Ion Bombardment Profiles of Satellites: Europa and Dione”. *Icarus* 78.1, pp. 1–13.

Press, W. H. et al. (1992). *Numerical Recipes in FORTRAN 77: The Art of Scientific Computing*. 2nd ed. Cambridge University Press.

Schenk, P. M. and E. P. Turtle (2009). “Europa’s Impact Craters: Probes of the Icy Shell”. *Europa*. Ed. by R. T. Pappalardo, W. B. McKinnon, and K. Khurana. University of Arizona Press, Tucson AZ, pp. 181–198.

Shkuratov, Y. et al. (1999). “A Model of Spectral Albedo of Particulate Surfaces: Implications for Optical Properties of the Moon”. *Icarus* 137.2, pp. 235–246.

Strazzulla, G. (2011). “Cosmic Ion Bombardment of the Icy Moons of Jupiter”. *Nuclear Instruments and Methods in Physics Research Section B: Beam Interactions with Materials and Atoms* 269.9, pp. 842–851.

Strazzulla, G. et al. (2007). “Hydrate Sulfuric Acid after Sulfur Implantation in Water Ice”. *Icarus* 192.2, pp. 623–628.

Tomlinson, T. C. and P. O. Hayne (2022). “Composition and Possible Origins of Dark Crater Ejecta on Europa”. *Icarus* 385, p. 115037.

Tribbett, P. D. and M. J. Loeffler (2022). “Thermal Reactions between H2S and O3: Implications for Europa Surface Chemistry”. *The Planetary Science Journal* 3.10, p. 233.

Trumbo, S. K. et al. (2022). “A New UV Spectral Feature on Europa: Confirmation of NaCl in Leading-Hemisphere Chaos Terrain”. *The Planetary Science Journal* 3.2, p. 27.

Trumbo, S. K., M. E. Brown, and K. P. Hand (2019). “Sodium Chloride on the Surface of Europa”. *Science Advances* 5.6, eaaw7123.

– (2020). “Endogenic and Exogenic Contributions to Visible-Wavelength Spectra of Europa’s Trailing Hemisphere”. *The Astronomical Journal* 160.6, p. 282.

Virtanen, P., R. Gommers, T. E. Oliphant, et al. (2020). “SciPy 1.0: Fundamental Algorithms for Scientific Computing in Python”. *Nature Methods* 17, pp. 261–272.

Zahnle, K. et al. (2003). “Cratering Rates in the Outer Solar System”. *Icarus* 163.2, pp. 263–289.

Chapter 4

SPECTROSCOPIC MAPPING OF CALLISTO WITH HST/STIS AND IMPLICATIONS FOR ITS SURFACE COMPOSITION

Davis, M. R., S. K. Trumbo, M. E. Brown, and M. Belyakov (2025). "Spectroscopic Mapping of Callisto with HST/STIS and Implications for Its Surface Composition". *The Planetary Science Journal* 6.7, p. 161.

Abstract

We present global, spatially resolved ultraviolet-visible spectra of Callisto obtained with HST/STIS and explore possible compositions of Callisto's surface material. We map the strength of a widespread downturn toward the near-UV and the NIR spectral slope from 700 to 1000 nm, which varies from slightly blue (reflectance decreasing from 700 to 1000 nm) to red (reflectance increasing) across Callisto's surface. Globally, bright water-ice-rich regions tend to have neutral or blue NIR slopes and a shallower near-UV downturn, while darker material is associated with red NIR slopes and stronger near-UV absorption. Broad absorptions near 820 and 930 nm are spatially correlated with the Asgard and Valhalla impact basins and may be associated with iron-bearing silicates. An absorption edge near 275 nm maps primarily to Callisto's trailing hemisphere, and a 320 nm absorption most prevalent within and surrounding Asgard and Valhalla may be related to organics. We report two new absorption features near 230 and 450 nm which might be attributed to irradiated NaCl. We find little evidence for sulfur-bearing species at UV-visible wavelengths and suggest that a 280 nm band seen only in leading/trailing hemisphere ratio spectra and previously attributed to SO_2 is better explained as a consequence of dividing the unrelated 320 nm leading hemisphere band by the trailing-hemisphere 275 nm absorption edge. Spatial variations in spectral features suggest that Callisto's dark material composition varies regionally, reflecting a mix of endogenic and exogenic sources and radiolytic alteration.

4.1 Introduction

Callisto, the outermost of Jupiter's Galilean moons, has an ancient (~4–4.5 Ga) surface dominated by impact craters and no evidence for any past endogenic processing, volcanism, tectonics, or other surface-interior interactions which are widespread on Io, Europa, and Ganymede (Bottke et al., 2024; Greeley et al., 2000; Moore et al., 2004). Callisto has the lowest albedo and the highest proportion of dark material among the four Galilean moons (Moore et al., 2004). Its surface is also the most degraded, and sublimation-driven landform modification and mass-wasting effects result in a well-segregated surface. Bright high-albedo regions consist of relatively pure frost emplaced on topographic highs, formed when exposed H_2O ice sublimates under daytime heating (~165 K) and re-deposits on crater rims and peaks (Howard et al., 2008; Moore et al., 1999). A smooth blanket of fine-grained dark (non-icy) material fills topographic lows like crater floors and inter-crater depressions (Moore et al., 2004). This dark material may be largely composed of lag deposits left behind after the H_2O (and possibly CO_2) ice sublimates out of endogenic ice/rock mixtures which were excavated from the subsurface by large impactors (e.g. Howard et al., 2008; Moore et al., 1999, 2004; White et al., 2016), or it may be dominated by dust delivered from the irregular satellites via Poynting–Robertson drag (Bottke et al., 2013; Chen et al., 2024). Most likely, Callisto's dark material represents a mix of endogenic lag deposits and delivered dust, but their relative contributions remain uncertain. In addition to this dark material, Callisto's surface is composed primarily of water ice, small amounts of CO_2, and possibly sulfur-bearing species (Cartwright et al., 2020, 2024; Hibbitts et al., 2002; Moore et al., 2004; Noll et al., 1997).

Despite nearly 50 years of spectroscopic study, the specific mineralogical composition of Callisto's dark material remains largely unknown. Several lines of evidence, including absorption features detected with Galileo/NIMS (0.7–5.2 μm, R~40–200), ground-based observations, and recent JWST/NIRSpec (G395H; 2.85–5.35 μm, R~2700) data have been interpreted as arising from iron- and Mg-OH bearing silicates, carbon bearing species, and organic molecules, perhaps suggesting a composition similar to primitive asteroids and carbonaceous chondrites (Calvin et al., 1991, 1993; Cartwright et al., 2024; McCord et al., 1997, 1998). However, the identities of many non-water ice absorptions between 1 and 5 μm remain uncertain, and the literature is often contradictory, with various types of material suggested to explain each feature. Some authors suggest that several of these NIR bands are consistent with carbonates and C-H and C-N stretch features from organics (Cartwright et al., 2024; Johnson, 2004; McCord et al., 1998), while others claim they are more

consistent with sulfur-bearing species (Cartwright et al., 2020; McCord et al., 1997), and still others suggest that at least some of these features may be associated with ammonia or NH_4-bearing minerals (Calvin et al., 1993) or Na-bearing species like Na-carbonates (Johnson et al., 2004), Na-oxides (e.g. $Na_2C_2O_4$), or Na-sulfates (e.g. Na_2SO_4) (Cartwright et al., 2020, 2024), all of which have different implications for Callisto's formation and history.

Existing observations of Callisto at UV and visible wavelengths have led to a number of valuable insights, despite the somewhat sparse availability of data. Callisto displays a significant hemispheric albedo dichotomy, where its trailing hemisphere (270°W) is brighter than its leading hemisphere (90°W), which is opposite of the pattern seen on Europa and Ganymede (Hendrix et al., 2005; Nelson et al., 1987). This dichotomy may result directly from the preferential delivery of dark material from Jupiter's prograde irregular satellites to the leading hemisphere (Bottke et al., 2013; Chen et al., 2024), or from weathering processes thought to alter Callisto's surface including micrometeoroid gardening and radiolytic alteration from magnetospheric charged particle bombardment (Bottke et al., 2013; Buratti, 1991; Johnson et al., 2004). A strong opposition effect on the leading hemisphere, where it becomes nearly equally as bright as the trailing side when viewed at 0° solar phase angle, may arise from smaller grain sizes resulting from the higher total bombardment of irregular satellite dust onto the leading hemisphere (Buratti, 1991; Calvin et al., 1993).

A UV absorption feature near 280 nm, seen in the spectral ratio of Callisto's leading to trailing hemisphere, has been attributed to SO_2 possibly related to neutral sulfur from Io delivered to the leading/sub-Jovian hemisphere or due to enhancement of endogenic or delivered sulfur by micrometeoroid bombardment (Lane et al., 1997; Noll et al., 1997). The presence of SO_2 on Callisto was initially supported by near-IR absorptions at 3.88 and 4.02 μm seen in some Galileo/NIMS observations and suggested to arise from an S-H stretch (McCord et al., 1997) and SO_2 (Hibbitts et al., 2000), respectively. However, more recent analyses have questioned the identification of all three of these absorptions (Cartwright et al., 2020; Hendrix et al., 2008; Johnson, 2004). Whether or not SO_2 or endogenically sourced sulfur-bearing species are present on Callisto remains an open question, although some amount of Iogenic sulfur is likely delivered by the Jovian magnetosphere (Cooper et al., 2001; Liuzzo et al., 2019).

Generally, Callisto's UV slope tends to redden at lower latitudes, which Hendrix

et al. (1999) suggest may be due to the presence of H_2O_2. However, Callisto lacks the 3.5-μm H_2O_2 absorption seen on Europa and Ganymede (Carlson et al., 1999a; Hand et al., 2013; Trumbo et al., 2023, 2019a; Wu et al., 2024), calling this identification into question. Analysis of Galileo/UVS data (~160–320 nm, R~150–230) revealed the presence of a possible absorption feature at high southern latitudes with a band center somewhere long-wards of 320 nm (where the UVS data ended) which has been attributed to organic species (Hendrix et al., 2008). Hendrix et al. (2008) hypothesize that this species is progressively weathered at lower latitudes by charged particle or UV irradiation, producing carbonized organics which absorb strongly in the far-UV and potentially explaining both the observed variation in the UV spectral slope and the apparent 280 nm absorption seen in leading/trailing ratio spectra. In this case, much of Callisto's UV spectral behavior is explained by organic species which have undergone varying amounts of radiolytic alteration rather than the previously suggested H_2O_2 and SO_2, perhaps suggesting a largely carbon dominated surface chemistry.

While existing data sets remain consistent with the presence of hydrated silicate minerals, carbon-bearing species, CH- or CN-bearing organics, and S-bearing species within Callisto's dark material, they have proven insufficient for definitive identification and evidence for S-bearing species has become increasingly sparse. Previous analyses at UV and visible wavelengths have relied on full-disk UV-visible spectroscopy, which lack spatial detail (e.g. Hendrix et al., 2005; McFadden et al., 1980; Nelson et al., 1987); spatially resolved UV spectra with limited spatial and wavelength coverage (~160–320 nm) (Hendrix et al., 2008); or high-spatial-resolution imagery, which lacks spectral detail (Denk et al., 1999; Greeley et al., 2000). To help expand our understanding of the spectral properties of Callisto's surface, we used the Space Telescope Imaging Spectrograph aboard the Hubble Space Telescope (HST/STIS; ~200–1000 nm, R~600–1000) to obtain the first near-global, spatially resolved UV-visible wavelength reflectance spectra of Callisto. We use this new data set to identify and map absorption features across Callisto's surface and discuss compositional implications in the context of potential endogenic materials, delivery of exogenic species, and alteration via charged particle bombardment.

4.2 Observations and Data Reduction

We present global, spatially resolved ultraviolet and visible wavelength spectroscopy of Callisto's surface taken with HST/STIS. The data were acquired in the first-order spectroscopy mode with the G230L (157–318 nm), G430L (290–570 nm) and

Table 4.1: HST/STIS Observation Details

Date (UT)	Time (Start–End)	Central Lon.	Central Lat.	Angular Diameter	Gratings Used	Slit Width	Exposure Time (s)
2020-08-22	04:47–05:20	47°W	−1.08°	1.53″	G230L	0.2″	155.0
2020-08-26	05:43–06:16	135°W	−1.09°	1.52″	G230L	0.2″	155.0
2020-10-19	17:17–17:51	229°W	−1.01°	1.29″	G230L	0.2″	155.0
2020-09-20	09:31–10:04	318°W	−1.07°	1.41″	G230L	0.2″	155.0
2020-09-07	13:20–13:53	41°W	−1.08°	1.46″	G430L	0.1″	42.0
2020-10-10	00:00–23:59	41°W	−1.03°	1.32″	G750L	0.1″	75.0
2020-10-15	08:26–08:55	135°W	−1.02°	1.31″	G430L	0.1″	42.0
2020-10-15	09:52–10:30	136°W	−1.02°	1.31″	G750L	0.1″	70.0
2021-05-26	05:42–06:12	221°W	0.65°	1.37″	G430L	0.1″	42.0
2020-10-19	09:13–09:51	221°W	−1.01°	1.29″	G750L	0.1″	70.0
2020-05-10	03:15–03:45	314°W	−1.1°	1.41″	G430L	0.1″	42.0
2020-05-10	04:39–05:18	315°W	−1.1°	1.41″	G750L	0.1″	75.0

G750L (524–1027 nm) gratings across 10 visits between May 2020 and May 2021. UV observations with the G230L grating were taken with a slit width of 0.2″ and used the STIS MAMA detector, while the two visible gratings (G430L and G750L) used a 0.1″ slit and the STIS CCD.

The observations are summarized in Table 4.1. We downloaded flux- and wavelength-calibrated x2d files from the MAST Archive produced by the standard HST STIS calibration pipeline (calstis). Data taken with the G750L grating showed substantial fringes at the longest wavelengths, so we reprocessed the data using the calstis pipeline with the additional defringing routines turned on. We then extracted individual spectra from the x2d images, with a pixel scale of 0.025″ and 0.05″ for the UV and visible gratings, respectively. This corresponds to a spatial resolution of ∼80 and ∼160 km near the center of the disk on Callisto, which is comparable to the diffraction-limited spatial resolution of HST near 250 nm (80 km) and 600 nm (192 km), respectively. To convert each spectrum to units of reflectance, we divided by a solar spectrum which was smoothed and binned to match the spectral resolution and sampling of the observations. For the G230L grating, we used solar spectra from the Total and Spectral Solar Irradiance Sensor (TSIS-1) Spectral Irradiance Monitor (SIM) on the International Space Station acquired on the same date as each observation and downloaded via the LASP Interactive Solar Irradiance Datacen-

ter (LISIRD).[1] For the two visible wavelength gratings, we used the ASTM E490 zero-airmass solar reference spectrum.[2]

The reprocessed G750L spectra exhibited multiple artifacts as a result of the defringing process as well as an artificial dropping of the reflectance towards longer wavelengths as a result of slit losses due to the broadening of the point-spread function with increasing wavelength, as was also noted in STIS observations of Mars, Europa, and Io (Bell III et al., 2007; Trumbo et al., 2020, 2022b). We simultaneously correct for these wavelength-dependent slit losses and defringing artifacts following the method described in Trumbo et al. (2022b). We fit a spline curve to the ground-based leading-hemisphere spectrum of Callisto from Spencer et al. (1995), combined with the lower spectral resolution data from Clark et al. (1980) to fill in missing wavelengths above ~780 nm. We then construct a disk-integrated spectrum of Callisto's leading hemisphere, centered at 70°W to match the viewing geometry of Spencer et al. (1995). We multiply each individual HST spectrum by the ratio of the spline fit to the ground-based data and the constructed full-disk HST spectrum. This allows for the correction of the slit losses and defringing artifacts while preserving pixel-to-pixel variations and the general spectral shape within the data.

We calculated the geographic coordinates of each extracted pixel on Callisto using the phase, angular size, and pole orientation at the time of the observation obtained from JPL Horizons. We found that the telemetry information contained in the FITS headers was not sufficiently accurate to determine the geographic locations of each pixel, particularly for the observation taken on 2021-05-26, where the HST target acquisition appears to have partially failed. We therefore reconstructed a 3D image from each of the individual slit observations for a given grating and viewing geometry, summed across the wavelength axis to create a 2D average image, and fit a 2D Gaussian to the reconstructed image to identify the center of the disk. We used this disk center and the slit-offset information contained in each fits header to calculate the corresponding latitude and longitude of each spatial pixel. We then combined the two visible gratings (G430L and G750L) to create a full visible wavelength spectrum (300–1000 nm) for each spatial pixel. For the 45°W, 135°W, and 315°W viewing angles, the two visible gratings were taken close enough in time and with the same slit orientation and step pattern that the resulting pixel locations on Callisto were very similar and we simply matched up pixels which overlapped

[1] `https://lasp.colorado.edu/lisird/`

[2] `https://www.nrel.gov/grid/solar-resource/spectra-astm-e490.html`

in area by more than ~90%. For the two gratings at ~225°W viewing geometry, however, the observations were taken nearly 7 months apart and combining the full visible wavelength region required more care. We interpolated the spatial pixels in the G750L grating to match those of the G430L grating by computing the average of the spectra of G750L pixels which overlap a given G430L pixel, weighted by the area of the overlapping region. For all viewing angles, we computed an additional offset, which was applied to the G750L spectra so that the median values of the spectra at the overlapping wavelengths from the two gratings are equal. This ensured that there were no jumps or discontinuous regions in the combined visible wavelength reflectance spectra. We generally consider the UV and visible spectra separately, at their native resolutions, except when otherwise noted. In this case, we degrade the spatial resolution of the visible data to match that of the UV observations by resampling the visible data at the locations of the UV spatial pixels. We do not apply a specific photometric correction because we analyze normalized spectra. However, pixels whose center coordinates were farther than 60° from the disk center were removed in order to minimize photometric effects associated with high incidence angles where deviations from ideal photometric behavior may become significant, except for the case where there were no other data associated with that spatial region.

4.3 Definition of Spectral Features

Figure 4.1 shows a selection of representative spectra on Callisto's surface. Immediately obvious in all of the spectra is a sharp decrease in reflectance from the visible to near-UV wavelengths, consistent with previous ground-based disk-averaged observations (e.g. Clark et al., 1980; Johnson et al., 1970). Indeed, all of the Galilean satellites have a spectrum with a band edge near 500 nm, interpreted as the edge of a broad and strong UV absorption (e.g. Calvin et al., 1995; McFadden et al., 1980). This near-UV downturn appears to be present globally on Callisto, although its strength varies across the surface, and the wavelength at which the downturn starts shifts from ~500 to 650 nm. All of the Callisto spectra have red slopes in the near-UV (200–350 nm), consistent with Hendrix et al. (2008), and a steep red slope from ~350–500 nm with an apparent slope break near 415 nm. Most of the spectra have a neutral or moderately red NIR slope from 700 to 1000 nm, although some pixels have a slightly blue slope beyond 700 nm.

As is shown in Figure 4.1 (c–h), there are a number of discrete absorption features seen in the Callisto spectra. There are two broad and shallow absorptions centered at 820 and 930 nm which combine to form a broader band from ~700 to 990 nm

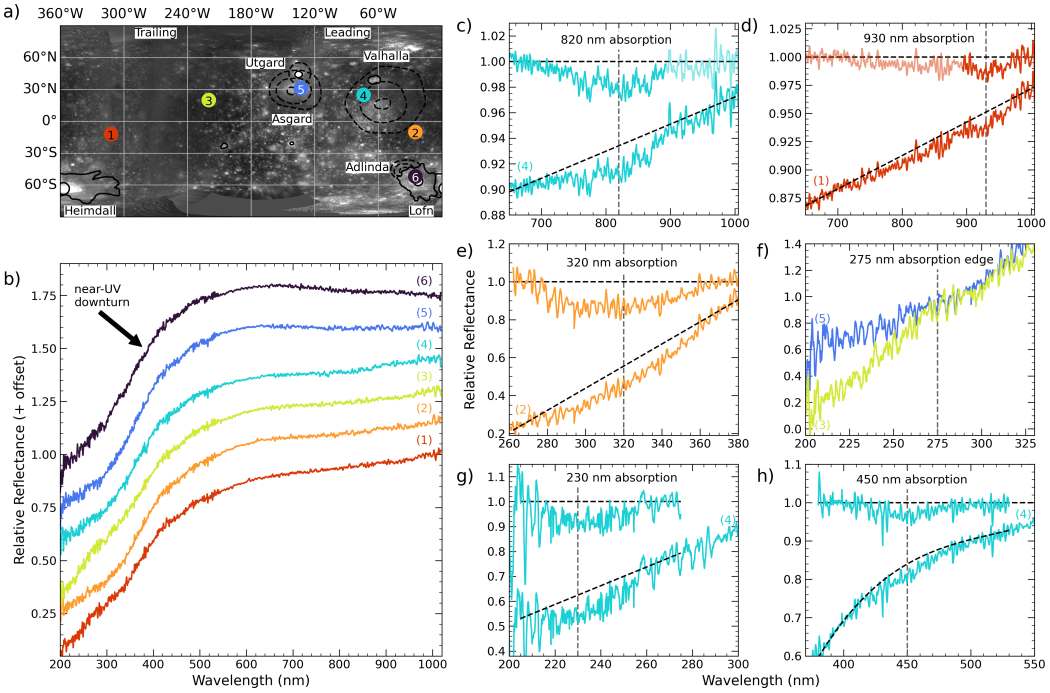

Figure 4.1: Example HST spectra from 200 to 1000 nm of a few representative regions on Callisto. The location of each spectrum is indicated by a numbered circle on the map (a) with a corresponding color to the plotted spectrum (b). Each spectrum is calculated by averaging the UV and visible pixels which intersect a circle with a radius of 2° about the point of interest, and combining the resulting UV and visible spectra. Spectra are normalized to unity at 1000 nm and offset by increments of 0.15 for clarity. These spectra are generally smoothly varying, and uncertainties can be estimated from the scatter in the data. (c-h) show many of the individual spectral features discussed in this paper, with band centers indicated by the vertical dashed gray lines. Colors indicate the corresponding spectrum from panel b used to highlight each individual spectral feature. Polynomial continuum fits are shown with black dashed lines and continuum divided features are included above each spectrum. In panel (f), the Asgard spectrum (5, blue) is included to highlight the difference between a typical Callisto spectrum that does not have a 275 nm absorption edge and one that does (3, yellow). The large ringed basins Valhalla, Asgard, Utgard, and Adlinda are outlined with black dashed lines and labeled on the map in panel (a) along with the bright young impact craters Heimdall and Lofn and their ejecta. The basemap is the high-resolution USGS global mosaic created from Voyager and Galileo images (USGS Astrogeology Science Center, 2013).

in many pixels. This combined band is consistent with the weak ~750 to 950 nm absorption reported in the ground-based spectrum of Clark (1980). Some of the Callisto spectra also display an absorption from 275–360 nm, with a band center near 320 nm. Figure 4.1 (e) shows an example spectrum with a clear 320 nm absorption. It is possible that this feature is the same as the $\gtrapprox$320 nm absorption inferred by

Hendrix et al. (2008); see Section 4.4 for more detailed discussion. Some regions on Callisto's trailing hemisphere show a steep absorption edge starting at ~275 nm and quickly dropping towards shorter wavelengths (see spectra 1 and 3 in Figure 4.1 (b) and the zoom-in in panel (f)). Additionally, many of the Callisto spectra also show two previously unreported absorption features centered near 230 nm and 450 nm, as seen in Figure 4.1 (g) and (h). These features are superimposed on the much stronger 275 nm absorption edge and near-UV downturn, respectively.

Noll et al. (1997) noted that the spectral ratio of Callisto's leading to trailing hemisphere produces a broad absorption feature centered near 280 nm, which we are able to reproduce with our data set. However, the width of the ratio feature is wider than that assumed by Noll et al. (1997), whose data only extended to 330 nm (see Section 4.5 for a more detailed discussion of the spectra), and we see no unambiguous evidence of a UV absorption feature centered at 280 nm in the spectra of any of the individual spatial pixels without performing such a ratio.

In the following sections, we explore the spatial distributions of the near-UV downturn, NIR (700 - 1000 nm) slope, 930 nm, 820 nm, 450 nm, 320 nm and 230 nm absorption features, 280 nm ratio feature, and the 275 nm absorption edge and compare the spectra with existing libraries of laboratory spectra to explore possible compositions of Callisto's non-ice material. We then consider the spatial distributions and plausible identifications of the various bands and propose a consistent conceptual model for the composition of Callisto's dark material with contributions of endogenic, exogenic, and radiolytically processed species. Finally, we compare the average leading and trailing hemisphere spectra of Callisto with equivalent HST/STIS spectra of the other Galilean satellites - Io, Europa and Ganymede and discuss implications for the Galilean system.

4.4 Spectral Maps

We map the strength of Callisto's absorption features with one of two methods. For the near-UV downturn, where the full width of the absorption extends beyond the observed wavelength range, as well as the NIR (700–1000 nm) slope, we measure the strength of the feature by fitting a line to the data after normalizing at the long wavelength edge, excluding wavelengths that may be strongly affected by other overlapping features. We estimate 1σ uncertainties on the measured slope values for each spatial pixel using the residual variance of the linear polynomial fit and the scatter in the spectral values, using standard linear regression error propagation

(Bevington et al., 2003). For the near-UV downturn, we measure the slope between 360 to 410 nm in order to avoid interference from the 320 nm and 450 nm features and normalize at 410 nm. We normalize at 1000 nm and measure the slope between 680 and 1000 nm (excluding 700–930 nm where the 820 and 930 nm bands are) for the NIR slope, although the effect of the weak 820 and 930 nm bands is minimal and slopes computed across the entire 700 to 1000 nm range produce qualitatively similar maps. The results are mapped in Figure 4.2 and Figure 4.3, respectively. We find that small changes to the wavelength bounds used in the linear fits produce consistent results for these mapped slopes.

For the 280 nm ratio, 320 nm, and combined 820 and 930 nm features, we map the band strengths using the integrated band area. We fit a linear continuum to the regions surrounding the absorption and produce a continuum divided spectrum. We then integrate the residual absorption across the full feature to calculate a band area or equivalent width and estimate the 1σ uncertainty for each spatial pixel by taking the standard deviation of the normalized spectrum within the feature as a constant 1σ uncertainty and computing the trapezoidal error propagation for the band area integration as described in Bevington et al. (2003). For the overlapping 820 and 930 nm bands, we calculate a single combined band strength by fitting a linear continuum from 660 to 995 nm (excluding 695–975 nm) and integrating across the combined band width from 710 to 980 nm. For the 320 nm feature, we fit the continuum from 262 to 370 nm (excluding 275–360 nm) and integrate across the band from 275 to 360 nm. For the 280 nm ratio feature, we first construct an average spectrum within 5° of the trailing hemisphere apex (270°W, 0°N) and divide each Callisto spectrum by this trailing hemisphere average before fitting a linear continuum from 230 to 405 nm (excluding 235–400 nm) and integrating the residual feature from 235 to 400 nm. These calculated band areas are mapped in Figures 4.5, 4.6, and 4.8.

Finally, for the 275 nm absorption edge, it is difficult to determine a consistent UV spectral continuum for each pixel because the feature extends beyond the observed wavelength range, there is increased noise at the short-wavelength end of the spectra, and additional overlapping absorption features apparently modify Callisto's UV spectrum (e.g. the 230 nm feature). We therefore apply both approaches for measuring the band strength and compare the resulting maps. We measure the slope between 230 and 270 nm after normalizing at 270 nm, with the results shown in Figure 4.7 (a). To measure the band area, we first construct a base spectrum from

Callisto spectra interpreted to contain little or no sign of the 275 nm absorption edge by averaging five pixels with the smallest (nearly neutral) 230 to 270 nm slopes. The five pixels used in this mean are nearby one another and centered at (141°W, 42°N), (154°W, 39°N), (150°W, 45°N), (145°W, 51°N), and (144°W, 49°N). We then divide each Callisto spectrum, normalized to unity at 280 nm, by this base spectrum and integrate the residual feature from 220 to 275 nm. We exclude wavelengths shorter than 220 nm because of to the significantly increased noise at the short-wavelength end of the spectra, as well as the presence of a possible absorption shoulder shortwards of ~220 nm in some of the pixels. The results are mapped in Figure 4.7 (b).

In the following subsections, we map the strength of each spectral feature and discuss their spatial distributions. We report the minimum and maximum estimated uncertainties across all of the spatial pixels as error bars on each figure's corresponding colorbar and caption.

Near-UV Downturn

Figure 4.2 (a) shows the bolometric albedo from Camarca et al. (2023) for comparison with the strength of the near-UV downturn mapped in Figure 4.2 (b). Generally, the leading hemisphere has a stronger near-UV absorption than the trailing hemisphere, especially at northern latitudes. The leading hemisphere southern low latitudes, where there is an abundance of bright material, show a relatively weak near-UV downturn. The southern low latitudes on the leading/anti-Jovian hemisphere is also where Cartwright et al. (2024) find the strongest 4.57 μm band strengths, which is tentatively attributed to CN-bearing organics. The trailing hemisphere mid-latitudes show a stronger near-UV downturn than the high-latitudes, which have a similar strength as the leading hemisphere low southern latitudes. However, as seen in Figure 4.2 (a), the trailing hemisphere high-latitudes do not have an abundance of brighter material like the leading hemisphere low southern latitudes. The bright young impact features Heimdall (357°W, 65.5°S) and Lofn (22°W, 56.5°S) and their ejecta show the shallowest measured downturn, while the low albedo region to the east of Valhalla have the strongest measured near-UV downturn.

Figure 4.2 (c) shows a scatter plot of the bolometric albedo versus our proxy for the strength of the near-UV downturn for the leading and trailing hemispheres with the colorbar indicating the NIR (700 to 1000 nm) slope mapped in Figure 4.3. The bolometric albedo of each HST spatial pixel is determined by calculating the average

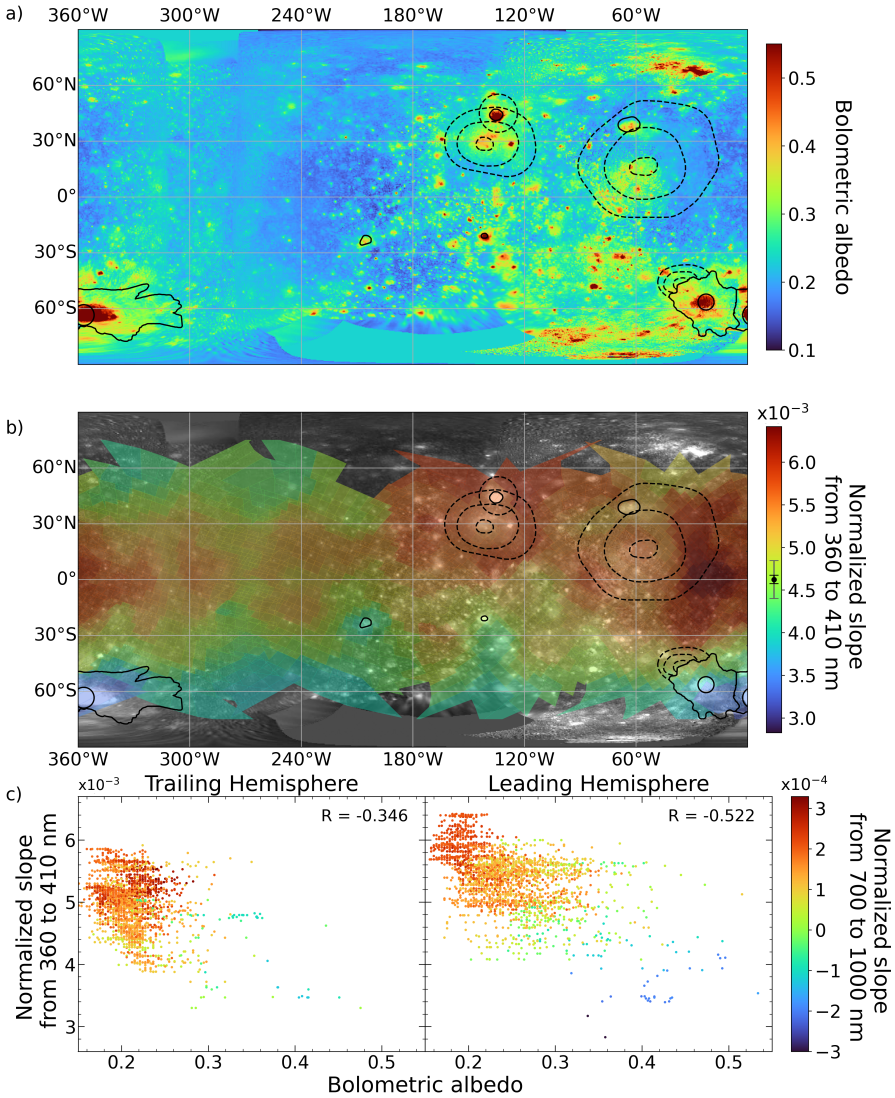

Figure 4.2: Maps showing Callisto's bolometric albedo (a; from Camarca et al., 2023) compared with the spectral slope from 360 to 410 nm (b), which measures the strength of the near-UV downturn (redder slope = stronger downturn). The per-pixel estimated 1σ error on the 360 to 410 nm slope ranged from $\pm 4.9\times10^{-5}$ to $\pm 2.2\times10^{-4}$, and the minimum (black) and maximum (gray) estimated error is shown on the colorbar. On both maps, the large ringed basins Valhalla (56°W, 16°N), Asgard (140°W, 32°N), Utgard (134°W, 45°N), and Adlinda (36°W, 48°S) are outlined with black dashed lines. For Valhalla, Asgard, and Adlinda, the central, inner, and outer rings are shown, based on the geologic map from Greeley et al. (2000). A few young, bright impact features are also indicated in solid black, along with Heimdall (357°W, 65.5°S) and Lofn (22°W, 56.5°S) craters and their relatively extensive ejecta. The scatter plots (c), produced by degrading the spatial resolution of the albedo map to match the HST/STIS observations, reveal the moderate correlation between the bolometric albedo and near-UV downturn on Callisto's leading and trailing hemispheres and the Pearson correlation coefficient (R) is shown on each plot. The colorbar indicates the NIR slope (700-1000 nm) mapped in Figure 4.3.

albedo of overlapping pixels from the higher spatial resolution map of Camarca et al. (2023), thereby degrading the resolution to match that of the HST observations. Generally, pixels with the shallowest near-UV downturns tend to have higher albedos and regions with the strongest downturns have low albedos, explaining the moderate negative correlation. However, relative differences in the albedo of the dark material do not correlate strongly with the strength of the near-UV downturn, aside from having a generally steeper slope than high albedo pixels. Additionally, while the bright young impact features Heimdall and Lofn tend to have a much shallower near-UV downturn compared with the Valhalla (56°W, 16°N) and Asgard (140°W, 32°N) impact basins, the strength of the near-UV absorption within these geologic features is not noticeably different from surrounding pixels with similar albedos, suggesting that the spatial distribution of the material(s) responsible for the near-UV downturn is not closely tied to Callisto's geologic units.

700–1000 nm Slope

The NIR (700 - 1000 nm) slope is mapped in Figure 4.3 (a). We find that much of Callisto's surface has a red 700 to 1000 nm slope, although some regions are neutral or blue. While previous analyses using Galileo/SSI imaging did not find any regions with blue NIR slopes (e.g. Denk et al., 1999), we believe this is due to the locations of the SSI filters, which miss the downward slope starting ~650 nm. Indeed, we integrated the HST spectra against the SSI green (~550 nm) and IR986 (~986 nm) bandpasses, computed the green - IR slope, and found only neutral and red slopes. Figure 4.3 (b) shows the moderate negative correlation between the NIR slope and bolometric albedo. Generally, the reddest material with the largest NIR slopes is dark (albedo $\lesssim 0.35$), although not all dark material is particularly NIR red. On the leading hemisphere, the darkest material, which is concentrated to the east and south of Valhalla, has the reddest NIR slopes as well as the strongest near-UV downturn, although the most extreme values appear to be slightly offset from one another. The generally redder slopes seen on the leading hemisphere are consistent with ground based photometry and have been suggested to be related to the higher fraction of irregular satellite dust expected to be delivered (Bottke et al., 2013; Chen et al., 2024; Morrison et al., 1974). On the trailing hemisphere, the lowest albedo pixels are not necessarily the reddest, suggesting that whatever species are responsible for the red NIR slopes must not be the only material contributing to the low albedo. The moderate correlation between the NIR red and UV red material seen on the leading hemisphere is also less apparent on the trailing hemisphere.

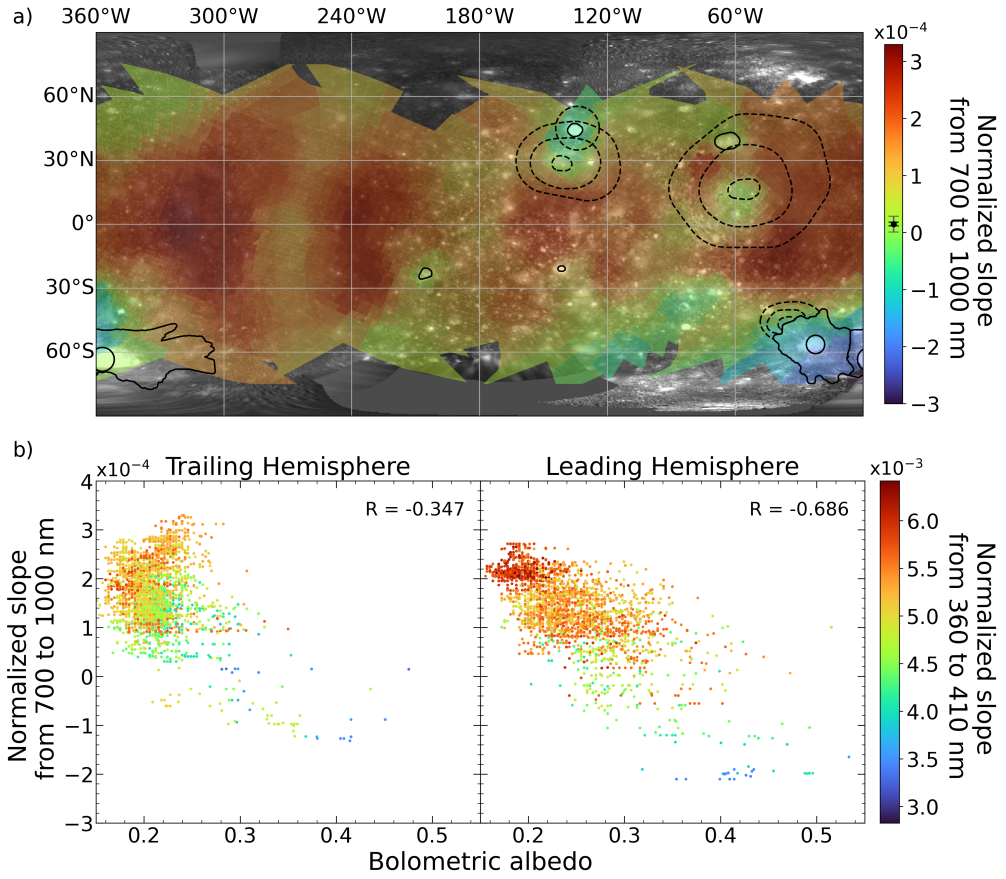

Figure 4.3: (a) The map of the strength of the 320 nm absorption demonstrates that it is largely constrained to the regions within and surrounding the Asgard and Valhalla impact basins which leads to clear hemispheric asymmetry. The scatter plots (b) reveal a moderately strong negative correlation with albedo, with the pixels displaying a significant 320 nm absorption tending to be both dark and NIR red. The strongest measured 320 nm band areas are associated with dark and red material directly east of Valhalla, which is partially within the outer ring or trough zone. The estimated 1σ error for the calculated band area of each spatial pixel ranges from ±0.1 to ±0.27 nm, and the minimum (black) and maximum (gray) estimated error is shown on the colorbar in panel (a).

On both hemispheres, pixels dominated by bright water-ice-rich material have blue or neutral slopes, consistent with the bluer visual color of Callisto's high-albedo material. The young impact craters, Heimdall (357°W, 65.5°S) and Lofn (22°W, 56.5°S), and their relatively extensive bright ice-rich ejecta contain pixels with the bluest measured NIR slopes.

The smooth bright central zones of the Utgard, Asgard and Valhalla impact basins, which have comparable near-UV downturns as the rest of the basin material, have neutral or slightly blue NIR slopes while the inner ridge and trough zones (as defined

in Greeley et al. (2000)) and surrounding regions are red in the NIR. As discussed in Greeley et al. (2000), after careful analysis of Galileo SSI imagery it remains uncertain whether this bright NIR neutral material is directly associated with the central plains of the ringed impact basins, or if bright material excavated from the sub-surface by recent impacts which happen to have hit near the centers of all three impact basins excavated ice-rich material that covered the otherwise NIR red surface of the large ringed structures. Based on our mapping results, however, we suggest that a direct association with the smooth central zones of the impact basins is the more likely explanation, as nearby bright impacts in the southern portion of the inner and outer ring of Valhalla, and near the eastern edge of the inner ring at Asgard do not have NIR slopes which differ significantly from the surrounding material.

820 and 930 nm Absorption Features

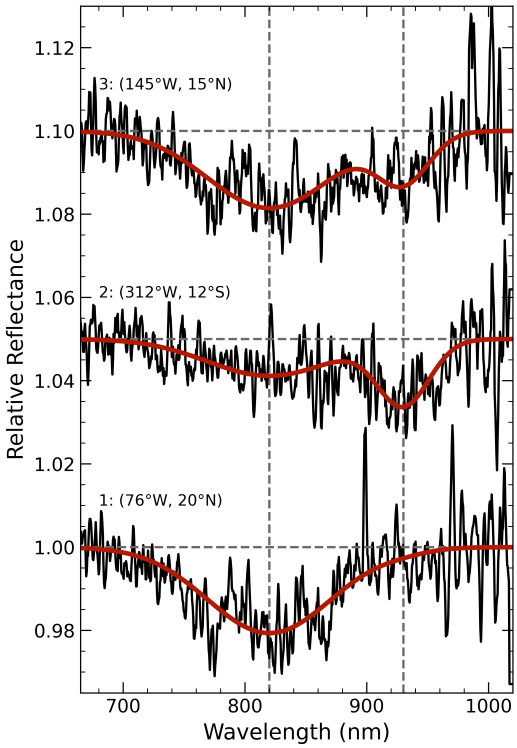

Figure 4.4: A selection of spectra showing regions on Callisto's surface where there is a clear 820 nm absorption with little to no 930 nm absorption (1: (76°W, 20°N)), a clear 930 nm absorption with a relatively weaker 820 nm absorption (2: (312°W, 12°S)), and relatively strong 820 and 930 nm absorptions which appear to merge into a single broader feature (3: (145°W, 15°N)). The spectra have been divided by a linear continuum (horizontal dashed lines), smoothed with a 5 pixel moving average filter, and offset for clarity. The 820 nm and 930 nm band centers are indicated by vertical dashed lines and a best-fit two Gaussian model is over-plotted in red. The location of each spectrum is indicated on the map in Figure 4.5 (a).

As seen in Figure 4.4, the relative ratio of the 820 nm and 930 nm absorptions varies across Callisto's surface, but both features are present in a majority of pixels with either band, hinting at a possible relation between the two. Because of the tendency to form what appears to be a single broad absorption, the combined strength of the 820 and 930 nm absorptions is mapped in Figure 4.5 (a). On the leading hemisphere, dark material within the inner and outer rings and directly south of

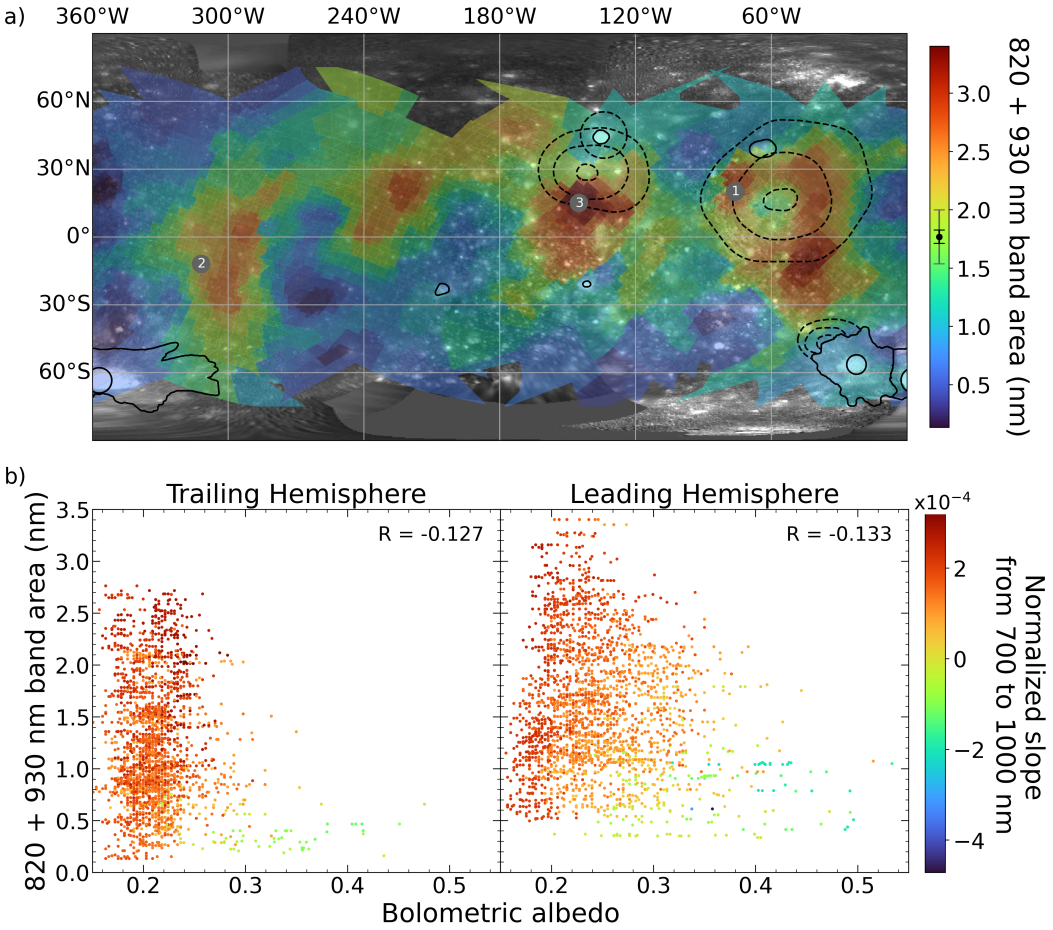

Figure 4.5: Map showing the calculated band area of the combined 820 and 930 nm absorption features (a), along with scatter plots (b) demonstrating that there is no notable correlation between the relative albedo of the dark material and the strength of the 820 and 930 nm bands and the very weak anti-correlation can largely be explained by the tendency for the highest-albedo pixels to have little to no sign of an 820 or 930 nm feature. Pixels with the strongest 820 and 930 nm absorptions tend to have fairly red NIR slopes, especially on the trailing hemisphere where almost all of the NIR reddest pixels (700 to 1000 nm slope $\gtrapprox 2 \cdot 10^{-4}$) have a relatively strong combined band strength. The estimated 1σ error for the calculated band area of each spatial pixel ranges from ±0.06 to ±0.23 nm and the minimum (black) and maximum (gray) estimated error is shown on the colorbar in panel (a). The gray circles on the map indicate the locations of the spectra in Figure 4.4 which demonstrate the overlap between the 820 and 930 nm bands.

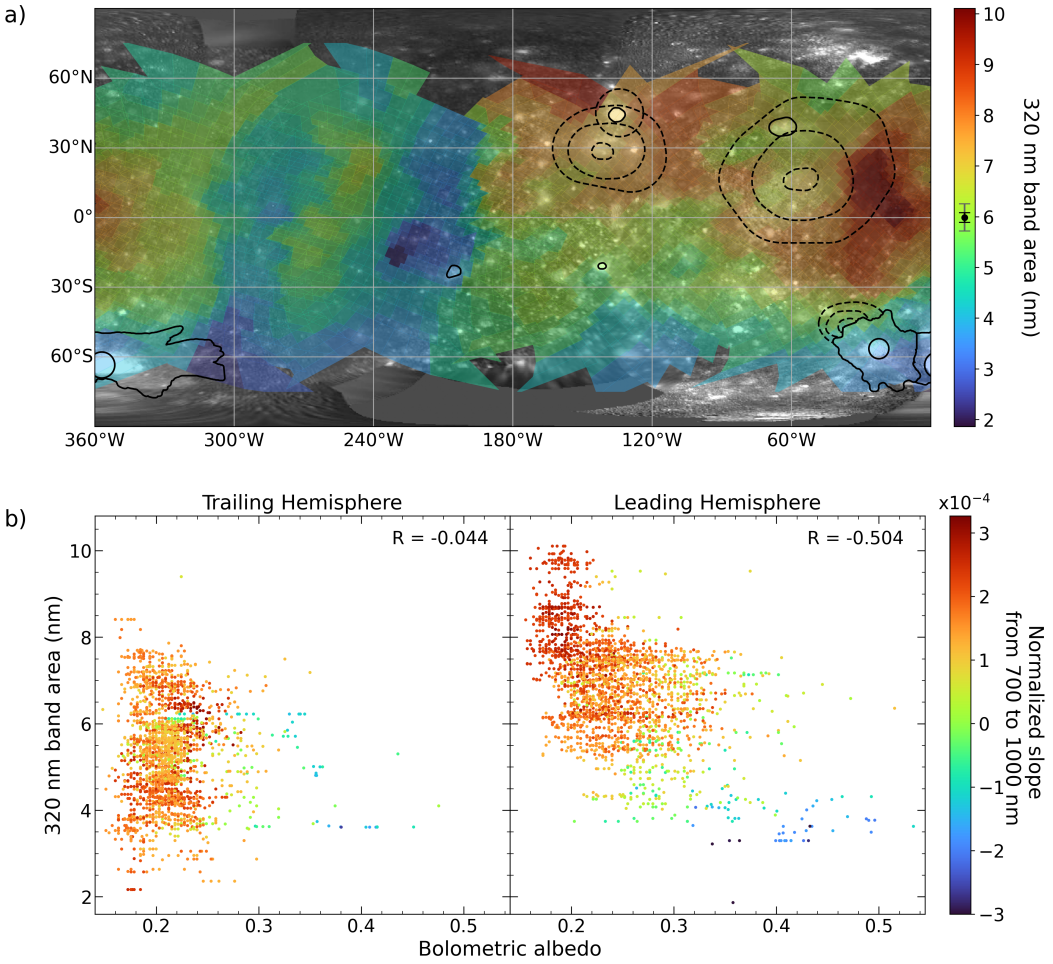

Figure 4.6: (a) The map of the strength of the 320 nm absorption demonstrates that it is largely constrained to the regions within and surrounding the Asgard and Valhalla impact basins which leads to clear hemispheric asymmetry. The scatter plots (b) reveal a moderately strong negative correlation with albedo, with the pixels displaying a significant 320 nm absorption tending to be both dark and NIR red. The strongest measured 320 nm band areas are associated with dark and red material directly east of Valhalla, which is partially within the outer ring or trough zone. The estimated 1σ error for the calculated band area of each spatial pixel ranges from ± 0.1 to ± 0.27 nm, and the minimum (black) and maximum (gray) estimated error is shown on the colorbar in panel (a).

the Valhalla impact basin show relatively strong combined 820 and 930 nm band strengths (see Figure 4.5 (a)). Visual inspection of the spectra reveal that much of the Valhalla impact basin has a strong 820 nm band and the 930 nm band is present in the south east section of the inner and outer rings but much weaker in the rest of Valhalla. Indeed, the region at the north west corner (near 76°W, 20°N) has a strong 820 nm band with no apparent 930 nm feature, as shown in Figure 4.4. The relatively bright and smooth central zone and the bright material associated with the recent impactors at the north-western corner of Valhalla (~65°W, 40°N) are the only regions within the impact basin with a relatively weak 820 and 930 nm combined band strength. Much of the terrain surrounding the Valhalla impact basin also has a very weak 820 and 930 nm band strength, suggesting that the presence of these features may be directly related to the Valhalla impactor itself. The dark material to the south of the Asgard impact basin and within its inner and outer rings also show relatively strong 820 and 930 nm absorptions, except where the bright material from the recent impactors Doh (141.4°W, 30.6°N) and Burr (134.5°W, 42.7°N) apparently cover the dark material with water-ice rich ejecta. Two additional large patches on Callisto's trailing hemisphere also show strong 820 and 930 nm combined band strengths, while both features are absent from much of the rest of the surface.

320 nm Absorption Feature

As can be seen in Figure 4.6 (a), Callisto's 320 nm absorption is constrained to the regions within and surrounding the Asgard and Valhalla impact basins. Pixels with a 320 nm absorption also tend to be dark and both UV and NIR red with the strongest measured band areas associated with the dark red material partially within the outer ring directly east of Valhalla. The bright material associated with fresh impact craters within Asgard and Utgard, which lack strong 820 nm and 930 nm absorption features and have relatively neutral NIR slopes, show strong 320 nm band strengths that are generally consistent with those measured in the darker material in and around the impact basins. This combined with the generally low band strengths seen for low- and mid- southern latitudes on the leading anti-Jovian hemisphere south of Asgard suggest that the strength of the 320 nm absorption feature may be more strongly associated with the Asgard and Valhalla impact basins than with the leading hemisphere dark material generally.

230 and 450 nm Absorption Features

The 450 nm absorption feature is inset on the broader near-UV downturn, which itself may be a composite of multiple overlapping absorptions with unidentified band parameters. As a result, the spectral continuum relative to the 450 nm absorption changes significantly across Callisto's surface. We find that while the band center of the 450 nm absorption feature appears to remain relatively consistent near 450 nm, the width, depth and shape of the continuum removed absorption feature varied significantly for different choices of polynomial degree and wavelengths included in the continuum fit and the true band parameters remain ambiguous. Attempts to map the spatial distribution of the 450 nm absorption feature produced qualitatively inconsistent results for different choices of the wavelengths included in a third order polynomial fit, and we find that we are unable to confidently map the distribution of this feature. Similarly, the 230 nm absorption feature is inset on the stronger 275 nm absorption edge. While the band center and width are more easily identified (~200 to 260 nm), we find that the increased noise in the UV observations, especially at the short-wavelength end of the spectrum, as well as a possible overlapping absorption feature short-ward of ~220 nm seen in some pixels affects the continuum fit. Additionally, the 230 nm feature is very weak relative to the 275 nm absorption edge, which has an unknown effect on the concavity of the spectrum at wavelengths near 230 nm and may artificially enhance measurements of the 230 nm band strength in some pixels, hindering attempts to consistently define a spectral continuum across Callisto's surface. Taken together, this makes mapping the strength of the 230 nm absorption feature difficult and we are again unable to confidently map the spatial distribution of this feature.

While our attempts to map the strength of the 230 nm and 450 nm absorption features were unsuccessful, visual inspection reveals that both features appear to be widespread over much of the surface of Callisto. Furthermore, pixels with a strong 450 nm signature also tend to have a visually stronger 230 nm absorption while pixels with the weakest observed 450 nm absorptions show little to no sign of a 230 nm feature, hinting at a possible but unconfirmed spatial association between the two features. While the 230 nm and 450 nm absorptions appear to be relatively widespread across Callisto's surface, it is interesting to note that the features appear to be extremely weak or possibly entirely absent from pixels containing the highest albedo material. This is consistent with the absorption bands resulting from a globally distributed component of the dark material, or with a more uniform exogenic delivery that is subsequently covered up by the fresh impact ejecta

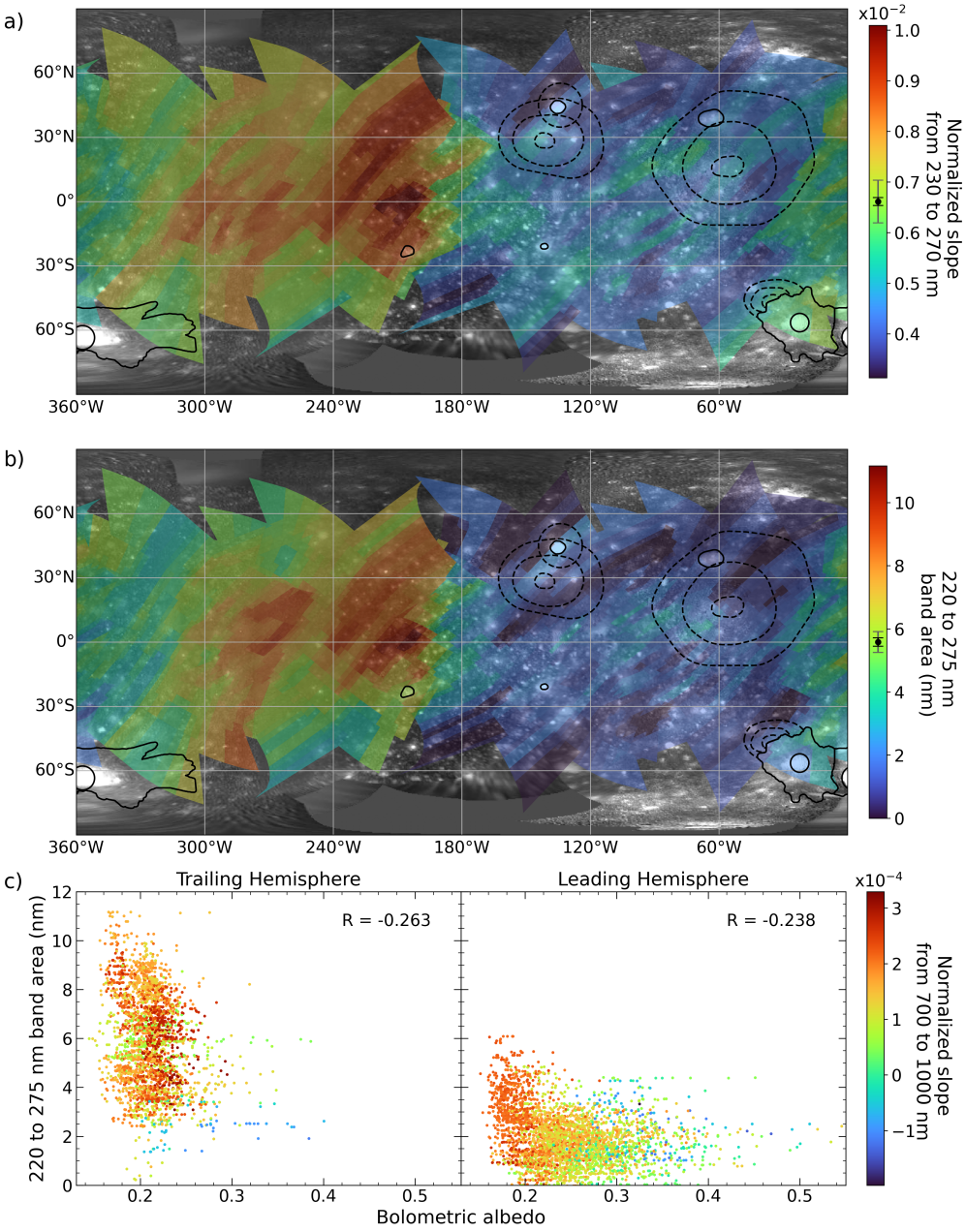

Figure 4.7: Maps showing our two proxies for the strength of the 275 nm absorption edge- (a) the normalized slope from 230 to 270 nm , and (b) the integrated band area (from 220 nm to 275 nm) after dividing by a base spectrum constructed from five pixels identified as having the weakest 275 nm absorption edge. The feature is constrained to the trailing hemisphere and is likely associated with the stronger irradiation environment, although the somewhat irregular distribution suggests that it may require radiolysis of an unevenly distributed endogenic species. (c) Scatter plots demonstrating that the 275 nm absorption edge is uncorrelated with the bolometric albedo. The estimated 1σ error for the calculated 230 to 270 nm slope and 220 to 275 nm band area of each spatial pixel ranges from $\pm 8.0\times10^{-5}$ to $\pm 4.2\times10^{-4}$ and ± 0.14 to ± 0.33 nm, respectively. The minimum (black) and maximum (gray) estimated error is shown on the colorbars in panels (a) and (b).

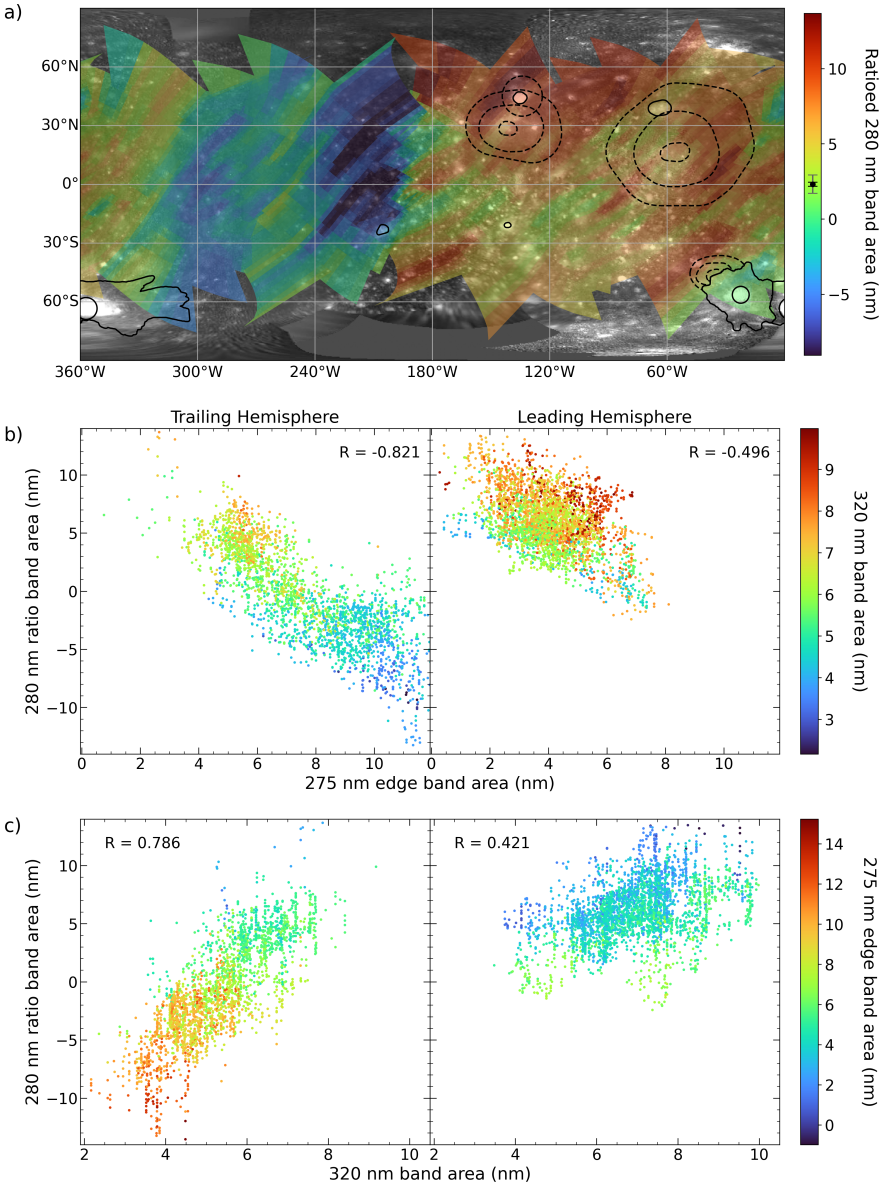

Figure 4.8: (a) Map showing the calculated band area of the 280 nm ratio feature for spectra ratioed with the center of the trailing hemisphere. Negative values represent pixels where the ratio spectrum is above the linear continuum and there is no apparent 280 nm feature present. As expected, the band is strongest on the leading hemisphere and largely absent from the trailing hemisphere. (b, c) Scatter plots demonstrating that the 280 nm ratio feature is strongly anti-correlated with the 275 nm absorption edge, especially on the trailing hemisphere and strongly positively correlated with the 320 nm absorption band. We interpret the 280 nm ratio band to be a direct consequence of these two absorption bands, which map strongly to separate hemispheres, and find that additional absorbers on the leading hemisphere (like SO_2) are not required to explain the spatial distribution of the ratio feature. The estimated 1σ error for the calculated band area of each spatial pixel ranges from ±0.13 to ±0.61 nm, and the minimum (black) and maximum (gray) estimated error is shown on the colorbar in panel (a).

typically associated with the bright water-rich material seen at the global scales considered here.

275 nm Absorption Edge

Both measurements of the strength of the 275 nm absorption edge are mapped in Figure 4.7. Qualitatively, the two maps agree quite well and the 230 to 270 nm slope and 220 to 275 nm integrated band area are strongly correlated ($R = 0.914$). It is clear from these maps that Callisto's 275 nm absorption edge is constrained to the trailing hemisphere, suggesting that it may be associated with the fast rotating plasma bombarding Callisto's trailing hemisphere (Johnson et al., 2004). However, its distribution does not match the bullseye pattern which is expected for species that are radiolytically produced from this plasma bombardment (e.g. CO_2) (Cartwright et al., 2024; Hibbitts et al., 2000). The 275 nm absorption may require both the more intense irradiation environment of the trailing hemisphere and endogenic material which is not evenly distributed, explaining its absence on the leading hemisphere as well as its uneven distribution across the trailing hemisphere. The scatter plots in Figure 4.7 (c) show that there is not a significant correlation between the strength of the absorption edge and the albedo.

Both maps in Figure 4.7 show minor diagonal striping orthogonal to the scan direction, likely due to uncorrected instrumental artifacts. However, the striping does not correlate with surface features and has a magnitude which is smaller than the estimated 1σ uncertainties on the band strength measurements, so we expect that this striping has a minimal effect on the interpretation of the observations.

280 nm Ratio Feature

The strength of Callisto's 280 nm ratio feature is mapped in Figure 4.8 (a). We expect that minor diagonal striping, as described previously for the 275 nm absorption edge, should have a minimal effect on the interpretation of the spatial distribution. As expected from the disk averaged observations of Noll et al. (1997), Callisto's 280 nm ratio feature is largely constrained to the leading hemisphere, although it is also present on the trailing hemisphere at longitudes larger than ~300°W. The ratio feature appears to be absent from the regions on the trailing hemisphere that show the strongest 275 nm band strengths, explaining the strong anti-correlation displayed in Figure 4.8 (b). There is a similarly strong positive correlation with the 320 nm absorption shown in panel c. We therefore propose that the presence of the 280 nm ratio feature, and its prevalence on the leading hemisphere, may be an artifact of

the strong 275 nm absorption edge present across much of the trailing hemisphere and the 320 nm absorption on the leading hemisphere. Indeed, taking the ratio of spectra containing the strongest 320 nm absorptions to those with the strongest 275 nm edge show a very strong 280 nm ratio feature with a similar band profile as that in the disk averaged ratio. See Section 4.5 for further discussion.

4.5 Comparison of Spectral Features to Laboratory Spectra

We have completed a thorough search through the United States Geological Survey (USGS) (Kokaly et al., 2017), Winnipeg Planetary Spectrophotometer Facility (PSF) (Cloutis, 2015), Keck/NASA Reflectance Experiment Laboratory (RELAB) (Pieters et al., 2004) , and Solid Spectroscopy Hosting Architecture of Databases and Expertise (SSHADE) (Schmitt et al., 2018) spectral libraries as well as a general literature search in order to find plausible spectroscopic matches to the observed Callisto spectra. In the following sections we discuss plausible matches for each of the observed features. When possible, we consider laboratory spectra obtained at cryogenic temperatures or which have been irradiated to simulate the effects of magnetospheric particle bombardment and space weathering. However, a majority of the available laboratory spectra are acquired from rock or powdered samples at room temperature and therefore do not capture the spectral changes associated with cryogenic temperatures, grain size differences, and space weathering effects, which are expected under Callisto-like conditions (e.g. Escobar-Cerezo et al., 2018; Kohout et al., 2014; Singer et al., 1985). The spectral identifications discussed in the text therefore remain preliminary and future laboratory work under conditions relevant to the Galilean satellites will be required to confirm many of these plausible spectral matches.

820 and 930 nm Absorptions

A wide variety of materials of relevance to planetary surfaces have absorption features with band centers near 820 and 930 nm, typically attributed to Fe-related electronic absorptions. We do not find any obvious or unambiguous spectral matches for either feature, however we consider a range of plausible species with interesting implications for Callisto's surface composition in the following subsections including structured silicates like orthopyroxene, sulfates and other sulfur-bearing species, phyllosilicates, and iron oxides and other weathering products.

Orthopyroxene and Iron Oxides

Several low calcium orthopyroxenes exhibit a broad 930 nm Fe^{2+} vibrational band

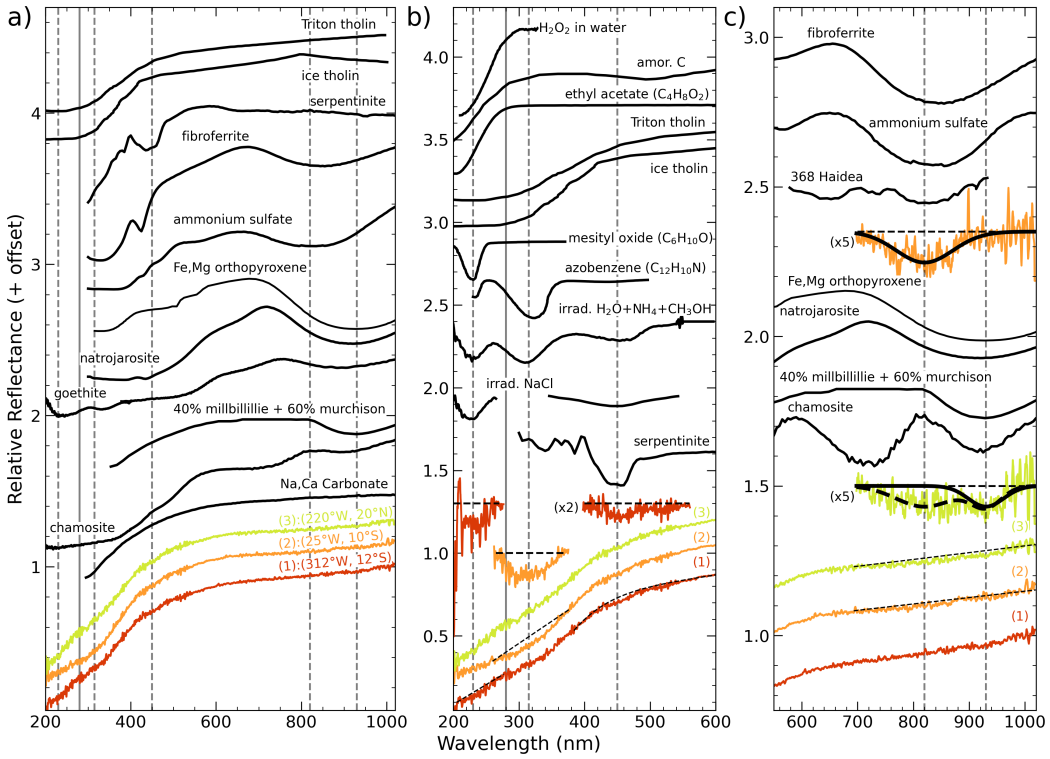

Figure 4.9: Comparison between select Callisto spectra and some laboratory spectra discussed in the text. The color and associated number for each Callisto spectrum correspond with the locations mapped in Figure 4.1 (a) and the longitude and latitude are listed in panel (a). Examples of local continuum fits, indicated with black dashed lines, and corresponding continuum removed features for the 230, 320, 450, 820, and 930 nm absorption features are shown in panels (b) and (c). The approximate positions of the band centers for the 230, 320, 450, 820, and 930 nm absorption bands are indicated with vertical dashed gray lines and the position of the long wavelength shoulder of the 275 nm absorption edge is indicated by the solid gray line. Individual laboratory spectra are shown and labeled in black. As discussed in detail in Section 4.5, the identification of specific minerals to explain each UV and visible absorption feature on Callisto is difficult, and identifications typically remain ambiguous. However, we use some of the potential spectral matches, in combination with the spatial distributions of the features, to explore possible compositions in the text. Laboratory spectra in panel (a) include the Na- and Ca- bearing carbonate shortite (PSF sample CRB126), the phyllosilicate chamosite (PSF sample CHM102), an intimate mixture of the orthopyroxene-rich Millbillillie eucrite meteorite and phyllosilicate-rich Murchison CM2 chondrite (Cloutis et al., 2013), the iron oxide goethite (USGS sample WS222), the sodium sulfate natrojarosite (PSF sample SPT108), the Fe,Mg orthopyroxene enstatite (En30; Klima et al. (2007)), ferric ammonium sulfate (PSF sample SPT104), the iron sulfate fibroferrite (Cloutis et al., 2006), the phyllosilicate serpentinite (PSF sample SRP105), and laboratory tholins produced by irradiation of mixtures of H_2O:CH_3:CO_2:C_2H_6 ices (ice tholin; McDonald et al. (1996)) and N_2:CH_4 ices (Triton tholin; Cruikshank et al. (2005)).

Figure 4.9 (cont): Panel (b) includes the continuum removed 450 nm feature from the serpentinite spectrum in panel (a), continuum removed spectra of irradiated NaCl at Europa-like conditions (Brown et al., 2022), continuum removed spectra of irradiated mixtures of H_2O:NH_4:CH_3OH ices that are warmed to 120 K post-irradiation (Wong et al., 2019), the Triton and ice tholins from panel a, spectra of the liquid phase organics azobenzene, mesityl oxide, and ethyl acetate from NIST (Talrose et al., 2001), amorphous carbon (Duley, 1984), and 0.16% H_2O_2 in water ice (Carlson et al., 1999a). Panel c includes continuum removed spectra of chamosite, the Millbillillie eucrite and Murchison CM2 chondrite mixture, natrojarosite, orthopyroxene, ferric ammonium sulfate, and fibroferrite from panel a, as well as a spectrum of the asteroid 368 Haidea from Vilas et al. (1994).

(e.g. Cloutis, 2002; Klima et al., 2007), and iron oxides like maghemite or goethite and some iron sulfides like jarosite have a strong ~930 nm Fe^{3+} spin-forbidden absorption (e.g. Bishop et al., 2019; Hunt et al., 1979). See Figure 4.9 (a) and (c) for example spectra of an Fe-Mg orthopyroxene (enstatite En30 from Klima et al. (2007)), the iron oxide goethite (USGS sample WS222), and the Na-bearing sulfate natrojarosite (PSF sample SPT108). While all three example spectra have a strong absorption band near 930 nm, it is clear that the absorption is significantly broader than what is seen on Callisto. Indeed, all laboratory spectra of typical (Ca-poor) orthopyroxenes, (hydr)oxides, and iron sulfates considered in this study have a ~900 nm absorption that is significantly broader than is seen on Callisto, though crystal field absorptions are expected to become narrower at low temperatures. However, limited cryogenic laboratory data of enstatite (Mg-bearing orthopyroxene) (Singer et al., 1985) and hematite (Morris et al., 1997), suggest that the ~900 nm absorption does not narrow significantly enough to explain the discrepancy. Additionally, iron oxides like goethite typically have an electronic Fe- absorption band near 650 nm and an Fe-OH doublet near 2.4-2.5 μm (Bishop et al., 2019) which we do not see in any available spectra of Callisto, suggesting that iron oxides are unlikely to be responsible for the 930 nm absorption.

Callisto's 820 nm absorption band is a surprisingly good match to the continuum removed spectra of 368 Haidea and 165 Loreley (see Figure 4.9 (c)), two low-albedo asteroids which may have undergone less thermal alteration than the majority of C-type asteroids (Vilas et al., 1994). Vilas et al. (1994) suggest that this ~820 nm absorption may arise from Fe^{3+}-Fe^{2+} charge transfer absorptions in a combination of iron alteration minerals including iron oxides like goethite and hematite. They suggest that the absorption may shift to shorter wavelengths at the lower temperatures

experienced at the far edge of the asteroid belt (~195 K at 4 AU). However, we have already found that many of the iron oxides are a poor match to the 930 nm feature and the shortest wavelength band minimum for any of the iron oxides studied at 160 K in Morris et al. (1997) is at 860 nm, which cannot explain the 820 nm band minimum observed on Callisto. Additionally, the spectra of 368 Haidea and 165 Loreley include a prominent absorption near 650 nm which is also attributed to Fe^{3+} and expected in goethite (see Figure 4.9 (a)) and hematite, and which we do not see on Callisto. We therefore conclude that an association of Callisto's 820 nm band with iron alteration minerals, as is suggested for 368 Haidea and 165 Loreley, remains unconvincing. We note, however, that while we do not find convincing evidence of large-grained Fe-alteration minerals, we cannot rule out the presence of sub-micron or nano-phase iron or iron oxides, which are an expected space weathering product of Fe-bearing minerals (e.g. Clark et al., 2012). Nano-phase iron and iron oxides lack the distinct absorption bands seen in their larger grained counterparts and could produce a general, but non-diagnostic, darkening and reddening of Callisto's UV and visible wavelength spectra while perhaps also weakening the strength of the mineral absorption bands (e.g. Clark et al., 2012; Escobar-Cerezo et al., 2018; Kohout et al., 2014).

Sulfates

The effects of temperature and irradiation on hydrated sulfate minerals to the visible-NIR spectrum has not been studied extensively in the lab, and it remains uncertain whether the ~900 nm band common in many sulfates could narrow significantly enough to match Callisto's 930 nm feature. In addition to the strong ~900 nm absorption, iron-bearing sulfates like jarosite also tend to have an Fe- related feature near 430 nm which could help explain Callisto's 450 nm band. However, the 430 nm band in Fe-bearing sulfates tends to be sharper and narrower than what is seen on Callisto, and Callisto's 450 nm band appears to be more widespread across the surface than the 930 nm absorption, suggesting that they do not arise from the same material. Sulfates also tend to have additional absorption features due to the sulfate anion (SO_4^{2-}) near 1.74-1.85 and 4-5 μm as well as an OH related feature near 2.2-2.3 μm (Bishop et al., 2019). Galileo/NIMS observations of Callisto's dark material show possible absorption features near 2.31 and 1.8 μm (Moore et al., 2004) which could be consistent with the presence of hydrated sulfate minerals, however NIMS spectra contain spurious radiation spikes and currently neither the 1.8 or 2.31 μm features have been confirmed with another dataset. In a recent analysis of JWST/NIRSpec observations of Callisto, Cartwright et al. (2024) suggest

that Na-bearing sulfate could be responsible for the 3.72 μm absorption and find additional absorption features near 4.38, 4.57, and 4.92 μm which are potentially consistent with nearby absorptions in the laboratory spectrum of natrojarosite and other sulfates analyzed here. However, Cartwright et al. (2024) find that the 4.57 μm band is strongest at southern latitudes on the anti-Jovian hemisphere, where we find no sign of the 930 nm band, and both the 4.38 and 4.92 μm bands, while not mapped, are somewhat stronger in the average trailing hemisphere JWST spectrum than in the leading (anti-Jovian) hemisphere spectrum. It therefore remains uncertain whether Na-bearing sulfates could be responsible for Callisto's 930 nm absorption or any of the NIR features, although it is clear from their differing spatial distributions that a single sulfate mineral cannot be responsible for all of these features.

There are some Fe^{3+}-sulfates that have a band minimum between 800 and 820 nm (e.g. rhomboclase, fibroferrite) (Cloutis et al., 2006), however the absorptions in available laboratory spectra are broader than Callisto's 820 nm band, and as previously discussed for the 930 nm feature, it remains uncertain whether the crystal field bands in sulfate minerals will narrow sufficiently with temperature. Interestingly, ferric ammonium sulfate has a band center at 820 nm with a narrower band width than other non-NH_4-bearing sulfates, offering the best match to Callisto's 820 nm feature out of all of the laboratory sulfate spectra considered (see PSF sample SPT104 in Figure 4.9 (a) and (c)). While ammonia-bearing compounds have been suggested on Callisto based on a possible weak band near 3.05 μm, spectroscopic evidence for NH_4 on Callisto is ambiguous at best (e.g. Calvin et al., 1993; Cartwright et al., 2024) and NH_4^+ bands near 2.55-2.65 μm have not been identified in existing NIR datasets. However, there are a surprising number of recent detections of NH_4-bearing species on surfaces within the orbit of Saturn, including ammoniated phyllosilicates on the main-belt asteroids Ceres and Hygiea (De Sanctis et al., 2015; Rivkin et al., 2025), possible detections of NH_4-bearing salts or carbonates on Ganymede from Juno/JIRAM (Tosi et al., 2024), and the detection of ammoniated phyllosilicates on the Himalia family of Jovian irregular satellites (Sharkey et al., 2025). This suggests that not only is the presence of endogenic NH_4-bearing species on Callisto plausible, but some amount of NH_4-bearing species are almost certainly delivered to Callisto's surface by the prograde irregular satellite dust sourced from the Himalia family (Bottke et al., 2013; Chen et al., 2024). The 820 nm band in the ferric ammonium sulfate laboratory spectra is much stronger than any of the other NIR features, and if an ammonium-bearing sulfate is responsible for Callisto's very weak 820 nm absorption, it is unlikely that any additional absorptions (e.g. the very

weak 1.7-1.85 and 4-5 μm SO_4^{2-} bands) would be discernible on Callisto.

Fe^{2+}- Phyllosilicates

Phyllosilicates might provide a better match to Callisto's 930 nm absorption as several iron-phyllosilicates common in CM chondrites show an Fe^{2+} band near 900-940 nm with a band width that is more comparable, although still slightly broader, than Callisto's 930 nm feature (Cloutis et al., 2011a). An example spectrum of chamosite (PSF sample CHM102), an Fe-rich chlorite, is shown in Figure 4.9 (a), and the polynomial continuum removed feature is compared with Callisto's 930 nm band in panel (c). The band is much narrower than those seen in most orthopyroxenes, (hydr)oxides, and sulfates, providing a much closer match to Callisto, and it may narrow further at cryogenic temperatures although this has not yet been tested in the lab. The possible presence of phyllosilicates within Callisto's dark material is supported by the modeling work of Calvin et al. (1991) and Calvin et al. (1995), who demonstrate that the non-ice component of Calliso's spectrum from 0.2 to 4 μm can be well-fit by models including the phyllosilicate serpentine. However, these models are based on very low resolution ground-based spectra from before Galileo arrived at the Jovian system and more recent observations with Galileo/NIMS and JWST (e.g. Cartwright et al., 2024; Moore et al., 2004) do not show any unambiguous sign of the ~2.7 μm characteristic phyllosilicate band (Bishop et al., 2019), although it is possible that this feature may be obscured by a stronger 3 μm band associated with H_2O ice and other more abundant hydrated minerals. The laboratory spectrum of chamosite and other Fe/Mg phyllosilicates is a reasonable match to several additional NIR features on Callisto, including the OH band near 2.25-2.35 μm which is near the potential 2.31 μm band seen in some NIMS spectra. Additionally, chlorites like chamosite have a weak doublet near 3.4 and 3.5 μm which is very close to the 3.43 and 3.51 μm bands seen in NIMS observations and typically attributed to carbon-bearing minerals (e.g. Bishop et al., 2019; McCord et al., 1998). However, we note that while Cartwright et al. (2024) suggest that the weak 3.43 and 3.51 μm absorptions seen in the JWST/NIRSpec observations are likely real based on their correspondence to features detected in past NIMS observations, similar features detected in NIRSpec spectra of Ganymede are suggested to arise from calibration artifacts (Bockelee-Morvan et al., 2024). The bands in the JWST observations have a similar spectral contrast as other artifacts and are significantly weaker than would be expected based on the NIMS observations, which were heavily plagued by spurious radiation spikes. While it is therefore possible that the 3.43 and 3.51 μm bands are spurious and not present on Callisto, ground-based observations also show

a possible weak band near 3.4 μm (Cartwright et al., 2020) and the recent JWST spectra of the Jovian irregular satellites reveal a stronger 3.43 μm band attributed to aliphatic organics (Sharkey et al., 2025), perhaps suggesting that these bands are real on both Ganymede and Callisto, but related to C-H bearing organics delivered by the irregular satellite dust rather than phyllosilicates.

Additionally, there is no evidence in any of our HST spectra for the relatively strong ~700 nm $Fe^{2+}-Fe^{3+}$ charge transfer absorption seen in the chamosite spectrum in Figure 4.9 that is typical in iron-bearing phyllosilicates, which are usually found in mixed valence. If single valence Fe^{2+}-phyllosilicates are responsible for Callisto's 930 nm feature, then they are apparently uniquely devoid of Fe^{3+} which is responsible for the ~700 nm absorption attributed to phyllosilicates in many solar system bodies including carbonaceous chondrites, asteroids, on Ceres, and even in one Kuiper belt object (e.g. Rivkin, 2012; Rizos et al., 2019; Seccull et al., 2018). Recent irradiation experiments bombarding a sample from the Murchison CM2 meteorite with 1 keV H^+ and He^+ ions to simulate the solar wind resulted in reduction of some of the Fe^{3+} within the phyllosilicate component to Fe^{2+} or metallic iron (Laczniak et al., 2021). It is therefore possible, although unproven, that the unique oxidation and irradiation environment on Callisto's surface could result in more efficient reduction of Fe^{3+} in native (or delivered) phyllosilicates, perhaps reducing much of the Fe^{3+} content to Fe^{2+} or sequestering it into largely featureless weathering products like nanophase iron, and resulting in a 930 nm feature with an absent or very weak 700 nm absorption.

Meteoritic analogues for the 930 nm feature

While low-calcium orthopyroxene and Fe-phyllosilicates are among the best contenders for explaining Callisto's 930 nm absorption, neither species offers a convincing match to the 930 nm band on its own. Orthopyroxenes require a more significant narrowing of the pyroxene band at low temperatures than is currently supported by laboratory data and the Fe-phyllosilicates require a very atypical single valence Fe^{2+}-phyllosilicate or some other mechanism for suppressing the 700 nm charge transfer band. It turns out, however, that an intimate mixture of orthopyroxene and Fe-phyllosilicates may simultaneously explain both the narrowness of the 930 nm band and the absence of the ~700 nm phyllosilicate absorption on Callisto. Indeed, Cloutis et al. (2013) analyze laboratory measurements of mixtures of fine-grained samples of the Millbillillie eucrite meteorite, whose spectrum is dominated by a broad ~950 nm absorption attributed to Fe^{2+}-rich low-calcium pyroxene, and the

Murchison CM2 carbonaceous chondrite with a spectrum characterized by an overall red slope and shallow ~700-1200 nm absorption feature which is a composite of the 700 nm Fe^{2+}-Fe^{3+} charge transfer band and the ~920 nm Fe^{2+} crystal field transition in phyllosilicates (predominantly cronstedtite and serpentine). They find that for intimate mixtures of the two meteorites, the resulting spectrum is dominated by the ~900 nm pyroxene band and there is no compelling evidence for the presence of the expected phyllosilicate absorption band near 700 nm even for mixtures with 60 wt.% phyllosilicate-rich CM2. Additionally, they show that increasing amounts of the murchison CM2 in the intimate mixtures shifts the pyroxene band to shorter wavelengths (933 nm for 60 wt.% CM2) and results in a shallower band depth with a small but measurable reduction in the band width. A mixture of 40% orthopyroxene rich Millbillillie with 60% phyllosilicate rich Murchison from Cloutis et al. (2013) is shown in Figure 4.9 (c) and is remarkably consistent with the weak and narrow 930 nm band measured on Callisto.

If Callisto's 930 nm band arises from a mixture of orthopyroxene and phyllosilicates, it may not be surprising that it is apparently associated with the large impact basins. Typical silicates like orthopyroxene are common throughout the solar system and may be present in Callisto's endogenic rocky material or be delivered from the giant impactors themselves. Heat generated by the basin forming impacts into Callisto's ice-rich surface could have produced melt which resulted in the aqueous alteration of some of the original orthopyroxene into phyllosilicates.

230 and 450 nm Absorptions

We were unable to map the spatial distributions of the weak 230 nm and 450 nm absorption features (see Section 4.4). However, visual inspection of the individual spectra reveals that both features are present across a majority of Callisto's surface, and their strengths may be correlated. If the 230 nm and 450 nm absorptions arise from the same material, they may be a reasonable spectroscopic match to irradiated NaCl, which was recently detected within chaos terrains on Europa's leading hemisphere via color center absorptions at 230 nm and 450 nm (Trumbo et al., 2022a, 2019b). Figure 4.9 (b) shows a continuum removed laboratory spectrum of irradiated NaCl at Europa-like conditions (Brown et al., 2022) along with the continuum removed 230 and 450 nm absorptions on Callisto. The 450 nm band center is a reasonable match to the NaCl laboratory spectrum as well as Europa's 450 nm feature, but Callisto's continuum removed feature appears to be significantly narrower than expected for NaCl. However, the 450 nm absorption feature is inset

on the broader near-UV downturn and ~415 nm slope break, and it is difficult to discern the spectral continuum in this region of Callisto's spectrum, so the exact band shape and width of Callisto's 450 nm feature remains ambiguous. Indeed, as discussed in Section 4.4, changes to the wavelengths included in the continuum polynomial fit significantly alter the apparent 450 nm band width and shape and we conservatively choose the continuum fit displayed in Figure 4.9 (b) to highlight the deepest, most visually obvious portion of the absorption. We suspect that the true band width of Callisto's 450 nm absorption may be broader than the narrow region captured by this choice of continuum, perhaps extending to ~370 nm on the short wavelength end where there is a small divet in many of the spectra with strong 450 nm absorption's that is visually similar to that seen for the 450 nm NaCl feature on Europa. The 230 nm absorption observed on Callisto is also a reasonable match, in both band center and width, to the NaCl laboratory spectra as well as Europa's 230 nm absorption.

Alternatively, Callisto's 450 nm absorption is a reasonable visual match to the 450 nm spin-forbidden electronic transition of tetrahedrally-coordinated Fe^{3+} in hydrated minerals like serpentines (Burns, 1993) (see serpentinite spectrum from PSF sample SRP105 in Figure 4.9). Indeed, models including serpentine have been shown to fit Callisto's 0.2 to 4 μm spectrum reasonably well (Calvin et al., 1991, 1995), albeit at relatively low spectral resolution, and many serpentines have a characteristic OH band near 2.3 μm which may explain the potential 2.31 μm band seen in some NIMS spectra. If this feature is related to a phyllosilicate like serpentine, the apparently widespread distribution of the 450 nm band suggests that it is either delivered from irregular satellite dust or excavated from the subsurface, and it cannot be directly related to the potentially phyllosilicate-bearing material responsible for the geographically constrained 930 nm absorption.

275 nm Absorption Edge

The 275 nm absorption edge, seen predominantly on Callisto's trailing hemisphere, has been attributed to the presence of hydrogen peroxide (H_2O_2) produced via irradiation of water ice (Hendrix et al., 1999). The laboratory spectrum of 0.16% H_2O_2 in water ice (Carlson et al., 1999a), as shown in Figure 4.9 (b), is indeed a reasonable visual match to Callisto's 275 nm absorption edge. However, neither Galileo/NIMS or the more recent JWST/NIRSpec observations of Callisto show any evidence of a 3.5 μm peroxide absorption which is seen on Europa and Ganymede (Carlson et al., 1999a; Trumbo et al., 2023, 2019a). It is possible that the concentration of H_2O_2

on Callisto may be low enough that the strong electronic transition band near 210 nm is observed, while the much weaker 3.5 μm O-H stretch vibrational overtone is masked. Alternatively, Hendrix et al. (2008) also suggest that the reddening of the spectral slope towards shorter UV wavelengths may be dominated by carbon-based species. In either case, the feature is strongly geographically constrained to the trailing hemisphere and we expect that the species responsible for the 275 nm absorption edge is an irradiation product associated with the stronger magnetospheric bombardment experienced by Callisto's trailing hemisphere. If the 275 nm absorption edge is associated with H_2O_2 in irradiated water ice, then we might expect the strongest band strengths to be associated with the bright material. However, as can be seen in Figure 4.7 (c), we find the strongest band strengths are associated with very low albedo ($\lesssim$0.2) water-poor material. This suggests that an association with organics is the more likely explanation and could indicate that the 275 nm absorption edge is caused by irradiation-induced alteration of dark carbon-rich material through some process (e.g. carbonization) which requires the higher irradiation fluxes experienced on Callisto's trailing hemisphere. Indeed, Callisto's CO_2 signature is strongest on the trailing hemisphere and appears to be related to the magnetospheric bombardment, perhaps consistent with an irradiated carbon-bearing material producing both CO_2 and heavily carbonized organic molecules responsible for the 275 nm absorption edge (Cartwright et al., 2024; Hibbitts et al., 2002, 2000). See Section 4.5 for further discussion of the 275 nm absorption edge in the context of organic species on Callisto.

320 nm Absorption and Other Plausible Organic Features

The newly identified 320 nm absorption feature, seen predominantly in and around the Valhalla and Asgard impact basins on Callisto's leading hemisphere, may be related to the 280 nm rollover seen in the Galileo/UVS spectra (210 - 320 nm), which Hendrix et al. (2008) attribute to organic absorption. They suggest this feature is strongest in the south polar region, where they measured steep blue slopes from 280–320 nm, and propose that organics may be progressively weathered at low latitudes by UV, charged particle, and micrometeorite bombardment. Our HST/STIS observations do not extend to the south pole, but we find that the 320 nm absorption is generally weak at mid-high southern latitudes, and regions with the strongest absorption do not consistently exhibit blue 280–320 nm slopes. While the 320 nm feature could still be linked to the material responsible for the 280 nm rollover, our broader wavelength coverage reveals a spatial distribution that differs

significantly from that inferred in Hendrix et al. (2008). Nevertheless, the 320 nm absorption remains consistent with the presence of organic molecules, long considered a plausible component of Callisto's dark material (e.g. Hendrix et al., 2008; McCord et al., 1997, 1998), though its precise origin warrants further study.

Unsaturated organics, molecules that contain at least one double or triple carbon bond, have strong UV absorption bands associated with a $\pi-\pi^*$ electronic transition that often occur at wavelengths between 200 and 500 nm (Kalsi, 2007), many of which could present a plausible match to Callisto's 320 nm band, 275 nm absorption edge, and possibly even the 230 and 450 nm features. However, the identification of specific organic molecules or sub-types are typically not possible from UV and visible absorption features as small changes to the molecular structure such as the inclusion of one additional double bond can shift the band position by up to 30 nm at a time (Kalsi, 2007). Existing literature exploring the production (or destruction) of organics by irradiation of carbon and nitrogen bearing species, especially at Callisto-like conditions, is sparse and the influence of these organics on the UV and visible wavelength reflectance spectrum has not been well studied in the laboratory. Recent experiments simulating the effect of solar wind on the murchison CM2 meteorite showed that H^+- and He^+- irradiation may affect the organic functional group chemistry in different ways, with H^+ breaking down macromolecular material and increasing the abundance of low-molecular-weight free organic species while He^+ decreases the overall organic content (Laczniak et al., 2021). The radiolytically induced organic chemistry on carbon-rich surfaces apparently depends on the bombarding species and energy, and the balance of constructive and destructive processes in the much more intense irradiation environment at Callisto is unknown. Further complicating the picture, laboratory studies of meteorites reveal a large diversity of organic molecules which range from simple ones like amino acids and carboxylic acids to more complex species like polycyclic aromatic hydrocarbons and macromolecular organic matter (e.g. Cloutis et al., 2011a,b) and it is likely that the organic component on Callisto has a similar diversity of species resulting in a complex mixture of bands presented in the UV spectrum. With this in mind, we discuss several types of organic species below with example spectra shown in Figure 4.9 that provide a plausible visual match to some of Callisto's UV spectral features, but we by no means suggest that any of these particular species are present on Callisto. Instead, we ask the reader to view this as a demonstration that organic molecules of a variety of types can offer a plausible match to many of Callisto's UV features.

Recent observations of several of the Jovian irregular satellites with JWST/NIRSpec revealed strong (~1-3% band depths) 3.4 μm absorptions attributed to aliphatic organics on all five of the observed retrograde satellites and on at least one of the prograde Himalia family moons (Sharkey et al., 2025). These organics are delivered to Callisto via irregular satellite dust grains and likely explain the 3.43 μm band reported in both the leading and trailing hemispherically averaged spectrum from JWST (assuming it is not an artifact as in Bockelee-Morvan et al. (2024)) (Cartwright et al., 2024). The relatively weak ($\lesssim$1%) 3.43 μm band depths measured in the Callisto JWST spectra could arise from this dust mixing with other species on the surface, or it might indicate that some of these delivered organics are radiolytically altered and incorporated into new species (Cartwright et al., 2024; McCord et al., 1997). Callisto's 4.57 μm band has also been suggested to arise from C-N (or C-S) bearing organics delivered directly from irregular satellite dust (Cartwright et al., 2020, 2024), however the 4.57 μm band and any spectral indication of S-bearing species is notably absent from the irregular satellite JWST spectra (Sharkey et al., 2025). Instead, the 4.57 μm band may arise from the irradiation of NH_4-bearing compounds delivered by the dust which mixes with native H_2O ice and carbon-rich material or CO_2, perhaps following a similar radiolytic pathway as mixtures of N^-, C^-, H^-, and O^- bearing ices which form a variety of new radiolytic products such as OCN^- and long-chain refractory organics with C-H and C-N stretching modes (Accolla et al., 2018; Cartwright et al., 2024; Sharkey et al., 2025). An understanding of the spatial distribution of the 3.43 μm band and how it relates to the 4.57 μm feature on Callisto may help determine whether the organics delivered by the irregular satellite dust are cannibalized and incorporated into the more refractory organics tentatively associated with the 4.57 μm band. Regardless, irradiation of carbon-bearing and ice-rich materials have been shown to create a variety of complex organic molecules in laboratory simulations (see e.g. Accolla et al., 2018; Faure et al., 2021; Marcellus et al., 2017; Palumbo et al., 2004; Urso et al., 2020) and we expect that radiolytic processing plays a crucial role in the formation of organics on Callisto and is required to explain the apparently vastly different spatial distributions of the 320 nm, 3.43 μm, and 4.57 μm absorptions if the interpretation that they result from organic materials is correct.

Some laboratory tholins, like those suggested to explain the prominent 4.57 μm absorption can also exhibit strong UV bands (Cartwright et al., 2024; Gavilan et al., 2017; McCord et al., 1997). Figure 4.9 (a) and (b) shows the reflectance spectrum, calculated via Hapke modeling (as in Hendrix et al. (2010)) from laboratory optical

constants for an ice tholin and Triton tholin produced via irradiation of a mixture of H_2O:CH_3OH:CO_2:C_2H_6 (McDonald et al., 1996) and N_2:CH_4 (Cruikshank et al., 2005) ices, respectively. The start of a strong UV absorption edge in the ice tholin aligns well with the long wavelength edge of Callisto's 320 nm absorption, and the Triton tholin shows a drop-off towards the UV starting at slightly longer wavelengths. While the laboratory tholin absorption edges continue to shorter wavelengths and are therefore not a spectral match to Callisto's 320 nm feature, we can not rule out a possible contribution from such tholin like organics to the 320 nm band, or to the generally red UV slopes and near-UV downturn which are ubiquitous across Callisto's surface. Regardless, tholin-like organics are unlikely to fully explain the band width and shape of the observed 320 nm band, and additional species are required.

Interestingly, irradiated mixtures of H_2O:NH_4:CH_3OH ices that are warmed to 120 K post-irradiation in a recent experiment designed to explore the irradiation and heating history of the Jupiter Trojans (Mahjoub et al., 2016; Poston et al., 2018) provide a remarkably good match to the 230, 320, and 450 nm absorption bands seen on Callisto. The continuum removed spectrum of the irradiation product after heating, as shown in Wong et al. (2019), is plotted in Figure 4.9 (b). The specific causes of these UV absorptions are not identified in the laboratory analysis of Poston et al. (2018), however Mahjoub et al. (2016) identify the presence of several HCOOH and $HCONH_2$ -bearing irradiation products in the infrared spectrum from the same set of experiments, suggesting that a variety of CH- and CN- bearing organics are formed which may explain the UV bands. While direct irradiation of NH_4 and CH_3OH ices is not relevant at Callisto, perhaps the irradiation of mixtures of water-ice, ammonium-bearing species, and carbonates or CO_2 can produce similar CH- and CN- bearing organics, possibly explaining the stark similarities between the 230, 320, and 450 nm absorptions seen in the laboratory irradiation product and on Callisto. While N-bearing species have not been unambiguously detected on Callisto, recent JWST observations have detected ammoniated phyllosilicates on the prograde Jovian irregular satellites Himalia and Elara which are expected to source dust, likely including NH_4-bearing compounds, that is delivered to Callisto's surface (Bottke et al., 2013; Chen et al., 2024; Sharkey et al., 2025).

Several organic molecules with absorption bands near 230 nm and 320 nm, and with a shoulder near the 275 nm edge are included in Figure 4.9 to show that organic molecules are capable of producing UV bands similar to those seen on Callisto. As

can be seen in Figure 4.9 (b), the N-bearing aromatic azobenzene (Ph−N=N−Ph) has a strong ∼320 nm absorption (Talrose et al., 2001) and the aliphatic ketone mesityl oxide ($CH_3C(O)CH{=}C(CH_3)_2$) displays a strong ∼230 nm band (Talrose et al., 2001). N-bearing aromatics like azobenzene also tend to display a second absorption, in this case near 200 nm, which could help explain Callisto's 230 nm feature. However, we do not find any clear evidence of a strong spatial correlation between Callisto's 230 and 320 nm absorption bands, suggesting a single organic subtype or formation pathway cannot fully explain both absorptions. Additionally, the spectrum of the relatively simple carboxylate ester ethyl acetate ($CH_3CO_2CH_2CH_3$) and amorphous carbon, a common product of irradiation induced carbonization of organics (e.g. Laczniak et al., 2021), are shown in Figure 4.9. Both have a strong absorption band near 200 nm which is a reasonable visual match to the 275 nm absorption edge seen predominantly on Callisto's trailing hemisphere. Amorphous carbon and other aromatic carbon rings is perhaps the simplest explanation for the 275 nm absorption edge, as we might expect the more heavily irradiated trailing hemisphere to efficiently break down (or carbonize) existing organics. This is consistent with the absence of the 320 nm band on the trailing hemisphere as well as the much weaker 4.57 μm band depth reported in Cartwright et al. (2024).

The association of Callisto's UV spectral features with organic molecules remains tentative. We have completed a thorough search through the USGS, PSF, RELAB, and SSHADE spectral libraries as well as a general literature search and have not found any other plausible spectral matches for Callisto's 320 nm absorption, perhaps strengthening the case for an organic origin. The 230 nm and 450 nm absorption bands, on the other hand, are consistent with other plausible species including NaCl and Fe-bearing silicates like serpentinite, and we do not find any strong spectroscopic evidence to prefer one explanation over the others.

280 nm Ratio Feature

The 280 nm ratio feature has been attributed to the presence of SO_2 (Lane et al., 1981; Noll et al., 1997) or a combination of SO_2, O_3, and an additional unidentified ∼300 nm band (Ramachandran et al., 2023) on Callisto's leading hemisphere. Figure 4.10 (a) shows the disk-integrated ratio spectrum of Callisto's leading to trailing hemisphere alongside the more limited wavelength coverage observation from Noll et al. (1997) and similarly constructed trailing to leading hemisphere ratios from HST/STIS observations of Europa and Ganymede. For Ganymede, the ratio spectrum reveals a relatively strong band near 255 nm which is attributed to

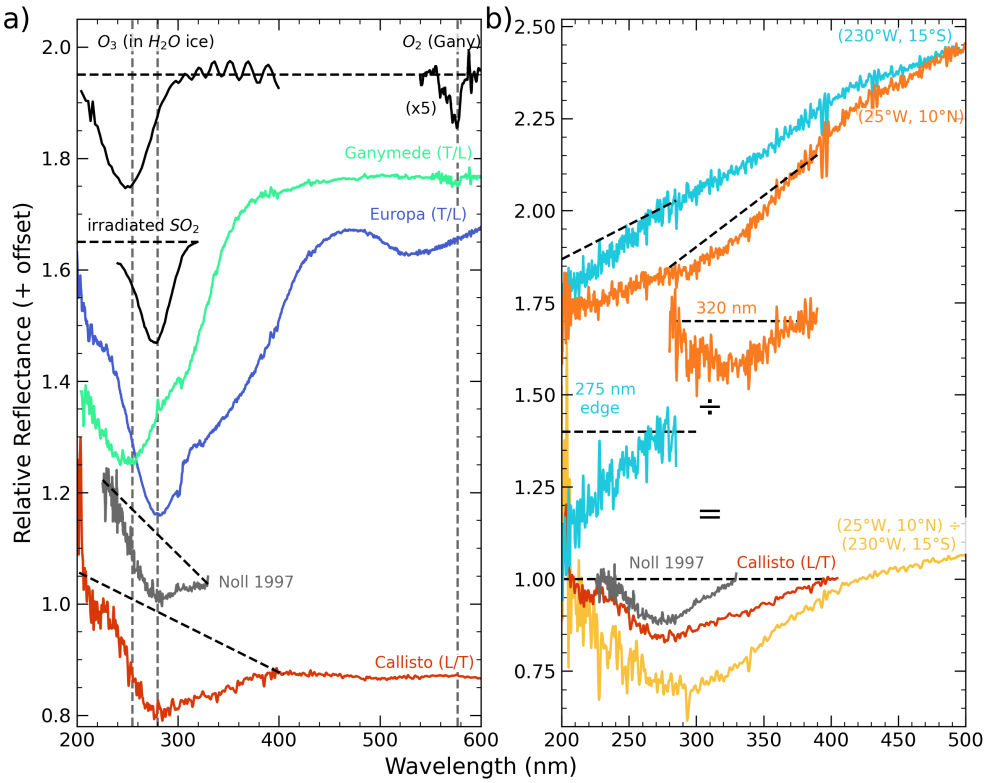

Figure 4.10: (a) Callisto's 280 nm absorption shows up in leading hemisphere spectra when ratioed against the trailing hemisphere. Europa's trailing/leading hemisphere ratio spectrum (blue) shows a clear 280 nm band which matches the laboratory spectrum of irradiated SO_2 ice that is warmed to 100 K (Ramachandran et al., 2023) and is typically attributed to SO_2 created from Iogenic sulfur implantation (Becker et al., 2022; Hendrix et al., 2011; Lane et al., 1981). Ganymede's trailing/leading hemisphere ratio spectrum (teal) shows a strong band centered at 260 nm attributed to radiolytically produced O_3 (Boduch et al., 2016; Noll et al., 1996), which also clearly matches the laboratory spectrum of O_3 in water ice from Teolis et al. (2006). The hemispherically averaged leading/trailing spectrum of Callisto (red) is compared with the observations of Noll et al. (1997) which originally attributed this band to SO_2 on the leading hemisphere. Our HST observations clearly show that the band is broader than assumed by Noll et al. (1997) and is not necessarily an obvious match to SO_2 or a combination of SO_2, O_3, and an unidentified band past 300 nm as suggested by Ramachandran et al. (2023). Instead, as demonstrated in (b) the ratio spectrum can be explained by diving a spectrum with a strong 320 nm feature, which maps predominantly to the leading hemisphere, by a spectrum with a strong 275 nm absorption edge that is constrained to the trailing hemisphere. The spectra of the two pixels which produce the deepest 280 nm ratio feature are plotted in blue and orange and their ratio (orange/blue) is shown in yellow, clearly demonstrating that the ratio of the 320 nm band/275 nm edge produces an apparent 280 nm absorption. This means that an additional absorber, like SO_2 or O_3 are not required to explain the 280 nm ratio feature and we do not find strong evidence for SO_2 on Callisto's leading hemisphere.

radiolytically produced O_3 (Boduch et al., 2016; Noll et al., 1996) and is indeed a reasonable visual match to the laboratory spectrum of O_3 in water ice (Teolis et al., 2006). The Europa ratio spectrum shows a strong band centered near 280 nm, which is attributed to the radiolytic production of SO_2 from sulfur bombardment of the trailing hemisphere (Becker et al., 2022; Hendrix et al., 2011; Lane et al., 1981) and is indeed a fair visual match to the laboratory spectrum of irradiated SO_2 ice that is subsequently warmed to 100 K (Ramachandran et al., 2023) shown in Figure 4.10 (a). While both Europa and Ganymede appear to have additional contributions to the broader UV features in their hemispherical ratio spectra, they both show a clear inset band, which is consistent with the band center and width of O_3 on Ganymede and SO_2 on Europa. Ramachandran et al. (2023) suggest that the hemispherically averaged leading to trailing ratio spectrum for Callisto, as obtained by Noll et al. (1997), can be well fit by a combination of three Gaussian's with band parameters matching SO_2, O_3, and an additional unknown absorber with a band center long-wards of 300 nm. However, as can be seen in Figure 4.10 (a), as well as the continuum removed feature shown in panel b, our HST/STIS observations reveal that the width of the 280 nm ratio feature is significantly wider than assumed from the limited wavelength coverage observations from Noll et al. (1997), and additional components on both the short and long wavelength edges would likely be required to fit this broader feature.

Laboratory experiments have shown that, at the temperatures of the Jovian satellites, SO_2 and O_3 will efficiently react making detection of these molecules in the same vicinity unlikely (Loeffler et al., 2016), and suggesting that if these species are responsible for the ratio feature, then the relative strengths of the SO_2 and O_3 absorption bands should vary across Callisto's surface. Yet, we find no evidence for any distinct absorption bands near either the O_3 or SO_2 band centers in Callisto's hemispherical ratio spectrum or in ratio spectra for any of the individual spatial pixels. We therefore suggest that Callisto's 280 nm ratio feature is unlikely to be caused by an abundance of SO_2 and O_3 on the leading hemisphere.

Instead, we suggest a simpler explanation for Callisto's 280 nm ratio feature that only involves the 320 nm absorption band and 275 nm absorption edge, which are clearly seen in individual spatial pixels and mapped in Figures 4.6 and 4.7. Spectra of the two spatial pixels that produce the largest 280 nm ratio feature ((25°W, 10°N) and (230°W, 15°S)), identified by iteratively dividing every combination of leading and trailing hemisphere pixel pairs and calculating the residual band area, are shown in

Figure 4.10 (b) along with their ratio spectrum. It is clear that the leading hemisphere pixel has a strong 320 nm absorption band and the trailing hemisphere spectrum has a strong 275 nm absorption edge. The continuum removed bands are shown below the spectra illustrating that the division of a spectrum containing a clear 320 nm absorption, which maps predominantly to the leading hemisphere (Figure 4.6 (a)) by a spectrum containing a strong 275 nm absorption edge, seen predominantly on the trailing hemisphere (Figure 4.7 (a)), can reproduce the broad feature with a 280 nm band minimum seen in Callisto's ratio spectra without requiring any additional absorptions from species like SO_2 or O_3. This is consistent with our mapped spatial distribution for the 280 nm ratio feature (Figure 4.8 (a)) and, as expected, a clear anti-correlation with the strength of the 275 nm absorption edge and positive correlation with the 320 nm band area are shown in Figure 4.8 (b) and (c). We do note, however, that while the 280 nm band is better explained by the 275 nm edge and 320 nm absorption, we cannot rule out a small additional contribution from either SO_2 or O_3.

Near-UV Downturn

A similar near-UV downturn is seen on Callisto and the other Galilean satellites—Io, Europa, and Ganymede, as well as on the Saturnian satellites and on small bodies throughout the solar system (Hendrix et al., 2018; Spencer et al., 1995; Trumbo et al., 2020, 2022b). This downturn has been attributed, at least in part, to the presence of sulfur allotropes for Io and Europa's trailing hemisphere, which is heavily bombarded by Iogenic sulfur ions (e.g. Spencer et al., 1995; Trumbo et al., 2020, 2022b). Some amount of Iogenic sulfur is likely delivered to Callisto via Jovian magnetospheric bombardment (Cooper et al., 2001; Liuzzo et al., 2019) and Cartwright et al. (2020) suggest that an absorption near 4.02 μm seen primarily on the leading hemisphere could plausibly be explained by the presence of thermally-altered sulfur allotropes from Io or from irradiation of H_2S-rich dust grains originating from Jupiter's retrograde irregular satellites. While it is plausible that sulfur-bearing species could contribute to Callisto's near-UV downturn, we find that the presence of SO_2 on Callisto's leading hemisphere is not required to explain the observed 280 nm ratio feature, suggesting that SO_2 and perhaps other sulfur-bearing species may be less abundant on Callisto than previously thought. This is consistent with the more recent JWST/NIRSpec results from Cartwright et al. (2024) who favor the hypothesis that Callisto's spectral properties are dominated by carbon, with sulfur perhaps providing only minor contributions. Additionally, recent observations of

the Jovian irregular satellites with JWST/NIRSpec show no reliable evidence for S-bearing species (Sharkey et al., 2025), likely ruling out the irregular satellites as a significant source of sulfur on Callisto. Iogenic sulfur within the Jovian magnetospheric plasma is expected to preferentially bombard Callisto's trailing hemisphere (Cooper et al., 2001; Moore et al., 2004), although recent simulations accounting for interactions between the plasma and Callisto's induced magnetic field and ionosphere suggest that the trailing hemisphere may sometimes be partially shielded from energetic ions, which are instead focused towards the sub-Jovian (0°W, 0°N) and anti-Jovian (180°W, 0°N) apexes (Liuzzo et al., 2019). The observed spatial distribution of the near-UV downturn (see Figure 4.2 (b)) does not show any particular enhancement associated with the trailing hemisphere or near the sub- and anti- Jovian apexes, suggesting that magnetospheric plasma is not likely to supply the primary material(s) responsible for the downturn. When combined with the absence of S-bearing species in the delivered irregular satellite dust, this likely rules out sulfur allotropes as a significant contributor to Callisto's near-UV downturn.

Trumbo et al. (2020) has also suggested that irradiation damaged water ice may contribute to the near-UV downturn on Europa's relatively icy leading hemisphere, although this suggestion is based on very limited available laboratory data which demonstrates a decrease in reflectance between 200 and 400 nm for irradiated water ice (Sack et al., 1991). For Callisto, it is plausible that such irradiation damaged water ice could contribute a sort of global baseline for the near-UV downturn (below 400 nm), perhaps helping to explain the relatively weak but still prominent near-UV downturn observed in the bright water-ice rich regions and the apparant slope break near 415 nm. However, the association of the strongest near-UV downturns with dark, water-poor material implies that additional species must be largely responsible for the relative differences in the strength of the near-UV downturn across Callisto's surface.

Radiation processed organics have been invoked to explain the relative strengths of the near-UV downturn in the Saturnian system (e.g. Hendrix et al., 2018). Organic molecules have long been suggested as a plausible component of the dark material on Callisto (e.g. Cartwright et al., 2024; McCord et al., 1997, 1998) and, as previously discussed, various organic species offer a plausible, although unconfirmed, spectral match to several of Callisto's UV and visible wavelength absorption features. It therefore seems likely that organic species contribute to the near-UV downturn on Callisto. Irradiation-produced tholins, as shown in Figure 4.9, provide a close visual

match to the broad downturn, especially for wavelengths short-ward of ~400 nm. However, many organic species show deep absorption bands in this wavelength range and multiple species with plausibly overlapping absorptions could also contribute to the observed downturn.

Additional species, such as many silicates and phyllosilicates which have been suggested as plausible explanations for the 450 and 930 nm absorption bands also tend to show strong downturns towards the near-UV (see e.g. serpentinite in Figure 4.9 (a)) and, if present, likely contribute to the observed downturn. Carbonates, which are commonly discussed as a likely component of Callisto's dark material, also display a near-UV downturn and may contribute to the feature on Callisto. Figure 4.9 shows the spectrum of shortite, a Na,Ca carbonate (PSF sample CRB126), which matches Callisto's near-UV downturn quite well and is otherwise generally featureless at UV-visible wavelengths. Na- and Ca- bearing carbonates have also been proposed to explain the 4.02 μm band in Callisto's NIR spectrum (Johnson et al., 2004) and our results, along with the recent analysis of JWST/NIRSpec observations by Cartwright et al. (2024), suggest that Callisto's non-H_2O spectral properties are dominated by carbon. It therefore seems likely that Callisto's near-UV downturn arises from the combination of multiple species, each with distinct absorptions in the visible and near-UV, perhaps including organics, silicates, and carbonates.

4.6 Implications for Callisto's Surface Composition

The relative contribution of endogenic and exogenic sources to the dark non-icy material which covers much of Callisto's surface is not well constrained. The two most commonly discussed end-member hypotheses are that the dark material is sourced primarily from lag deposits left behind after the ice sublimates out of endogenic ice/rock mixtures that were excavated from Callisto's subsurface by large impactors (e.g. Howard et al., 2008; Moore et al., 1999, 2004; White et al., 2016) or that the dark material is comprised almost entirely of irregular satellite dust that coats the surface in a thick layer and fills in all of the low lying regions (e.g. Bottke et al., 2013). Bottke et al. (2013) argue that the latter is more consistent with observations and suggest that a global layer of irregular satellite dust ~120 - 140 m thick should have built up on Callisto over the last ~4 Gyr. Critically, however, the estimates of Bottke et al. (2013) rely on Callisto's surface age predating irregular satellite capture, as much of the total volume of delivered dust arrives in the first ~40 Myr after the irregular satellites are captured. The slightly younger surface age (3.97-4.15 Ga) for Callisto estimated by Bottke et al. (2024), combined with the currently

favored early instability as part of the Nice model for solar system formation (e.g Liu et al., 2022; Nesvorný et al., 2018) suggests that Callisto's surface may be as much as ~600 Myr younger than the time of irregular satellite capture. Based on the simulations of Bottke et al. (2013), this could result in an order of magnitude or more decrease in the accumulated height of the irregular satellite dust on Callisto, although it is important to note that uncertainties on both of these timescales are large and the dust delivered before the final global resurfacing event reset Callisto's surface age may still be incorporated into Callisto's subsurface material.

Bottke et al. (2013) argue that the idea of a very thick ($\gtrsim$100m) layer of irregular satellite dust dominating Callisto's dark material is supported by the apparent spectral similarity between the dark material on Ganymede and Callisto and carbonaceous meteorites (CI and CM type) and asteroids (C- and D-type), as noted by multiple authors (Denk et al., 1999; Greeley et al., 2000; Hibbitts et al., 2003), and based on the expectation that the Jovian irregular satellites may be sourced from the same population as C- and D- type asteroids (e.g. Bhatt et al., 2017; Luu, 1991). JWST observations have revealed that several of the retrograde irregular satellites do indeed appear to be spectrally consistent with C- and D- type asteroids, although there is an additional unexpected population in the prograde Himalia family that is rich in ammoniated phyllosilicates and likely contributes different material to the dust falling on Callisto (Sharkey et al., 2025). However, recent observations with JWST have made it clear that Callisto's dark material is not simply a more icy spectral analog to the irregular satellites, as would be expected for a ~100 m layer of deposited dust that is mixed with relatively pure ice excavated from Callisto's subsurface (Cartwright et al., 2024; Sharkey et al., 2025). Additionally, the albedo of Callisto's darkest material is ~0.2 (Moore et al., 2004), while the albedo of the irregular satellite dust is ~0.03-0.06 (Grav et al., 2015). It is unlikely that enough water ice would be excavated and mixed into the dust to increase the albedo from 0.05 to 0.2 if all of the dark material in the 100 m layer is sourced from the irregular satellites, implying that a significant component of (less-dark) endogenic material is likely needed within the lag deposits to explain the observed albedo. The inclusion of significant amounts of dark endogenic material, perhaps rich in silicates or carbon-bearing species, within at least some of Callisto's dark lag deposits, as well as the presence of radiolytically altered species are also required to explain the distinct spatial distributions and regional variations of Callisto's UV and visible spectrum.

Based on our mapped spectral features and the results of other recent observations of Callisto (Cartwright et al., 2024) and the Jovian irregular satellites (Sharkey et al., 2025), we suggest that there are at least three separate compositional regimes within Callisto's dark material which we define as follows:

(1) material excavated by, delivered from, or altered by the Valhalla and Asgard impacts which have since been mixed with a relatively small amount of irregular satellite dust and more recently exhumed subsurface material (which itself may have been altered by the giant impact events)

(2) material of older surfaces with a relatively larger fraction of irregular satellite dust mixed with endogenic material excavated by large impacts

(3) mixtures of endogenic and exogenic material that have been radiolytically altered via magnetospheric bombardment, with the largest affects seen on the trailing hemisphere.

The most prominent UV and visible-wavelength absorption features in our spatially resolved Callisto spectra tend to display unique spatial distributions indicating that different species and material sources are responsible for each of the major absorptions, with the possible exception of the 230 and 450 nm features which may be correlated. Bottke et al. (2024) suggest that impactors only modestly larger than the impactor that formed Valhalla ($\gtrsim$60 km) may have resulted in regional or global erasure events that reset Callisto's surface early in its lifetime. It is therefore plausible that the Asgard and Valhalla impact events may have similarly reset Callisto's surface on a smaller regional scale, erasing previously built up irregular satellite dust and explaining the apparently distinct composition of the regions in and nearby the large impact basins. The terrains within and surrounding Asgard and Valhalla are the only regions with a 320 nm absorption, and there is a clear association between the basins and the 820 and 930 nm bands on Callisto's leading hemisphere. The association of these features with the impact basins implies a possible relationship with subsurface material excavated by the large impactors responsible for the basins, or material that was delivered from or altered by (e.g. via impact shock or melt) these impactors. The unique spatial distribution of the 820 and 930 nm absorptions may be more consistent with creation via impact melt, while the wider reaching 320 nm absorption implies a possible relation to impact ejecta containing material sourced from deep within the subsurface or perhaps from the giant impactors themselves. This explanation may not be consistent with the two patches of material which show relatively strong 820 and 930 nm absorptions on Callisto's trailing hemisphere as

there are no known large impact basins nearby. However, these patches are somewhat close to antipodal with Asgard and Valhalla and it is possible that a process similar to antipodal ejecta focusing thought to have occurred for several recent impacts on the moon (e.g. Bandfield et al., 2017; Wakita et al., 2021), may have deposited impact ejecta from the Valhalla and Asgard impact events onto Callisto's trailing hemisphere. Recent simulations have shown that antipodal ejecta focusing may be possible on Europa and Ganymede, perhaps even providing enough energy for secondary melt production (Gritsevich et al., 2023), however, it is unclear whether such models can be applied to Callisto's ancient giant basin-forming impacts, and future modeling work will be required to explore this hypothesis. Regardless, the spatial distributions of the 320, 820 and 930 nm absorption features are inconsistent with the patterns expected for delivery of exogenic material from irregular satellite dust or magnetospheric bombardment, and thus these features are most likely related to material either excavated from Callisto's subsurface or delivered from/altered by the Asgard and Valhalla impact events.

Assuming that the 320 nm absorption band is indeed related to organic species either delivered from, excavated by, or created during the Valhalla and Asgard forming impact events, it may be responsible for the stronger near-UV downturn (redder visible color) generally associated with the impact basins and nearby terrains. Based on the more limited spatial mapping available from JWST, Cartwright et al. (2024) find that, like the 320 nm feature, the 4.57 μm band is weaker on the trailing hemisphere. However, unlike the 320 nm feature, the authors find that the 4.57 μm band is strongest at mid-southern latitudes on the anti-Jovian hemisphere (where the 320 nm absorption is relatively weak) and weaker in and around Asgard basin (where the 320 nm feature is stronger). It is clear from their distinctly different spatial distributions that a single species or source of organics cannot be responsible for both the 4.57 μm and 320 nm absorptions. The 4.57 μm band is not seen in the spectra of the irregular satellites (Sharkey et al., 2025), and is unlikely to be a simple irradiation product of the dust as it is also not present on Ganymede (Bockelee-Morvan et al., 2024) which receives the same composition of exogenic dust, just to a lesser degree (Bottke et al., 2013; Chen et al., 2024). Taking into account the fact that Callisto maintains a strong ~2-10% 4.57 μm band depth across its surface, we suggest that the species responsible for this band is most likely formed during irradiation of mixtures of excavated endogenic material and exogenic dust, perhaps favoring a non-organic origin or requiring ammoniated species delivered by the dust as a nitrogen source if the attribution to CN-bearing organics is correct.

On the trailing hemisphere, the more intense irradiation environment may result in preferential carbonization of organic species (e.g. Hendrix et al., 2008) that produces heavily processed carbon compounds, such as amorphous carbon, with a strong 275 nm absorption edge. This simultaneously explains the presence of the 275 nm absorption edge, absence of the 320 nm band even in the potential antipode deposits, and relative weakness of the 4.57 μm feature on the trailing hemisphere, although some small steady state concentration of the 4.57 μm band material is still produced. This is consistent with the anti-bullseye distribution of the 4.57 μm feature and its apparent anti-correlation with radiolytically produced CO_2, as noted by Cartwright et al. (2024). On the leading hemisphere, our working model would suggest the regions with the strongest 4.57 μm bands correspond to older terrains which should have the largest fraction of irregular satellite dust mixed with the endogenic material. At Asgard and Valhalla, we suggest that significantly less irregular satellite dust has built up since the formation of the large impact events reset the regional surfaces. While the impact basins are ancient, perhaps ~2-4 Ga (Greeley et al., 2000), the accretion rate of the dust would have been largest early in Callisto's lifetime and most of the dust is expected to have arrived shortly after the capture of the irregular satellites (Bottke et al., 2013). A lower abundance of irregular satellite dust associated with the impact basins may explain the relative weakness of the 4.57 μm absorption on its own, although we cannot rule out the possibility that the altered material present near Asgard and Valhalla may affect the radiolytic chemistry and lead to less efficient formation of the 4.57 μm band.

The 230 nm and 450 nm absorption features may be associated with irradiated NaCl on Callisto. If so, then NaCl appears to be relatively widespread across the surface. A plausible source of NaCl is exogenic delivery associated with the neutral torus from Io. However, we do not see any obvious enhancement in the 450 nm band strength associated with the sub-Jovian quadrant of the leading hemisphere where the neutral torus is expected to deposit the most material (Cooper et al., 2001). If the NaCl is endogenic, perhaps more in alignment with the generally widespread distribution, it may be exposed from the near sub-surface by impact events and mixed into the ancient regolith, or produced during irradiation of freshly exposed native Na- and Cl- bearing species. It is interesting to note that NaCl on Europa is likely to be sputtered into the exosphere over relatively short geologic timescales (Johnson et al., 2009), requiring a recent source to explain its presence. It is unclear what the lifetime would be on Callisto, and whether the significantly less intense radiation environment alone would allow NaCl to persist on its ancient surface. Regardless of

its origin, this potential detection of NaCl on Callisto along with recent detections on Europa (Trumbo et al., 2022a, 2019b), a plausible detection of NaCl and other hydrated salts in Juno/JIRAM spectra of Ganymede (Tosi et al., 2024), and the unconfirmed speculation for Na- oxalates (or Na- sulfates) in the JWST Callisto data (Cartwright et al., 2024), suggests that Na-bearing salts may be more prevalent on surfaces throughout the Galilean system than previously thought.

We find little evidence for sulfur-bearing species in Callisto's UV-VIS spectra, perhaps suggesting that sulfur chemistry plays a less significant role in the surface composition than previously suggested (e.g. Cartwright et al., 2020; Hibbitts et al., 2000; McCord et al., 1997; Noll et al., 1997). The 280 nm ratio band does not require an additional absorber, like SO_2, to explain its presence or spatial distribution and is better explained by the presence of the 275 nm absorption edge on the trailing hemisphere and the 320 nm band on the leading hemisphere. Cartwright et al. (2020) suggest that thermally altered sulfur allotropes or HS_2 may explain the 4.02 μm absorption which is stronger on the leading hemisphere and discuss various plausible sources of sulfur at Callisto (see Cartwright et al., 2020, and references therein). However, these species are expected to show strong UV absorptions (Gosavi et al., 1973; Gradie et al., 1980; Moses et al., 1991), which we do not see in our HST observations, likely ruling out a significant contribution from sulfur allotropes or HS_2 to Callisto's NIR spectrum. The irregular satellites, whose dust has been suggested as a source of sulfur to Callisto's leading hemisphere, show no evidence of sulfur-bearing species in recent JWST observations (Sharkey et al., 2025). If the 820 and 930 nm bands are associated with sulfate species, a hypothesis we generally disfavor, this could be consistent with an endogenic source of sulfur. However, these absorptions are likely associated with impact altered material, some of which may have been delivered directly from the giant impactors themselves, and are not widespread across Callisto's surface. These bands are therefore unlikely to be related to the strong NIR features, which may or may not be associated with sulfur-bearing species.

While we do not see clear spectroscopic evidence of sulfur-bearing species on Callisto's surface, some amount of sulfur is expected to be delivered by the neutral torus and magnetospheric ion bombardment. Existing simulations and Galileo fly-by measurements suggest that Iogenic S^n ions should predominantly impact the trailing hemispheres of the icy Galilean satellites (Cooper et al., 2001). Suggestions in the literature that this pattern may be reversed at Callisto (e.g. Cartwright et

al., 2020) are largely based on the presumed presence of SO_2 and other sulfur bearing species on the leading hemisphere, although recent simulations have shown that under certain conditions the impact pattern of high energy sulfur ions may shift away from the trailing hemisphere and, in some extreme cases, preferentially bombard the leading hemisphere (Liuzzo et al., 2019). We find little observational motivation to support (or refute) any of these proposed sulfur bombardment patterns. The sulfur bombardment rate at Callisto, which is 2-3 orders of magnitude lower than at Europa (Cooper et al., 2001), may be too low to drive significant radiolytic sulfur chemistry, although the delivered sulfur must be incorporated somehow as we do not find any evidence of sulfur allotropes which typically have strong UV absorptions. Perhaps the radiolytically produced sulfur species do not strongly affect Callisto's UV-VIS spectrum or the sulfur is incorporated into the so-called carbon cycle and contribute to the UV spectral features which we suspect may be related to organic species. Alternatively, if most of the sulfur is converted to hydrated sulfuric acid (H_2SO_4), as on Europa's trailing hemisphere (Carlson et al., 2002, 1999b), and which has recently been suggested to explain a prominent 5.9 μm band on Ganymede (Bockelee-Morvan et al., 2024), then it may not significantly affect our observed HST spectrum as the ~190 nm electronic transition band of sulfuric acid (Zhou et al., 2022) is outside of our observed spectral range. Future observations, especially at far-UV and mid-IR wavelengths, will be necessary to constrain the ultimate fate of magnetospheric sulfur at Callisto.

4.7 Comparison Between Galilean Satellites

A comparison between the UV and visible spectra of the four Galilean satellites from HST/STIS is shown in Figure 4.11. The Io spectrum is from a patch of bright white sulfur-rich material on the leading hemisphere (Trumbo et al., 2022b). Average spectra of the leading and trailing hemispheres of the three icy satellites - Europa, Ganymede, and Callisto are also shown (Becker et al., 2022; Trumbo et al., 2021, 2019b, 2020). All of the hemispherically averaged satellite spectra have red slopes in the near-UV (200 - 350 nm), a steep red slope from ~400 - 500 nm, and a relatively flat or slightly red slope from ~700 - 1000 nm. All of the satellite spectra also show a strong downturn toward the near-UV, with a band edge near 500 nm, consistent with previous ground-based observations (e.g. Calvin et al., 1995; McFadden et al., 1980). This near-UV downturn appears to be somewhat more pronounced in the spectrum of Io and on Europa's trailing hemisphere than on Europa's leading hemisphere or on Ganymede and Callisto,

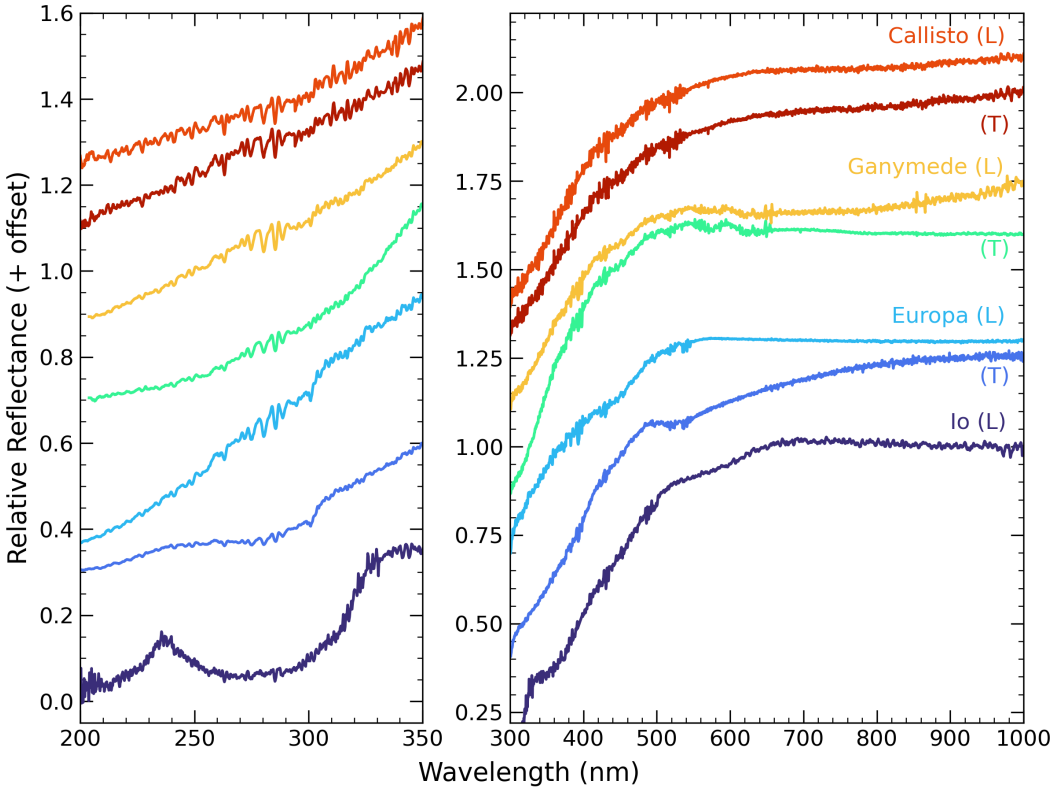

Figure 4.11: Comparison of HST/STIS UV (left) and visible (right) spectra of the leading and trailing hemispheres of Callisto, Ganymede, and Europa, and a patch of bright white (sulfur rich) material on Io's leading hemisphere. The leading and trailing averages for Europa, Ganymede, and Callisto include all UV and visible pixels within ~53 degrees of the leading and trailing points, respectively, combined to create a full 200 - 1000 nm spectrum. All spectra are normalized to 1000 nm, and offset for clarity (+0, +0.25, +0.3, +0.6, +0.75, +1, and +1.1).

likely due to an additional contribution from sulfur allotropes at Io and on Europa's trailing side (e.g. Spencer et al., 1995; Trumbo et al., 2020, 2022b). However, this near-UV downturn is ubiquitous across all of the Galilean satellites, as well as the icy Saturnian satellites (Hendrix et al., 2018), so sulfur cannot be the sole cause for all of these bodies. Hendrix et al. (2018) suggest radiation processed organics may explain the relative strengths of the near-UV downturn in the Saturnian system. As discussed in Section 4.5, it is possible that irradiation processed organics could also contribute to the near-UV downturn in the Galilean system, especially on Ganymede and Callisto. The presence of hydrated silicate minerals on Ganymede and Callisto could also contribute to the near-UV downturn, as has been proposed to explain the similar near-UV downturn short-wards of ~400 nm on hydrous meteorites and primitive asteroids (e.g. Cloutis et al., 2011a,b; Gaffey et al., 1978). Indeed, both

hemisphere spectra of Ganymede and Callisto have an apparent slope break near 400 nm, which is consistent with a contribution from multiple species to their near-UV downturn. Perhaps the presence of hydrated iron-bearing silicates within the dark material of both moons contributes to a deepening of the near-UV downturn short-wards of ~400 nm. Trumbo et al. (2020) has also suggested irradiation-damaged water as a potential explanation for the near-UV downturn on Europa's leading hemisphere, which is weaker than the trailing hemisphere where sulfur is thought to contribute. Irradiation damaged water ice could contribute to the UV absorption for all of the icy Galilean satellites, although it is likely to have the strongest contribution for Europa's leading hemisphere, where comparatively pure water ice is most abundant.

As noted in Trumbo et al. (2022b), the Io spectrum in Figure 4.11 has a strong UV SO_2 signature, with reflectance minima near 220 and 280 nm and a local maximum near 240 nm (Nash et al., 1980). This SO_2 signature is also clearly seen in the trailing hemisphere spectrum of Europa, albeit more muted, and is attributed to irradiation-produced SO_2 from Iogenic sulfur ions deposited onto Europa's trailing hemisphere by Jupiter's magnetosphere (e.g. Becker et al., 2022; Hendrix et al., 2011; Lane et al., 1981). Despite past claims of a similar SO_2 band in Callisto's leading/trailing spectral ratio (Noll et al., 1997), our analysis suggests that this feature and identification are spurious and, in reality, the consequence of dividing the unrelated 320 nm leading hemisphere band by the trailing-hemisphere 275 nm absorption edge. There is no direct evidence of a UV SO_2 signature on either hemisphere of Ganymede or Callisto.

There is also a broad absorption from ~200 - 360 nm that can be seen in Ganymede's trailing hemisphere spectrum in Figure 4.11. Noll et al. (1996) took the ratio of Ganymede's disk integrated trailing hemisphere to the leading, and attributed the observed ~260 nm feature to the O_3 Hartley band. Future studies noted that Ganymede's absorption is broadened relative to that of O_3, and an additional component attributed to SO_3^- and HSO_3^- radicals produced during sulfur implantation into oxygen rich water ice may further improve the fit to Ganymede's 260 nm absorption on the short-wavelength side (Boduch et al., 2016). An additional absorption near ~300 nm from an unidentified UV absorber may also be required to fit the long-wavelength side of Ganymede's 260 nm feature (Jones et al., 2014; Teolis et al., 2006). We note, however, that these studies relied on data which only extended to ~330 nm and our HST spectra show that the broadening of Ganymede's 260

nm absorption on the long-wavelength side actually extends out to ~360 nm (see Figure 4.10 for a ratio of Ganymede's trailing to leading hemisphere), which places the band center of this additional UV absorber closer to 320 nm. This absorption is apparent in the average trailing hemisphere spectrum of Ganymede and appears to be a close spectroscopic match to the 320 nm feature seen primarily on Callisto's leading hemisphere which we tentatively attribute to the presence of organics. We note, however, that it is difficult to determine where the short end of Ganymede's ~320 nm absorption is because it blends into the strong O_3 band, and confirmation that the feature seen on Ganymede matches Callisto's 320 nm band will require careful analysis of Ganymede's disk-resolved UV-visible spectra, which is beyond the scope of this paper. Nonetheless, it is worth considering whether the species responsible for the 320 nm absorption may be present on both Ganymede and Callisto, and that this could be the unidentified UV absorber required to fit Ganymede's broadened 260 nm feature.

Europa and Ganymede's leading hemisphere and Callisto's trailing hemisphere spectra show a drop in reflectance from ~275 nm to 200 nm which has previously been attributed to H_2O_2 (Hendrix et al., 1999). However, the 3.5 μm infrared peroxide band has only been identified on Europa's leading hemisphere and at high latitudes on Ganymede (Trumbo et al., 2023, 2019a; Wu et al., 2024). As seen in Figure 4.11, Ganymede and Callisto have very similar UV spectral slopes, and the generally equatorial distribution of the UV red material on Ganymede is inconsistent with an origin of H_2O_2. Instead, organics may dominate the reddening of the UV spectral slope at Ganymede and Callisto, as suggested by Hendrix et al. (2008). For Europa, H_2O_2 likely contributes to the reddening of the UV slope on the leading hemisphere, although an additional contribution from organics or other species cannot be ruled out.

There is a clear 577 nm absorption due to condensed O_2 in the trailing hemisphere spectrum of Ganymede, which is expected as Ganymede's O_2 is concentrated at the low- to mid-latitudes of the trailing hemisphere (Trumbo et al., 2021) and the disk-averaged trailing hemisphere absorption is ~2% (Spencer et al., 2002) A weaker absorption is also seen in the Ganymede leading hemisphere spectrum. The 577 nm O_2 absorption is not seen in the Europa or Callisto spectrum in Figure 4.9, however this is not surprising as ground-based detection suggests the 577 nm absorption is only ~0.3% deep on Europa and Callisto (Spencer et al., 2002)—at the level of the noise for these HST/STIS observations.

The Europa leading hemisphere spectrum has a broad absorption centered at 450 nm (350 to 530 nm), and a weaker UV absorption at 230 nm (200 to 260 nm) which has been attributed to irradiated NaCl in the leading hemisphere chaos terrains (Trumbo et al., 2022a, 2019b). Both the leading and trailing hemisphere spectra of Ganymede and Callisto show a weak absorption feature centered near 450 nm, which appear to be a match to the band center of Europa's 450 nm absorption, although it is difficult to determine the width and shape of the feature on either satellite due to the quickly changing continuum at the surrounding wavelengths due, at least in part, to the near-UV downturn. Additionally, a broad but weak absorption centered near 230 nm can be seen in the trailing hemisphere spectra of both Ganymede and Callisto, and plausibly, but less obviously, in the leading hemisphere spectra as well. We find that Callisto's 230 nm and 450 nm absorptions may be correlated with one another, although difficulties with mapping these features make confirmations of this impossible. Nonetheless, Callisto's absorptions are plausibly consistent with the laboratory spectra of irradiated NaCl and features detected on Europa, providing the first reported spectral evidence for the presence of NaCl on Callisto. Based on these hemispherically averaged spectra, NaCl is also a likely spectroscopic match to Ganymede's 230 nm and 450 nm features, although confirmation of this will require careful analysis of the full Ganymede data set and verification that the absorptions are spatially correlated across the surface of Ganymede as well, which is beyond the scope of this paper. However, the presence of NaCl on Ganymede is consistent with the recent plausible detection of NaCl and other hydrated salts in Juno/JIRAM spectra of Ganymede (Tosi et al., 2024).

There is a 360 nm absorption seen in the trailing hemisphere Europa spectrum which is interpreted to result from irradiation induced alteration of an unidentified endogenous species (Trumbo et al., 2020). This feature does not appear in any of the other satellite spectra, or in Europa's leading hemisphere spectrum. Additionally, a 530 nm absorption in Europa's trailing hemisphere spectrum and 560 nm absorption in the Io spectrum, commonly attributed to the presence of sulfur allotropes (e.g. Carlson et al., 2009; Spencer et al., 1997; Trumbo et al., 2020, 2022b), are not present in any of the Ganymede or Callisto spectra or on Europa's leading hemisphere.

4.8 Conclusions

We present global, spatially resolved 200 - 1000 nm spectra of Callisto obtained with HST/STIS. We use this dataset to map observed spectral features and explore possible compositions of Callisto's surface material through comparison with laboratory

samples and in the context of alteration processes known to affect Callisto's surface chemistry. We map the strength of a widespread downturn toward the near-UV and the short-wavelength NIR spectral slope from 700 to 1000 nm, which varies from slightly blue to red across Callisto's surface. At a global scale, bright water-ice-rich regions tend to have neutral or blue NIR slopes and a shallower near-UV downturn, while darker material is generally associated with red NIR slopes and stronger near-UV absorption. The strength of the 700 - 1000 nm slope does not correlate strongly with albedo differences in the dark material, but rather varies regionally with the NIR reddest slopes associated with dark material east of the Valhalla impact basin. Consistent with the hemispherical and regional color variations of dark material noted in SSI imaging, we find that global correlations between absorption features and albedo are generally weak on Callisto, but become stronger when examined regionally, suggesting that the composition of Callisto's non-ice material varies on regional scales. We find that there are at least three distinct compositional regimes for Callisto's dark material, including (1) material excavated by, delivered from, or altered by the Valhalla and Asgard impacts which have since been mixed with a relatively small amount of irregular satellite dust and exhumed subsurface material, (2) older surfaces with a relatively larger fraction of irregular satellite dust mixed with endogenic material excavated by impacts, and (3) mixtures of endogenic and exogenic material that have been radiolytically altered via magnetospheric bombardment, with the largest effects generally seen on the trailing hemisphere.

Maps of the overlapping absorption bands at 820 nm and 930 nm, which are generally found together in varying ratios, suggest a strong correlation with the Asgard and Valhalla impact basins and may be consistent with an origin from impact melt. The 930 nm absorption band may be related to an Fe-bearing silicate, most plausibly Fe^{2+}-rich phyllosilicate or a mixture of Ca-poor orthopyroxene and CM2-like phyllosilicates, or Na-bearing sulfate. The 820 nm band can possibly be explained by either a currently unidentified silicate or ferrous ammonium sulfate. Two large regions of dark material on the trailing hemisphere, not associated with any known giant impact basin, show a strong 930 nm absorption with a relatively weak 820 nm feature. We suggest that these patches may be associated with near-antipodal deposits of material from the Asgard and Valhalla impact events, although significant modeling work and a more complete understanding of the extent and composition of these patches will be necessary to confirm this hypothesis. We also map a 320 nm absorption feature which is a plausible spectral match to various unsaturated organic species and is only present in regions within and surrounding the Asgard

and Valhalla basins, perhaps hinting at an association with impact ejecta containing material from deep within the subsurface or perhaps from the giant impactors themselves. We suspect that the impact events which formed these basins may have regionally reset Callisto's surface composition, burying any irregular satellite dust which had previously been deposited in this region and resulting in comparatively less dust having accumulated near the giant basins than elsewhere on Callisto's surface. We also find that irradiation processed and carbonized organics provide a more consistent explanation for the strong 275 nm absorption edge seen on Callisto's trailing hemisphere, which had previously been attributed to H_2O_2.

We report two new absorption features near 450 and 230 nm, which may be spatially correlated, and if so are plausibly attributed to irradiated NaCl. The apparently widespread distribution of these absorptions is generally inconsistent with the delivery of Iogenic NaCl from the neutral torus, which should preferentially bombard the sub-Jovian quadrant of the leading hemisphere (Cooper et al., 2001). It is possible that Iogenic NaCl may be sputter re-deposited across Callisto's surface or that the NaCl is sourced from endogenic material excavated by impacts. Future work exploring the spatial distribution and confirming a correlation between the 230 nm and 450 nm absorption bands is necessary to confirm the presence of NaCl on Callisto. Other possible attributions include an Fe-bearing phyllosilicate like serpentinite for the 450 nm band, and various organics for either band.

We find that a 280 nm band seen only in spectra ratioed against the trailing hemisphere and previously attributed to SO_2 (Noll et al., 1997) is better explained by the presence of the 275 nm absorption edge on the trailing hemisphere and the 320 nm band which is constrained to the leading hemisphere. The presence of an additional absorber with a 280 nm band center on the leading hemisphere, like SO_2, is not required to explain this ratio band or its spatial distribution. Generally, we do not find evidence of sulfur-bearing species at UV-VIS wavelengths and suggest that the main source of sulfur at Callisto may be magnetospheric S^n ions. The sulfur bombardment rate at Callisto, which is 2-3 orders of magnitude lower than at Europa (Cooper et al., 2001), may be too low to drive significant radiolytic sulfur chemistry, or perhaps the sulfur is incorporated into organic molecules. Alternatively, existing sulfur species may not strongly affect the UV-VIS spectrum above 200 nm as might be expected for hydrated sulfuric acid.

Acknowledgments

This work is based on observations made with the NASA/ESA Hubble Space Telescope, obtained at the Space Telescope Science Institute, which is operated by the Association of Universities for Research in Astronomy, Inc., under NASA contract NAS526555. These observations are associated with program #15925. The specific observations analyzed in this paper can be accessed via `https://doi.org/10.17909/q7h0-3j07`. Support for program #15925 was provided by NASA through a grant from the Space Telescope Science Institute, which is operated by the Association of Universities for Research in Astronomy, Inc., under NASA contract NAS526555. The authors thank the anonymous referees for insightful comments and suggestions that led to an improved manuscript. MRD thanks Dr. Bethany Ehlmann, Dr. Bill Bottke, Dr. Amanda Hendrix, Dr. William Denmann, Abigail Keebler, Maria Camarca, Swaroop Chandra, Merritt McDowell, and Ashma Pandya for helpful discussions.

Facilities: HST (STIS)

BIBLIOGRAPHY

Accolla, M. et al. (2018). "Combined IR and XPS characterization of organic refractory residues obtained by ion irradiation of simple icy mixtures". *Astronomy & Astrophysics* 620, A123.

Bandfield, J. L. et al. (2017). "Distal ejecta from lunar impacts: Extensive regions of rocky deposits". *Icarus* 283, pp. 282–299.

Becker, T. M. et al. (2022). "Mid-Ultraviolet Hubble Observations of Europa and the Global Surface Distribution of SO2". *The Planetary Science Journal* 3.6, p. 129.

Bell III, J. F. and T. M. Ansty (2007). "High Spectral Resolution UV to Near-IR Observations of Mars Using HST/STIS". *Icarus* 191.2, pp. 581–602.

Bevington, P. R. and D. K. Robinson (2003). *Data Reduction and Error Analysis for the Physical Sciences*. McGraw-Hill.

Bhatt, M. et al. (2017). "Composition of Jupiter irregular satellites sheds light on their origin". *Astronomy & Astrophysics* 608, A67.

Bishop, J. L., C. M. Pieters, and M. D. Dyar (2019). "Visible and Near-Infrared Reflectance Spectroscopy". *Remote Compositional Analysis*. Ed. by J. L. Bishop, J. Bell, and J. E. Moersch, pp. 68–101.

Bockelee-Morvan, D. et al. (2024). "Composition and thermal properties of Ganymede's surface from JWST/NIRSpec and MIRI observations". *Astronomy & Astrophysics* 681, A27.

Boduch, P. et al. (2016). "Ion Processing of Ices and the Origin of SO2 and O3 on the Icy Jovian Satellites". *Icarus* 277, pp. 424–432.

Bottke, W. F. et al. (2024). "The Bombardment History of the Giant Planet Satellites". *The Planetary Science Journal* 5.4, p. 88.

Bottke, W. F. et al. (2013). "Black Rain: The Burial of the Galilean Satellites in Irregular Satellite Debris". *Icarus* 223.2, pp. 775–795.

Brown, M. E., W. T. P. Denman, and S. K. Trumbo (2022). "The Mid-UV Spectrum of Irradiated NaCl at Europa-Like Conditions". *The Planetary Science Journal* 3.2, p. 28.

Buratti, B. J. (1991). "Ganymede and Callisto: Surface Textural Dichotomies and Photometric Analysis". *Icarus* 92.2, pp. 312–323.

Burns, R. G. (1993). *Mineralogical Applications of Crystal Field Theory*. 2nd ed. Cambridge University Press.

Calvin, W. M. and R. N. Clark (1991). "Modeling the Reflectance Spectrum of Callisto 0.25 to 4.1 μm". *Icarus* 89.2, pp. 305–317.

Calvin, W. M. and R. N. Clark (1993). "Spectral Distinctions between the Leading and Trailing Hemispheres of Callisto: New Observations". *Icarus* 104.1, pp. 69–78.

Calvin, W. M. et al. (1995). "Spectra of the Icy Galilean Satellites from 0.2 to 5 μm: A Compilation, New Observations, and a Recent Summary". *Journal of Geophysical Research: Planets* 100.E9, pp. 19041–19048.

Camarca, M. et al. (2023). "Thermal Properties of the Leading Hemisphere of Callisto Inferred from ALMA Observations". *The Planetary Science Journal* 4.8, p. 142.

Carlson, R. W. et al. (2002). "Sulfuric Acid Production on Europa: The Radiolysis of Sulfur in Water Ice". *Icarus* 157.2, pp. 456–463.

Carlson, R. W. et al. (1999a). "Hydrogen Peroxide on the Surface of Europa". *Science* 283.5410, pp. 2062–2064.

Carlson, R. W. et al. (2009). "Europa's Surface Composition". *Europa*. Ed. by R. T. Pappalardo, W. B. McKinnon, and K. Khurana. University of Arizona Press, Tucson AZ, p. 283.

Carlson, R. W., R. E. Johnson, and M. S. Anderson (1999b). "Sulfuric Acid on Europa and the Radiolytic Sulfur Cycle". *Science* 286.5437, pp. 97–99.

Cartwright, R. J. et al. (2020). "Evidence for Sulfur-Bearing Species on Callisto's Leading Hemisphere: Sourced from Jupiter's Irregular Satellites or Io?" *The Astrophysical Journal* 902.2, p. L38.

Cartwright, R. J. et al. (2024). "Revealing Callisto's Carbon-Rich Surface and CO2 Atmosphere with JWST". *The Planetary Science Journal* 5.3, p. 60.

Chen, Z., K. Yang, and X. Liu (2024). "'Life' of Dust Originating from the Irregular Satellites of Jupiter". *Monthly Notices of the Royal Astronomical Society* 527.4, pp. 11327–11337.

Clark, R. N. (1980). "Ganymede, Europa, Callisto, and Saturn's Rings: Compositional Analysis from Reflectance Spectroscopy". *Icarus* 44.2, pp. 388–409.

Clark, R. N. et al. (2012). "The Surface Composition of Iapetus: Mapping Results from Cassini VIMS". *Icarus* 218.2, pp. 831–860.

Clark, R. N. and T. B. McCord (1980). "The Galilean Satellites: New Near-Infrared Spectral Reflectance Measurements (0.65–2.5 μm) and a 0.325–5 μm Summary". *Icarus* 41.3, pp. 323–339.

Cloutis, E. A. (2015). *Mineral and Rock Sample Database. Planetary Spectrophotometer Facility (PSF)*.

Cloutis, E. A. et al. (2011a). "Spectral Reflectance Properties of Carbonaceous Chondrites: 2. CM Chondrites". *Icarus* 216.1, pp. 309–346.

Cloutis, E. A. et al. (2013). “Spectral Reflectance Properties of HED Meteorites + CM2 Carbonaceous Chondrites”. *Icarus* 223.2, pp. 850–877.

Cloutis, E. et al. (2011b). “Spectral reflectance properties of carbonaceous chondrites: 1. CI chondrites”. *Icarus* 212.1, pp. 180–209.

Cloutis, E. A. et al. (2006). “Detection and discrimination of sulfate minerals using reflectance spectroscopy”. *Icarus* 184.1, pp. 121–157.

Cloutis, E. A. (2002). “Pyroxene Reflectance Spectra: Minor Absorption Bands and Effects of Elemental Substitutions”. *Journal of Geophysical Research: Planets* 107.E6, pp. 6-1–6-14.

Cooper, J. F. et al. (2001). “Energetic Ion and Electron Irradiation of the Icy Galilean Satellites”. *Icarus* 149.1, pp. 133–159.

Cruikshank, D. P. et al. (2005). “A Spectroscopic Study of the Surfaces of Saturn’s Large Satellites: H2O Ice, Tholins, and Minor Constituents”. *Icarus* 175.1, pp. 268–283.

De Sanctis, M. C. et al. (2015). “Ammoniated Phyllosilicates with a Likely Outer Solar System Origin on (1) Ceres”. *Nature* 528.7581, pp. 241–244.

Denk, T. et al. (1999). “Galileo-SSI Color Observations of the Icy Galilean Satellites during the Primary Mission: (2) Callisto and Europa”. *Lunar and Planetary Science Conference*, p. 1877.

Duley, W. (1984). “Refractive indices for amorphous carbon”. *Astrophysical Journal* 287, pp. 694–696.

Escobar-Cerezo, J. et al. (2018). “Simulations of effects of nanophase iron space weather products on lunar regolith reflectance spectra”. *The Astrophysical Journal* 853.1, p. 71.

Faure, M. et al. (2021). “A radiolytic origin of organic matter in primitive chondrites and trans-neptunian objects? New clues from ion irradiation experiments”. *Icarus* 364, p. 114462.

Gaffey, M. J. and T. B. McCord (1978). “Asteroid surface materials: Mineralogical characterizations from reflectance spectra”. *Space Science Reviews* 21, pp. 555–628.

Gavilan, L. et al. (2017). “Organic aerosols in the presence of CO2 in the early earth and exoplanets: UV–Vis refractive indices of oxidized tholins”. *The Astrophysical journal letters* 848.1, p. L5.

Gosavi, R. et al. (1973). “The UV absorption spectrum and geometry of the HS2 radical”. *Chemical Physics Letters* 21.2, pp. 318–321.

Gradie, J., P. Thomas, and J. Veverka (1980). “The surface composition of Amalthea”. *Icarus* 44.2, pp. 373–387.

Grav, T. et al. (2015). "NEOWISE: Observations of the irregular satellites of Jupiter and Saturn". *The Astrophysical Journal* 809.1, p. 3.

Greeley, R., J. E. Klemaszewski, and R. Wagner (2000). "Galileo Views of the Geology of Callisto". *Planetary and Space Science* 48.9, pp. 829–853.

Gritsevich, M. and M. Kreslavsky (2023). "Theory of Impact Ejecta Focusing in Impact Antipodal Regions". *LPI Contributions* 2806, p. 1432.

Hand, K. P. and M. E. Brown (2013). "Keck II Observations of Hemispherical Differences in H2O2 on Europa". *The Astrophysical Journal Letters* 766.2, p. L21.

Hendrix, A. R. et al. (1999). "Hydrogen Peroxide on the Icy Galilean Satellites". *Proc. 30th Lunar and Planetary Sci. Conf.* Houston: LPI.

Hendrix, A. R., C. J. Hansen, and G. M. Holsclaw (2010). "The ultraviolet reflectance of Enceladus: Implications for surface composition". *Icarus* 206.2, pp. 608–617.

Hendrix, A. R. et al. (2011). "Europa's Disk-Resolved Ultraviolet Spectra: Relationships with Plasma Flux and Surface Terrains". *Icarus* 212.2, pp. 736–743.

Hendrix, A. R., D. L. Domingue, and K. King (2005). "The Icy Galilean Satellites: Ultraviolet Phase Curve Analysis". *Icarus* 173.1, pp. 29–49.

Hendrix, A. R. et al. (2018). "Icy Saturnian Satellites: Disk-Integrated UV-IR Characteristics and Links to Exogenic Processes". *Icarus* 300, pp. 103–114.

Hendrix, A. R. and R. E. Johnson (2008). "Callisto: New Insights from Galileo Disk-Resolved UV Measurements". *The Astrophysical Journal* 687.1, pp. 706–713.

Hibbitts, C. A. et al. (2002). "CO2-Rich Impact Craters on Callisto". *Journal of Geophysical Research: Planets* 107.E10, pp. 14-1–14-14.

Hibbitts, C. A., T. B. McCord, and G. B. Hansen (2000). "Distributions of CO2 and SO2 on the Surface of Callisto". *Journal of Geophysical Research: Planets* 105.E9, pp. 22541–22557.

Hibbitts, C. et al. (2003). "Impactor contamination of dark ray craters on Ganymede". *Lunar and Planetary Science Conference*, p. 1925.

Howard, A. D. and J. M. Moore (2008). "Sublimation-Driven Erosion on Callisto: A Landform Simulation Model Test". *Geophysical Research Letters* 35.3.

Hunt, G. R. and R. P. Ashley (1979). "Spectra of Altered Rocks in the Visible and Near Infrared". *Economic Geology* 74.7, pp. 1613–1629.

Johnson, R. E. (2004). "The Magnetospheric Plasma-Driven Evolution of Satellite Atmospheres". *The Astrophysical Journal* 609.2, p. L99.

Johnson, R. E. et al. (2004). "Radiation Effects on the Surfaces of the Galilean Satellites". *Jupiter: The Planet, Satellites and Magnetosphere*. Ed. by F. Bagenal, T. E. Dowling, and W. B. McKinnon. Cambridge University Press, pp. 485–512.

Johnson, R. et al. (2009). “Composition and detection of Europa’s sputter-induced atmosphere”. *Europa* 21, pp. 507–528.

Johnson, T. V. and T. B. McCord (1970). “Galilean Satellites: The Spectral Reflectivity 0.30–1.10 Micron”. *Icarus* 13.1, pp. 37–42.

Jones, B. M., R. I. Kaiser, and G. Strazzulla (2014). “Uv-vis, infrared, and mass spectroscopy of electron irradiated frozen oxygen and carbon dioxide mixtures with water”. *The Astrophysical Journal* 781.2, p. 85.

Kalsi, P. S. (2007). *Spectroscopy of Organic Compounds*. New Age International.

Klima, R. L., C. M. Pieters, and M. D. Dyar (2007). “Spectroscopy of Synthetic Mg-Fe Pyroxenes I: Spin-Allowed and Spin-Forbidden Crystal Field Bands in the Visible and Near-Infrared”. *Meteoritics & Planetary Science* 42.2, pp. 235–253.

Kohout, T. et al. (2014). “Space weathering simulations through controlled growth of iron nanoparticles on olivine”. *Icarus* 237, pp. 75–83.

Kokaly, R. F. et al. (2017). *USGS Spectral Library Version 7*. Report 1035. Reston, VA: US Geological Survey.

Laczniak, D. et al. (2021). “Characterizing the spectral, microstructural, and chemical effects of solar wind irradiation on the Murchison carbonaceous chondrite through coordinated analyses”. *Icarus* 364, p. 114479.

Lane, A. L. and D. L. Domingue (1997). “IUE’s View of Callisto: Detection of an SO2 Absorption Correlated to Possible Torus Neutral Wind Alterations”. *Geophysical Research Letters* 24.9, pp. 1143–1146.

Lane, A. L., R. M. Nelson, and D. L. Matson (1981). “Evidence for Sulphur Implantation in Europa’s UV Absorption Band”. *Nature* 292.5818, pp. 38–39.

Liu, B., S. N. Raymond, and S. A. Jacobson (2022). “Early Solar System instability triggered by dispersal of the gaseous disk”. *Nature* 604.7907, pp. 643–646.

Liuzzo, L., S. Simon, and L. Regoli (2019). “Energetic Ion Dynamics near Callisto”. *Planetary and Space Science* 166, pp. 23–53.

Loeffler, M. J. and R. L. Hudson (2016). “What Is Eating Ozone? Thermal Reactions between SO2 and O3: Implications for Icy Environments”. *The Astrophysical Journal Letters* 833.1, p. L9.

Luu, J. (1991). “CCD photometry and spectroscopy of the outer jovian satellites”. *Astronomical Journal (ISSN 0004-6256), vol. 102, Sept. 1991, p. 1213-1225.* 102, pp. 1213–1225.

Mahjoub, A. et al. (2016). “Electron Irradiation and Thermal Processing of Mixed-Ices of Potential Relevance to Jupiter Trojan Asteroids”. *The Astrophysical Journal* 820.2, p. 141.

Marcellus, P. de et al. (2017). "Photo and thermochemical evolution of astrophysical ice analogues as a source for soluble and insoluble organic materials in Solar system minor bodies". *Monthly Notices of the Royal Astronomical Society* 464.1, pp. 114–120.

McCord, T. B. et al. (1997). "Organics and Other Molecules in the Surfaces of Callisto and Ganymede". *Science* 278.5336, pp. 271–275.

McCord, T. B. et al. (1998). "Non-Water-Ice Constituents in the Surface Material of the Icy Galilean Satellites from the Galileo near-Infrared Mapping Spectrometer Investigation". *Journal of Geophysical Research: Planets* 103.E4, pp. 8603–8626.

McDonald, G. D. et al. (1996). "Production and Chemical Analysis of Cometary Ice Tholins". *Icarus* 122.1, pp. 107–117.

McFadden, L. A., J. F. Bell, and T. B. McCord (1980). "Visible Spectral Reflectance Measurements (0.33–1.1 μm) of the Galilean Satellites at Many Orbital Phase Angles". *Icarus* 44.2, pp. 410–430.

Moore, J. M. et al. (1999). "Mass Movement and Landform Degradation on the Icy Galilean Satellites: Results of the Galileo Nominal Mission". *Icarus* 140.2, pp. 294–312.

Moore, J. M. et al. (2004). "Callisto". *Jupiter: The Planet, Satellites and Magnetosphere*. Ed. by F. Bagenal, T. E. Dowling, and W. B. McKinnon. Cambridge University Press, pp. 397–426.

Morris, R. V., D. Golden, and J. F. Bell III (1997). "Low-temperature reflectivity spectra of red hematite and the color of Mars". *Journal of Geophysical Research: Planets* 102.E4, pp. 9125–9133.

Morrison, D., N. D. Morrison, and A. R. Lazarewicz (1974). "Four-Color Photometry of the Galilean Satellites". *Icarus* 23.3, pp. 399–416.

Moses, J. I. and D. B. Nash (1991). "Phase transformations and the spectral reflectance of solid sulfur: can metastable sulfur allotropes exist on Io?" *Icarus* 89.2, pp. 277–304.

Nash, D. B., F. P. Fanale, and R. M. Nelson (1980). "SO2 Frost: UV-Visible Reflectivity and Io Surface Coverage". *Geophysical Research Letters* 7.9, pp. 665–668.

Nelson, R. M. et al. (1987). "Spectral Geometric Albedos of the Galilean Satellites from 0.24 to 0.34 Micrometers: Observations with the International Ultraviolet Explorer". *Icarus* 72.2, pp. 358–380.

Nesvornỳ, D. et al. (2018). "Evidence for very early migration of the Solar System planets from the Patroclus–Menoetius binary Jupiter Trojan". *Nature Astronomy* 2.11, pp. 878–882.

Noll, K. S. et al. (1996). "Detection of Ozone on Ganymede". *Science* 273.5273, pp. 341–343.

Noll, K. S. et al. (1997). "Detection of SO2 on Callisto with the Hubble Space Telescope". *Geophysical Research Letters* 24.9, pp. 1139–1142.

Palumbo, M., G. Ferini, and G. Baratta (2004). "Infrared and Raman spectroscopies of refractory residues left over after ion irradiation of nitrogen-bearing icy mixtures". *Advances in Space Research* 33.1, pp. 49–56.

Pieters, C. M. and T. Hiroi (2004). "RELAB (Reflectance Experiment Laboratory): A NASA Multiuser Spectroscopy Facility". *Lunar and Planetary Science Conference*, p. 1720.

Poston, M. J. et al. (2018). "Visible Near-Infrared Spectral Evolution of Irradiated Mixed Ices and Application to Kuiper Belt Objects and Jupiter Trojans". *The Astrophysical Journal* 856.2, p. 124.

Ramachandran, R. et al. (2023). "Ultraviolet Spectrum Reveals the Presence of Ozone on Jupiter's Moon Callisto". *Icarus*, p. 115896.

Rivkin, A. S. (2012). "The fraction of hydrated C-complex asteroids in the asteroid belt from SDSS data". *Icarus* 221.2, pp. 744–752.

Rivkin, A. S. et al. (2025). "Observations and Quantitative Compositional Analysis of Ceres, Pallas, and Hygiea Using JWST/NIRSpec". *The Planetary Science Journal* 6.1, p. 9.

Rizos, J. L. et al. (2019). "Spectral clustering tools applied to Ceres in preparation for OSIRIS-REx color imaging of asteroid (101955) Bennu". *Icarus* 328, pp. 69–81.

Sack, N. et al. (1991). "Alteration of the UV-visible reflectance spectra of H2O ice by ion bombardment". *Journal of Geophysical Research: Planets* 96.E2, pp. 17535–17539.

Schmitt, B. et al. (2018). "Solid Spectroscopy Hosting Architecture of Databases and Expertise". *SSHADE (OSUG Data Center)*.

Seccull, T. et al. (2018). "2004 EW95: A Phyllosilicate-bearing Carbonaceous Asteroid in the Kuiper Belt". *The Astrophysical Journal Letters* 855.2, p. L26.

Sharkey, B. N. L. et al. (2025). *JWST Reveals Varied Origins Between Jupiter's Irregular Satellites*. arXiv: 2501.16484 [astro-ph].

Singer, R. B. and T. L. Roush (1985). "Effects of Temperature on Remotely Sensed Mineral Absorption Features". *Journal of Geophysical Research: Solid Earth* 90.B14, pp. 12434–12444.

Spencer, J. R. et al. (1997). "Volcanic resurfacing of Io: Post-repair HST imaging". *Icarus* 127.1, pp. 221–237.

Spencer, J. R. and W. M. Calvin (2002). "Condensed O2 on Europa and Callisto". *The Astronomical Journal* 124.6, p. 3400.

Spencer, J. R., W. M. Calvin, and M. J. Person (1995). "Charge-Coupled Device Spectra of the Galilean Satellites: Molecular Oxygen on Ganymede". *Journal of Geophysical Research: Planets* 100.E9, pp. 19049–19056.

Talrose, V. et al. (2001). *The NIST Chemistry WebBook: A chemical data resource on the internet*. Ed. by P. J. Linstrom and W. G. Mallard. Vol. 46. ACS Publications. Chap. UV/Visible Spectra.

Teolis, B. et al. (2006). "Ozone synthesis on the icy satellites". *The Astrophysical Journal* 644.2, p. L141.

Tosi, F. et al. (2024). "Salts and Organics on Ganymede's Surface Observed by the JIRAM Spectrometer Onboard Juno". *Nature Astronomy* 8.1, pp. 82–93.

Trumbo, S. K. et al. (2022a). "A New UV Spectral Feature on Europa: Confirmation of NaCl in Leading-Hemisphere Chaos Terrain". *The Planetary Science Journal* 3.2, p. 27.

Trumbo, S. K., M. E. Brown, and D. Adams (2021). "The Geographic Distribution of Dense-Phase O2 on Ganymede". *The Planetary Science Journal* 2.4, p. 139.

Trumbo, S. K. et al. (2023). "Hydrogen Peroxide at the Poles of Ganymede". *Science Advances* 9.29.

Trumbo, S. K., M. E. Brown, and K. P. Hand (2019a). "H2O2 within Chaos Terrain on Europa's Leading Hemisphere". *The Astronomical Journal* 158.3, p. 127.

– (2019b). "Sodium Chloride on the Surface of Europa". *Science Advances* 5.6, eaaw7123.

– (2020). "Endogenic and Exogenic Contributions to Visible-Wavelength Spectra of Europa's Trailing Hemisphere". *The Astronomical Journal* 160.6, p. 282.

Trumbo, S. K. et al. (2022b). "Spectroscopic Mapping of Io's Surface with HST/STIS: SO2 Frost, Sulfur Allotropes, and Large-Scale Compositional Patterns". *The Planetary Science Journal* 3.12, p. 272.

Urso, R. G. et al. (2020). "Irradiation dose affects the composition of organic refractory materials in space-Results from laboratory analogues". *Astronomy & Astrophysics* 644, A115.

USGS Astrogeology Science Center (2013). *Callisto Galileo/Voyager Global Mosaic 1km*. `https://astrogeology.usgs.gov/search/map/Callisto/Voyager-Galileo/Callisto_Voyager_GalileoSSI_global_mosaic_1km`.

Vilas, F., K. S. Jarvis, and M. J. Gaffey (1994). "Iron Alteration Minerals in the Visible and Near-Infrared Spectra of Low-Albedo Asteroids". *Icarus* 109.2, pp. 274–283.

Wakita, S. et al. (2021). "Impactor material records the ancient lunar magnetic field in antipodal anomalies". *Nature Communications* 12.1, p. 6543.

White, O. L. et al. (2016). “Modeling of Ice Pinnacle Formation on Callisto”. *Journal of Geophysical Research: Planets* 121.1, pp. 21–45.

Wong, I. et al. (2019). “Hubble Ultraviolet Spectroscopy of Jupiter Trojans”. *The Astronomical Journal* 157.4, p. 161.

Wu, P. et al. (2024). “Europa’s H2O2: Temperature Insensitivity and a Correlation with CO2”. *The Planetary Science Journal* 5.10, p. 220.

Zhou, X. et al. (2022). “SO3 and sulfuric acid (H2SO4) aerosol detection by UV absorption spectroscopy of liquid H2SO4 solution”. *Optik* 265, p. 169522.

Chapter 5

TRITON'S WAKE: NEPTUNE'S SHATTERED INNER MOONS REVEAL ICY BODY INTERIOR COMPOSITIONS

Davis, M. R., M. Belyakov, I. Wong, Z. Milby, and M. E. Brown (2026). "Triton's Wake: Neptune's Shattered Inner Moons Reveal Icy Body Interior Compositions". Submitted to *Science Advances*.

Abstract

Neptune's single large moon, Triton, is neighbored by a set of dusty rings and small moons whose composition and origin are uncertain. Using the James Webb Space Telescope, we observed Neptune's rings and three moons: Larissa, Galatea, and Proteus. On the surfaces of these moons, we detect a compositional signature unique among outer solar system bodies: a 2.72 μm absorption band diagnostic of magnesium-rich phyllosilicates – a signpost of extensive aqueous alteration. These minerals likely formed in the subsurface of primordial satellites destroyed during Triton's violent capture or a tidally shredded dwarf planet. Our findings suggest that Neptune's present-day moons reaccreted from this deep interior material and therefore uniquely provide direct access to the interior composition of icy outer solar system differentiated bodies.

5.1 Introduction

Neptune is the only giant planet in the solar system that lacks an ordered system of large regular satellites, suggesting that it underwent a unique evolutionary pathway. More than 99% of the mass of Neptune's satellite system is dominated by Triton, with most of the remaining mass contained in a rich inner system of small close-in satellites and rings (Stone et al., 1989). Explaining and understanding the system's unusual configuration can provide clues needed to reconstruct its history. Based on its retrograde and highly inclined orbit, Triton is likely a captured Kuiper belt object (Goldreich et al., 1989). Had Neptune initially contained a system of large regular satellites, they would have been violently destroyed during Triton's capture, creating a debris disk that may have driven Triton's post-capture circularization (Banfield et al., 1992; Ćuk et al., 2005; Goldreich et al., 1989; Rufu et al., 2017). The fate of a primordial small inner satellite system following Triton's capture is uncertain; some models suggest that the small innermost moons may have survived Triton's capture or reaccreted from their own collisional debris, thus preserving much of their primordial composition (Banfield et al., 1992; Karkoschka, 2003; Li et al., 2020). Alternatively, Neptune's small inner moons may be the remnants of the originally larger regular satellites that were catastrophically disrupted (Ćuk et al., 2005; Rufu et al., 2017). Another possibility is that the inner moons and rings could be sourced from a passing Kuiper belt object (KBO) that was tidally disrupted within the planet's Roche limit sometime after Triton circularized (Charnoz et al., 2009; Crida et al., 2012; Dones, 1991).

Understanding the formation history of Neptune's inner moon and ring system requires information on their compositions. Discovered only thanks to the 1989 Voyager 2 fly-by of Neptune (Stone et al., 1989), the satellites are small and close to Neptune, making detailed study from the Earth difficult, and the compositions of these bodies and their associated rings remain largely unconstrained. Photometric observations have revealed that the moons have a strong 3-μm OH band that is weaker in the rings, which has been attributed to the presence of water ice (Belyakov et al., 2024; Hedman et al., 2025). However, the satellites' low albedos (<10%) and the survival of the innermost moons within Neptune's water ice Roche limit indicate that they must have a major contribution from dark rocky material with significant internal strength (Karkoschka, 2003; Tiscareno et al., 2013). We obtained near-infrared spectra of the small inner moons—Proteus, Larissa, and Galatea—and faint rings to explore their composition and origin. We used the integral field unit (IFU) on JWST's Near-Infrared Spectrograph (NIRSpec) in PRISM mode (0.6–5.3 μm

at R∼30–300). In the following sections, we discuss the unique composition of these moons as revealed by their spectra and the implications for the origin of the present-day Neptunian system.

5.2 Observations and Data Reduction

Proteus, Larissa, and Galatea were observed with JWST NIRSpec as part of the Cycle 3 GO Program #4645. The observations were obtained using the IFU in PRISM mode (0.6–5.3 μm, R∼30–300). Each satellite was observed multiple times and the resulting spectra were combined to achieve the highest possible S/N. The details for each observation are listed in Table 5.1. The total co-added integration times for Proteus, Larissa, and Galatea were 2334.4 s, 5514.6 s, and 8169.6 s, respectively. The ring spectra were combined from all of the observations of Larissa and all but the last dither in each set of Galatea observations, with a total integration time of 11,641.8 s.

Due to the significant scattered light from Neptune present in all of our observations, we implemented a custom reduction of the JWST data that combines the standard pipeline with our own background subtraction and extraction of the data. We used version 1.18.0 of the JWST pipeline with `jwst_1364.pmap` for calibration. We begin with the raw `.uncal` files, and run the standard Stage 1 and 2 pipeline, generating IFU cubes aligned with the detector. For Galatea and Larissa, we run the pipeline twice to generate both detector and sky-aligned data cubes.

To extract the moons Proteus, Galatea, and Larissa, we begin by masking outliers in the data cube, removing values below 0, and masking any values greater than maximum flux at the center pixel of each moon across all wavelength slices. We find this more robust than aggressive sigma-clipping, which can mask pixels with significant scattered light from Neptune. For background subtraction, we mask the target in a radius of 3 pixels, then interpolate over the masked pixels using a two-dimensional Gaussian kernel with 1.5 pixel width to obtain a rough estimate of the background. We then subtract the background from the image, and perform PSF extraction as described in (Brown et al., 2023; Wong et al., 2024). We similarly extract a solar analog spectrum from program 1128 using a 3 pixel aperture, and divide our extracted spectra by the solar analog to obtain a reflectance spectrum.

To extract the spectra of the rings, we began by determining their sky coordinates in J2000.0 right ascension and declination at the time of each of the NIRSpec observations using the SPICE toolkit (Acton, 1996). We assumed each ring was circular and

Table 5.1: Details of JWST Observations of the Inner Satellites of Neptune from program #4645. Each individual observation is listed with the target, date in UTC, total exposure time in seconds, start and end time in UTC, and central longitude (°W) and latitude (°S) of the satellite in the middle of the observation. All observations were acquired using NIRSpec/IFU in PRISM mode with the clear filter.

Target	Date	Exp. Time	Start/End Time (UTC)	Obs Sub-Lon	Obs Sub-Lat
Larissa	2024-12-13	919.1 s	16:15:24/16:30:58	55°W	21°S
Larissa	2024-12-13	919.1 s	16:33:53/16:49:26	63°W	21°S
Larissa	2024-12-13	919.1 s	16:52:07/17:07:41	72°W	21°S
Proteus	2024-12-13	291.8 s	17:40:01/17:45:07	254.5°W	24.5°S
Proteus	2024-12-13	291.8 s	17:47:48/17:52:54	256°W	24.5°S
Proteus	2024-12-13	291.8 s	17:55:49/18:00:56	257.5°W	24.5°S
Proteus	2024-12-13	291.8 s	18:03:36/18:08:43	259.5°W	24.5°S
Proteus	2024-12-16	291.8 s	13:02:12/13:07:19	74.5°W	24.5°S
Proteus	2024-12-16	291.8 s	13:09:59/13:15:06	76.5°W	24.5°S
Proteus	2024-12-16	291.8 s	13:18:01/13:23:07	78°W	24.5°S
Proteus	2024-12-16	291.8 s	13:25:48/13:30:54	80°W	24.5°S
Galatea	2024-12-17	1021.2 s	15:33:55/15:51:11	226°W	20.9°S
Galatea	2024-12-17	1021.2 s	15:53:51/16:11:07	238°W	20.9°S
Galatea	2024-12-17	1021.2 s	16:13:48/16:31:03	245°W	20.9°S
Galatea	2024-12-17	1021.2 s	16:33:44/16:51:00	261°W	20.9°S
Galatea	2024-12-19	1021.2 s	08:44:32/09:01:48	226.5°W	20.9°S
Galatea	2024-12-19	1021.2 s	09:04:28/09:21:44	238°W	20.9°S
Galatea	2024-12-19	1021.2 s	09:24:24/09:41:40	250°W	20.9°S
Galatea	2024-12-19	1021.2 s	09:44:35/10:01:51	261.5°W	20.9°S
Larissa	2024-12-20	919.1 s	01:22:28/01:38:02	236°W	21°S
Larissa	2024-12-20	919.1 s	01:40:43/01:56:16	244°W	21°S
Larissa	2024-12-20	919.1 s	01:58:57/02:14:31	252°W	21°S

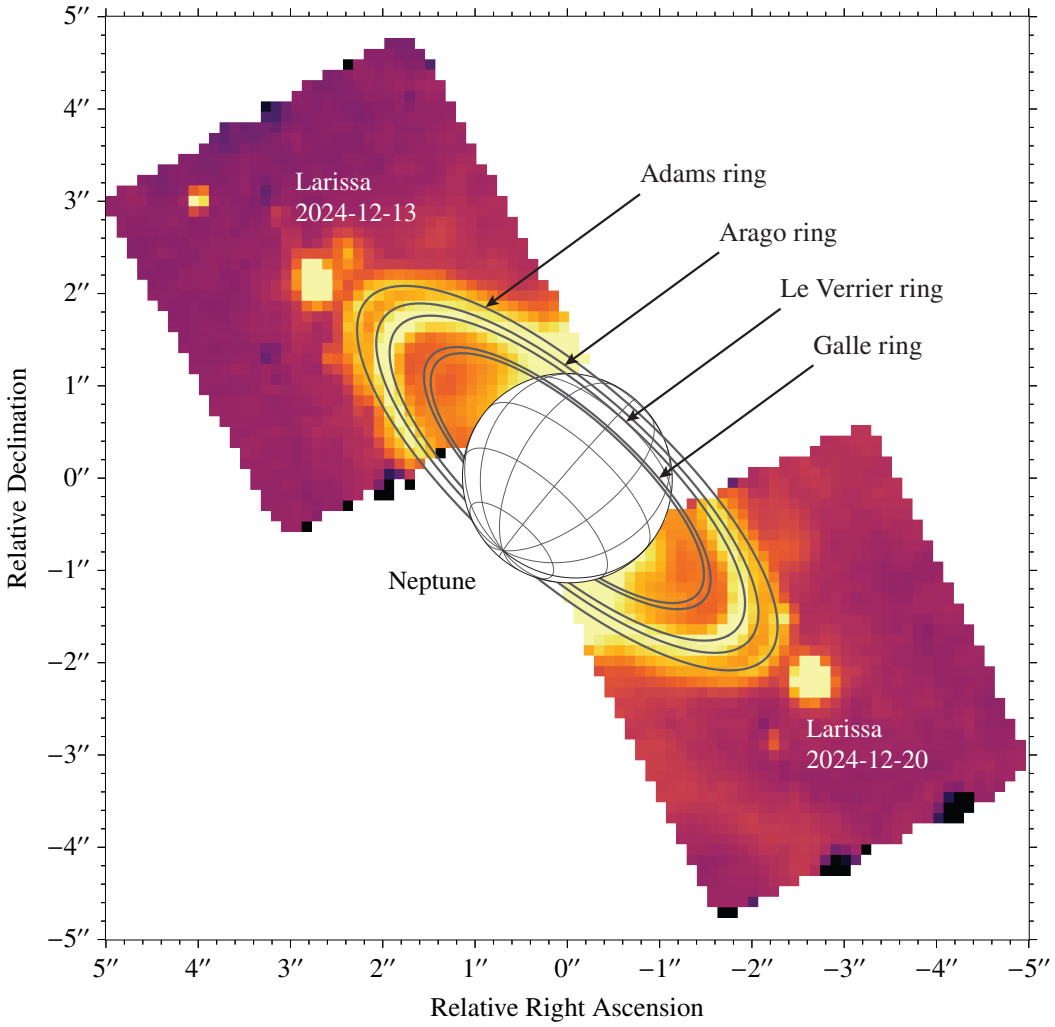

Figure 5.1: Representative JWST/NIRSpec IFU images of Larissa on 2024-12-13 and 2024-12-20 showing the locations of Neptune's rings. The IFU images were created from wavelength slices between 2.1–2.35 μm and acquired when Larissa was on opposite sides of Neptune. The bright Adams and Le Verrier rings, which are shepherded by Galatea and Despina, respectively, are easily visible in both images. The calculated ring coordinates are overlain in black.

had zero inclination. We used the semimajor axes for each ring determined during the Voyager 2 flyby on August 18, 1989 at 12:00 ET (Porco et al., 1995) and calculated the ring positions at 0.1° intervals in the body-fixed `IAU_Neptune` frame then transformed them to the J2000 inertial frame. We calculated the right ascension and declination of each ring position using the SPICE routine `recrad`, then transformed those sky coordinates to pixel coordinates using the `skycoord_to_pixel` function available in Astropy's `wcs` module (Astropy Collaboration et al., 2018, 2022, 2013). See Figure 5.1.

Using now the sky-aligned cubes described above for Larissa and Galatea, we obtain pixel coordinates from the ra/dec coordinates of the Adams, Arago, and Le Verrier ring. The locations of the rings derived for two IFU images of Larissa are shown in Figure 5.1, demonstrating the accuracy of the extracted coordinates. We mask out pixels that fall within 2.5 pixels of any of the rings or Larissa/Galatea, and interpolate with a two-dimensional gaussian kernel across the rings to estimate the background. We then subtract off the background, and find the median of each wavelength slice. The choice of specific parameters used in the reduction can cause significant changes in the data below 1.7 μm and past 4.5 μm, where scattered light from Neptune dominates the spectrum. We therefore do not show the data in those regions. The region between 1.7–4.5 μm shows a similar spectrum regardless of choice of kernel width used for smoothing and area used to measure the spectra of the rings. We select a kernel width of 1.5 pixels because it results in the visually cleanest extraction.

Raw data from all of the observations are available at the Mikulski Archive for Space Telescopes (MAST) portal under program ID 4645. The code used to generate the reduced Stage 2 background subtracted files and extracted spectra is archived at `https://data.caltech.edu/records/vwdse-4d488` (Davis et al., 2025).

5.3 Composition

The JWST/NIRSpec spectra of Neptune's rings and three of its inner moons: Proteus, Larissa, and Galatea, are shown in Figure 5.2 (a). The surfaces of Neptune's inner moons and rings are compositionally distinct from all other previously-observed outer solar system small bodies and moons. Proteus has a weak CO_2 absorption band at 4.27 μm, which is marginally stronger on the trailing hemisphere than the leading, while Larissa, Galatea, and the rings show no evidence of CO_2. These surfaces also lack a clear signature of water ice (e.g., 1.5, 1.65, 2.0, or 4.5 μm bands, or the 3.1 μm Fresnel peak), despite having very deep (~70%) and broad 3-μm OH bands. A strong hydrated mineral component is likely needed to explain the deep OH band and absent water-ice features, although no obvious spectroscopic match exists in current spectral libraries or existing observations. See the supplementary text for a more detailed discussion on the identification of the 3-μm OH stretch.

Larissa, Galatea, and the ring spectra show an unusual additional absorption on the short-wavelength side of the broader 3-μm OH stretch band. The 3-μm region of the Larissa and Galatea spectra appears very similar to Proteus, except that Proteus either

lacks or has a much weaker contribution from this additional absorption. Therefore, in order to isolate and characterize this feature, we rescale all of the spectra to have the same 3-μm band depth, and then divide the spectra of Larissa, Galatea, and the rings by Proteus' spectrum. The spectral ratios are shown in Figure 5.2 (b). These ratios reveal a sharp checkmark-shaped 2.72 μm absorption band that is characteristic of Mg-bearing phyllosilicates commonly seen on carbonaceous chondrites and main belt asteroids, which are associated with post-accretional aqueous alteration in their parent bodies (e.g. Takir et al., 2013; Zolensky et al., 1989). No similar feature has ever been detected on any body in the outer solar system past Jupiter.

We compare the 2.72 μm band on the inner moons and rings with the best-fit meteorite spectrum available in the RELAB spectral library (Pieters et al., 2004) in Figure 5.2 (b). The meteorite spectra were normalized and scaled to match the observed band depths. The 2.72 μm feature is a remarkably good match to the phyllosilicate absorption band in the Meteorite Hills (MET) 00639, Allan Hills (ALH) 84031, and Cold Bokkeveld CM2 carbonaceous chondrite spectra.

CM and CI carbonaceous chondrites are among the most primitive solar system materials that have been studied in the laboratory. They contain abundant phyllosilicates ($\gtrsim$60 vol% for CM and $\gtrsim$80 vol% for CI) which form during aqueous alteration of primary (unaltered) anhydrous silicates in their asteroid parent bodies (e.g. Howard et al., 2011; Rubin et al., 2007; Tomeoka et al., 1985; Zolensky et al., 2008, 1997). Laboratory studies show the exact band center and shape of the ~2.7–2.8 μm phyllosilicate feature trace the extent of aqueous alteration in the parent bodies of meteorites (Beck et al., 2010; Takir et al., 2013). Figure 5.2 (c) compares vacuum spectra, obtained at 150 K (Takir et al., 2013), of CM meteorites with varying degrees of alteration based on the Rubin petrologic scale (Rubin et al., 2007). The band evolves from a rounded 2.8 μm feature (Fe-serpentine; e.g., QUE 97990) to a sharp 2.7 μm "checkmark" shape (Mg-serpentine; e.g., LAP 02277) with progressive alteration (Beck et al., 2010; Takir et al., 2013, 2019). The inner Neptunian moons and rings are consistent with the Mg-serpentine dominated composition of the most aqueously-evolved CM chondrites (petrologic type CM2.0–2.1), indicating that these moons have undergone extensive and prolonged aqueous alteration.

In order to contextualize the bands seen on Larissa and Galatea, Figure 5.2 (c) also shows globally-averaged spectra of the asteroid Bennu from *OSIRIS-ReX* (Hamilton et al., 2019) and Ceres from *Dawn* (De Sanctis et al., 2015) for comparison with two well-studied bodies with significant phyllosilicate absorptions. The band on the

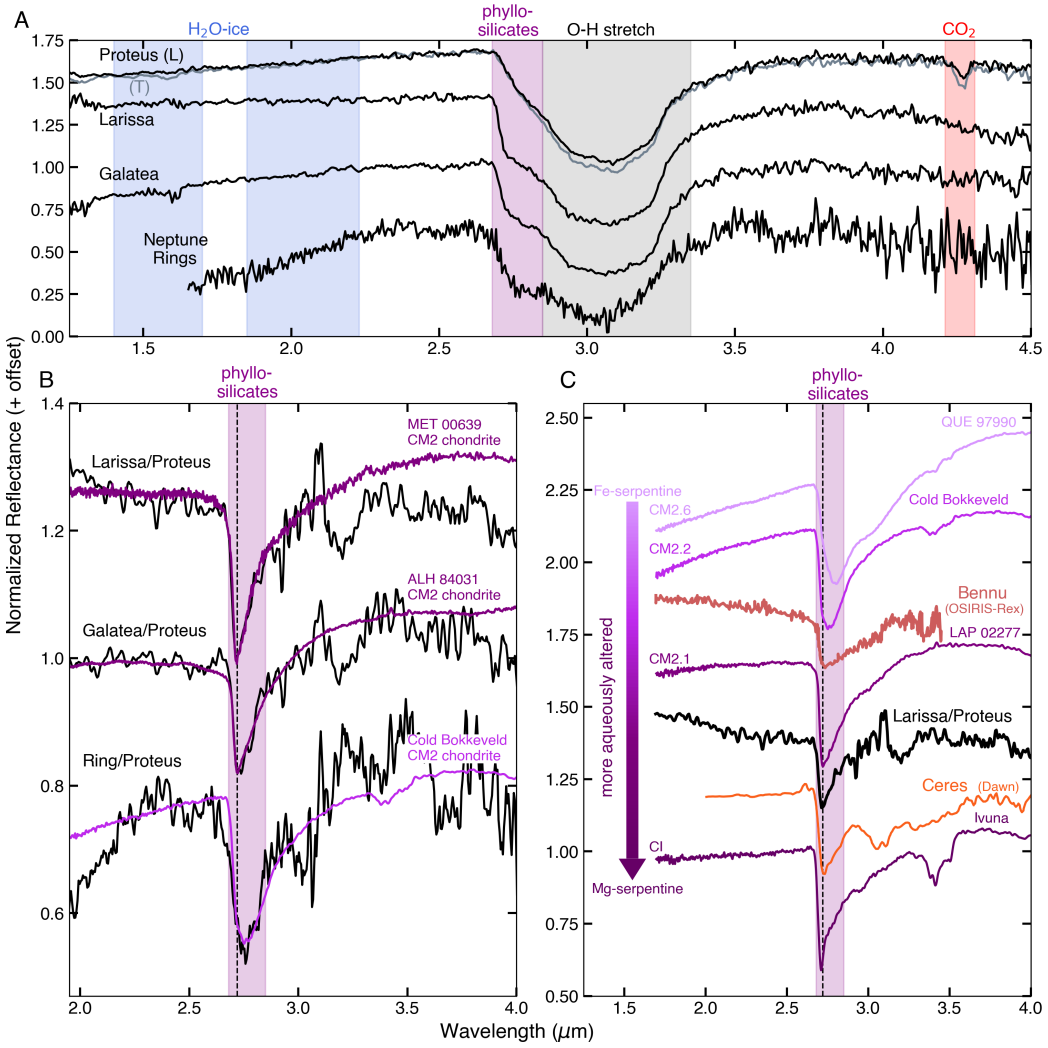

Figure 5.2: JWST/NIRSpec spectra of the inner Neptunian satellites reveal aqueously altered phyllosilicates from the deep interior of an original regular satellite. (a) Normalized reflectance spectra of Proteus, Larissa, Galatea and the average ring spectrum. Key absorption bands are highhlighted, demonstrating the deep 3 μm OH band and 2.7 μm feature, CO_2 only on Proteus, and no water-ice overtones. (b) The continuum removed 2.72 μm absorption band compared with meteorite laboratory spectra from the RELAB spectral library. The band is a close match to CM2 carbonacous chondrites. (c) Comparison with average spectra of asteroids's Bennu (Hamilton et al., 2019) and Ceres (De Sanctis et al., 2015) along with laboratory spectra of CM2 chondrites acquired under vacuum at 150 K (purple (Takir et al., 2013)) in order of increasing aqueous alteration as indicated by the Rubin petrologic scale (Rubin et al., 2007). The spectra range from the least altered Fe-serpentine dominated QUE 97990 to the most altered Mg-serpentine dominated LAP 02277 and CI chondrite Ivuna. The band on the inner Neptunian moons best matches the most altered CM2 chondrites and the largest asteroids, like Ceres.

inner Neptunian satellites is a much stronger match in both band center and shape to Ceres. Ceres experienced strong and pervasive aqueous alteration, and its measured mineralogy and geochemistry are consistent with CM/CI-like carbonaceous chondrites (McSween Jr. et al., 2018). Observations of the 2.7 μm phyllosilicate band on asteroids have been sparse due to atmospheric absorption, but recent JWST observations of the large ($\gtrsim$350 km) low-albedo outer main belt asteroids Hygiea and Pallas, along with Ceres, show that all three objects have similar Mg-rich and Fe-poor phyllosilicates (Rivkin et al., 2025). The advanced degree of aqueous alteration experienced by these bodies may be related to their size, with larger objects allowing convection of interior melt during (partial) internal differentiation which effectively increases the water-rock ratio (McSween Jr. et al., 2018). The phyllosilicate component of the inner Neptunian moons is broadly consistent with Ceres and the largest main belt asteroids, perhaps suggesting that they formed in differentiated parent bodies that are much larger than the moons' current sizes.

5.4 Origin of the Phyllosilicates

Larissa, Galatea, and the Neptunian rings contain abundant CM2-like Mg-endmember phyllosilicates that are formed by prolonged exposure ($\gtrsim$10Myr) to liquid water at moderately low temperatures ($\lesssim$300–400 K) (De Leuw et al., 2010; Fujiya et al., 2013; Zolensky et al., 1989). These aqueous conditions do not exist on any known outer solar system surfaces, and the formation of phyllosilicates requires both significant and prolonged heating. Collisions are one potential mechanism, as laboratory experiments demonstrate that shock processes can generate localized phyllosilicates on water-rich surfaces (Furukawa et al., 2011). However, the alteration timescales in the parent bodies of CM2 chondrites vastly exceed the duration of post-impact heating, and evidence of impact-induced thermal metamorphism in CM chondrites has been linked to dehydration of phyllosilicates and/or recrastallization into olivine and pyroxene (Nakamura, 2006; Rubin, 2012). The production of the observed highly aqueously evolved Mg-serpentine end-member minerology via collisions is therefore unlikely.

In situ formation of phyllosilicates within moons as small as Larissa (176 km) and Galatea (194 km) is equally implausible due to thermodynamic constraints. Interior models for Uranus' moons suggest that under most formation conditions, Miranda (470 km) will never generate enough internal heat to melt water ice and likely required a significant contribution from tidal heating to achieve differentiation (Castillo-Rogez et al., 2023). Thus, endogenous alteration can be ruled out for

Larissa and Galatea, which are approximately 2.5 times smaller than Miranda.

While aqueously altered phyllosilicates have never been detected in the outer solar system, they are likely present in the interiors of many of the large bodies that have liquid water (Castillo-Rogez et al., 2023). The most plausible reason for the detection of phyllosilicates on Larissa and Galatea is that Neptune's current inner moons are reaccreted fragments containing material from the deep interiors of large differentiated moons. In contrast, Proteus contains material that is hydrated but phyllosilicate-poor, suggesting that it either reaccreted from hydrated material that never underwent aqueous alteration or subsequently reached temperatures high enough to dehydrate the phyllosilicate phases and weaken the characteristic 2.7-μm absorption band (Che et al., 2011). We expect that any of the primordial satellites that were large enough to differentiate ($\gtrsim$500–800 km) and form phyllosilicates would have had relatively pure water-ice shells (Castillo-Rogez et al., 2023). It is therefore surprising that we find no evidence of water ice on any of the observed moons or rings and only small amounts of CO_2 on Proteus, suggesting that the reaccreted material was volatile poor or that these moons have lost most of their water ice during subsequent collisional processing. Additionally, it is unclear why the phyllosilicate-rich material preferentially accreted into Larissa and Galatea and is absent on Proteus. Perhaps the material that reaccreted into Proteus predominantly arises from large primordial satellites with a different composition than the ones from which the smaller inner satellites are sourced, although the fate of the water ice remains a mystery. It is possible that the moons have been devolatilized by impact shocks during their initial destruction or that volatiles were preferentially lost from the debris disk during Triton's circularization. Detailed investigation into the reaccretion properties of a satellite debris disk around Neptune, especially one whose lifetime may have been extended beyond typical reaccretion timescales due to repeated encounters with Triton (Zhang et al., 2008), will likely be required to better understand the distribution of materials among the inner Neptunian moons.

Another place where we may find phyllosilicates in the outer solar system is the interiors of large differentiated dwarf planets (Desch et al., 2009; Emery et al., 2024). Simulations demonstrate that the tidal shredding of a differentiated KBO could lead to the reaccretion of satellites with a relatively high silicate fraction if the KBO passes deep into Neptune's Roche limit, possibly delivering our observed phyllosilicates (Crida et al., 2012; Hyodo et al., 2017). In this scenario, anywhere from 0.1-10% of the original KBO's mass may form a ring around Neptune, consistent with a single

Pluto sized object sourcing Neptune's inner system (Hyodo et al., 2017). If the tidal shredding event occurred before Triton's capture, it is also possible that the system of original regular satellites considered above formed out of material delivered by a disrupted dwarf planet. These scenarios are therefore indistinguishable, except for the fact that the aqueous alteration may have occurred in the original dwarf planet rather than the regular satellites themselves.

5.5 Implications for the Proto-Neptunian System

The presence of phyllosilicates on Larissa and Galatea implies that at least one of Neptune's primordial moons (or precursor KBO) must have been large enough and experienced enough heating to melt ice in the interior. In contrast, these objects did not generate enough heat to completely dehydrate the Proteus-like material that has maintained a high degree of hydration, as evidenced by the very deep 3-μm OH band. Interior thermal models of Pluto suggest that it may have reached temperatures in excess of 1100 K (Robuchon et al., 2011), likely leading to the dehydration of Proteus-like material and perhaps suggesting that aqueous alteration within smaller regular satellites is more likely. The presence of abundant phyllosilcates on Larissa and Galatea also requires that the bulk of this phyllosilicate-rich material has never been heated above ~700K, including by impact shock, or the phyllosilicates would have dehydrated (Nakamura, 2006; Rubin, 2012). This means the relative speeds of the impacts that initially disrupted the primordial satellite system, as well as the subsequent collisional processing in the debris disk and after reaccretion, must have been low enough to avoid heating the bulk of the satellite material beyond these temperature limits. While the exact temperatures reached post-impact depend on numerous factors, such as the relative sizes and compositions of the impactors, the angle of impact, and the initial temperatures, these observationally derived temperature limits may inform models of the formation of Neptune's regular satellites, Triton's capture, and the subsequent evolution of the debris disk and Neptunian system.

5.6 Implications for Outer Solar System Icy Satellites

The phyllosilicates present on the inner Neptunian moons require prolonged aqueous alteration, which must have occurred in the deep interior of a large differentiated object followed by their exposure in a catastrophic event. Our observations most readily support a scenario in which the original Neptunian satellite system was destroyed during Triton's capture, and the current system reaccreted from the debris,

thereby exposing the bulk core-mantle material of the original satellites for remote sensing. While aqueous alteration in the interiors of outer solar system icy bodies has long been predicted, this material typically remains buried deep in the interiors. The inner Neptunian moons are therefore the only place in the solar system where we can directly probe the interior of an icy satellite, or possibly a dwarf planet if the aqueous alteration occurred prior to the formation of Neptune's original system. In either case, the presence of CM2-like phyllosilicates on Neptune's inner moons demonstrates that, when heated sufficiently, outer solar system materials undergo a mineralogical evolution nearly identical to that observed in main-belt asteroids. This similarity implies that the rocky components present in the inner and outer solar system during planetesimal formation must have either been inherently similar (likely requiring thorough mixing of materials across the protosolar disk) or converged toward the same geochemical end state when aqueously altered despite initial differences in Fe/Mg ratios, olivine/pyroxene proportions, and chondrite abundances (Leone et al., 2023).

Appendix

Attribution of the Broad 3-µm Feature

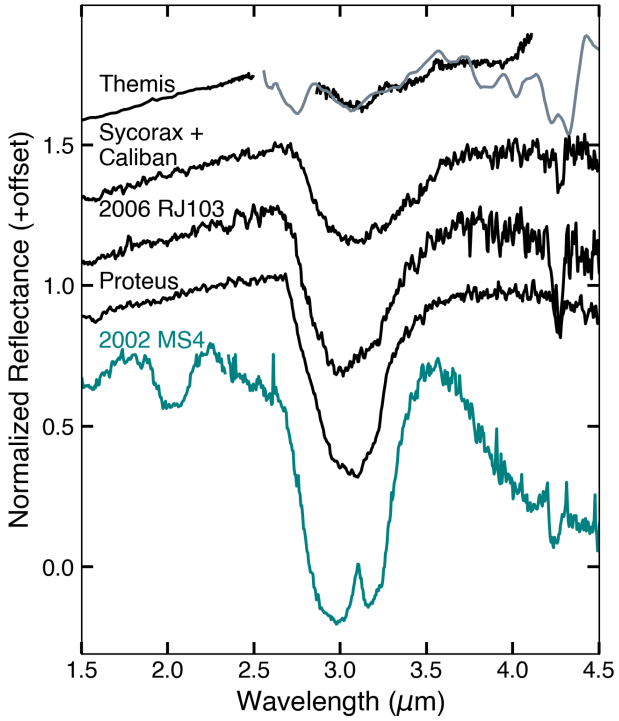

Figure 5.3: Comparison of Proteus to outer solar system bodies with 3 µm OH bands. Proteus shows an unusually deep 3 µm OH band among objects that do not show clear spectroscopic evidence of water-ice, like the Neptune Trojan 2006 RJ103 (Markwardt et al., 2025), the average spectrum of the Saturnian irregular satellites Sycorax and Caliban (Belyakov et al., 2025), and the main-belt asteroid Themis (Rivkin et al., 2010) shown here. Indeed, the band on Proteus is almost as deep as 2002 MS4, a water-ice-rich KBO with one of the deepest water bands in the observed population (Pinilla-Alonso et al., 2025).

There is no clear spectral analog for the deep 3 µm feature seen on Proteus and the other Neptunian moons in existing laboratory spectral databases including the United States Geological Survey (USGS) (Kokaly et al., 2017), Winnipeg Planetary Spectrophotometer Facility (PSF) (Cloutis, 2015), Keck/NASA Reflectance Experiment Laboratory (RELAB) (Pieters et al., 2004), and Solid Spectroscopy Hosting Architecture of Databases and Expertise (SSHADE) (Schmitt et al., 2018). Outer solar system objects with $\gtrsim$50% 3-µm band depths like water-rich KBOs (Pinilla-Alonso et al., 2025), Neptune Trojans (Markwardt et al., 2025), the regular satellites of Uranus (Brown et al., 1983; Cartwright et al., 2018), and Saturnian irregular satellite Phoebe (Belyakov et al., 2025; Clark et al., 2012) show additional spectral features associated with water and other volatile ices. Figure 5.3 shows a

comparison of Proteus' spectrum to other outer solar system objects known to have relatively deep 3 μm bands without water ice signatures, with Proteus' 70% band clearly being an outlier. For comparison, the figure also includes a water-ice-rich KBO, 2002 MS4, that has the one of the deepest 3 μm bands in the currently observed population (Pinilla-Alonso et al., 2025), which clearly correlate to strong water overtone bands at 1.5, 2 and 4.5 μm as well as a water ice Fresnell- peak near 3.1 μm.

The ~3.1 μm absorption band seen on the main belt asteroid Themis has been suggested to arise from anhydrous silicate grains coated with submicrometer-sized water ice grains, resulting in a ~10% band while suppressing the characteristic water-ice absorptions (e.g. Rivkin et al., 2010). Spectral models capable of reproducing Themis' spectrum require a very short path length for water ice to avoid observable overtone bands and are therefore unable to reproduce the deep 3-μm band seen on the Neptunian moons. For similar reasons, a coating of fine grained water ice has been dismissed as an explanation for the ~25% deep 3.1 μm band on the small Saturnian irregular satellites, Siarnaq and Albiorix (Belyakov et al., 2025). An unidentified hydrated material is the favored explanation for the somewhat similiar 3 μm absorption bands on Sycorax and Caliban as well as the unusual Neptune Trojan 2006 RJ103 (Belyakov et al., 2025; Markwardt et al., 2025). From direct spectroscopic comparison, it is uncertain whether the inner Neptunian satellites, 2006 RJ103 and small Saturnian irregular satellites may share a common hydrated mineral as the band shapes differ between these objects. Proteus' 3 μm band is closest to that of 2006 RJ103, but the Neptune Trojan lacks the 3.07 μm band minimum. However, a similar 3.1 μm band on Ceres, seperate from its broader 2.7 μm phyllosilcate band, has been attributed to ammoniation (De Sanctis et al., 2015). If ammoniated material is present on Proteus, it is possible that the same hydrated material is responsible for the broader 3 μm band on Proteus and 2006 RJ103 and the spectral differences observed near 3.1 μm are caused by ammoniation.

The acquisition of laboratory spectra of candidate materials for the unidentified hydrated minerals responsible for the unusual 3 μm OH bands seen on the inner Neptunian satellites will be necessary to understand the source of this material. It is possible that this Proteus-like material may represent relatively unaltered material from which the original Neptunian satellites accreted, perhaps deriving from smaller undifferentiated original satellites, and therefore probing the initial rocky component present in the outer solar system material that fed Neptune's protoplanetary disk.

Alternatively, this material may be highly metamorphically altered if it is sourced from the deepest and hottest part of the interiors of the original satellites. In this case, understanding the composition of the Proteus-like material may offer key insights into the composition as well as the temperature conditions—and therefore sizes—of the original differentiated satellites, as the maximum temperatures reached would have necessarily been lower than the temperature required to dehydrate this material.

The Question of Ammoniation in the Phyllosilicates

Ceres and Hygiea exhibit a 3.05–3.1 μm band attributed to ammoniated phyllosilicates, implying either: (1) formation in the outer Solar System where ammonia could condense followed by inward migration, or (2) more plausibly, accretion of ammonia-rich material (e.g. organics) that drifted inward from outer Solar System reservoirs that is only incorporated into clays in the largest objects that were heated sufficiently to release ammonia (De Sanctis et al., 2015; McSween Jr. et al., 2018; Rivkin et al., 2010). There is a weak and narrow divet near 3.07 μm in all four spectra of the Neptunian satellites and rings (Figure 5.2 (a)) which could plausibly be attributed to ammonia-bearing material. However, the band is more pronounced on Proteus than in the other three spectra, suggesting it is unlikely to be related to ammoniated phyllosilicates and consistent with an origin in a large regular satellite that was large enough to melt water-ice but which did not reach temperatures required to release ammonia. Instead, the ammonia may still be contained within the precursor outer solar system material which we expect to have been abundant at Neptune. The presence of this band in all three moon spectra, with the strongest band on Proteus, could suggest its incorporation into the hydrated material responsible for Proteus' unusual 3-μm band.

Distinguishing Between a Regular Satellite and Kuiper Belt Source

Simulations have demonstrated that the tidal shredding of a differentiated KBO could lead to the reaccretion of Neptune's inner satellites and possibly explain the observed phyllosilicates (Crida et al., 2012; Hyodo et al., 2017). However, in all but the most extreme cases, the reaccreted material should contain a significant fraction of water ice. Similarly, we expect that large regular satellites that melted water ice in their interiors would have produced water-ice rich shells, as is observed at Uranus (Castillo-Rogez et al., 2023). In either scenario, the absence of water on the inner Neptunian satellites is difficult to explain, and some mechanism of volatile loss is required. One possible alternative is the shredding of a single object

that is an order of magnitude more massive than Pluto, which simulations indicate could result in a nearly 100% silicate-dominated captured composition (Hyodo et al., 2017). However, an encounter with such an object and its initially massive debris disk is likely to have destabilized Triton (Rufu et al., 2017). It is therefore possible that, if such a shredding event preceded Triton's capture, it may have created a system of water-poor regular satellites with a total mass comparable to the current Uranian system. In this case, the primordial satellites could be silicate dominated, with hydrated phyllosilicates sourced from the interior of the shredded dwarf planet, and post-detruction volatile loss would not be necessary to explain the spectra of the present-day reaccreted moons. However, material sourced predominantly from the deep interior of a massive dwarf planet likely reached temperatures capable of dehydrating rock in a relatively large part of the interior (Robuchon et al., 2011). While the phyllosilicates may be sourced from a smaller region of mantle material, the hydrated Proteus-like material which dominates the spectrum of the current inner moons may not have survived within such a large KBO, perhaps favoring in-situ aqueous alteration within the interiors of Neptune's primordial (icy) regular satellites. A better understanding of the composition and temperature limits of the Proteus-like hydrated minerals will likely be required to differentiate between these hypotheses.

Acknowledgments

The authors thank Dr. Driss Takir for providing laboratory data used in Figure 5.2. M.R.D. thanks Dr. Josh Emery and Dr. Bethany Ehlmann for helpful discussions during the preparation of this manuscript. This study was based on observations made with the NASA/ESA/CSA James Webb Space Telescope (JWST). The data were obtained from the Mikulski Archive for Space Telescopes (MAST) at the Space Telescope Science Institute, which is operated by the Association of Universities for Research in Astronomy under NASA contract NAS 5-03127 for JWST. The observations analyzed here are associated with JWST program #4645. Support for program #4645 was provided by NASA through a grant from the Space Telescope Science Institute. The specific observations shown in this chapter can be found at `https://doi.org/10.17909/1cqh-hy49`. The code used to generate the reduced Stage 2 background-subtracted files and the extracted spectra is archived at `https://data.caltech.edu/records/vwdse-4d488` (Davis et al., 2025).

Facilities: JWST (NIRSpec)

BIBLIOGRAPHY

Acton, C. H. (1996). *Ancillary Data Services of NASA's Navigation and Ancillary Information Facility*.

Astropy Collaboration, A. M. Price-Whelan, et al. (2018). "The Astropy Project: Building an Open-Science Project and Status of the v2.0 Core Package". *The Astronomical Journal* 156.3, p. 123.

Astropy Collaboration, A. M. Price-Whelan, et al. (2022). "The Astropy Project: Sustaining and Growing a Community-Oriented Open-Source Project and the Latest Major Release (v5.0) of the Core Package". *The Astrophysical Journal* 935.2, p. 167.

Astropy Collaboration, T. P. Robitaille, E. J. Tollerud, et al. (2013). "Astropy: A Community Python Package for Astronomy". *Astronomy & Astrophysics* 558, A33.

Banfield, D. and N. Murray (1992). "A Dynamical History of the Inner Neptunian Satellites". *Icarus* 99.2, pp. 390–401.

Beck, P. et al. (2010). "Hydrous Mineralogy of CM and CI Chondrites from Infrared Spectroscopy and Their Relationship with Low Albedo Asteroids". *Geochimica et Cosmochimica Acta* 74.16, pp. 4881–4892.

Belyakov, M. and M. E. Brown (2025). "Saturnian Irregular Satellites as a Probe of Kuiper Belt Surface Evolution". *The Planetary Science Journal* 6.4, p. 97.

Belyakov, M. et al. (2024). "JWST Spectrophotometry of the Small Satellites of Uranus and Neptune". *The Planetary Science Journal* 5.5, p. 119.

Brown, M. E. and W. C. Fraser (2023). "The State of CO and CO_2 Ices in the Kuiper Belt as Seen by JWST". *The Planetary Science Journal* 4.7, p. 130.

Brown, R. H. and D. P. Cruikshank (1983). "The Uranian Satellites: Surface Compositions and Opposition Brightness Surges". *Icarus* 55.1, pp. 83–92.

Cartwright, R. J. et al. (2018). "Red Material on the Large Moons of Uranus: Dust from the Irregular Satellites?" *Icarus* 314, pp. 210–231.

Castillo-Rogez, J. et al. (2023). "Compositions and Interior Structures of the Large Moons of Uranus and Implications for Future Spacecraft Observations". *Journal of Geophysical Research: Planets* 128.1, e2022JE007432.

Charnoz, S. et al. (2009). "Did Saturn's Rings Form during the Late Heavy Bombardment?" *Icarus* 199.2, pp. 413–428.

Che, C. et al. (2011). "Spectroscopic Study of the Dehydration and/or Dehydroxylation of Phyllosilicate and Zeolite Minerals". *Journal of Geophysical Research: Planets* 116.E5.

Clark, R. N. et al. (2012). “The Surface Composition of Iapetus: Mapping Results from Cassini VIMS”. *Icarus* 218.2, pp. 831–860.

Cloutis, E. A. (2015). *Mineral and Rock Sample Database. Planetary Spectrophotometer Facility (PSF)*.

Crida, A. and S. Charnoz (2012). “Formation of Regular Satellites from Ancient Massive Rings in the Solar System”. *Science* 338.6111, pp. 1196–1199.

Ćuk, M. and B. J. Gladman (2005). “Constraints on the Orbital Evolution of Triton”. *The Astrophysical Journal* 626.2, p. L113.

Davis, M. R. et al. (2025). *Reduction Code for Inner Neptunian Satellite Paper*.

De Leuw, S., A. E. Rubin, and J. T. Wasson (2010). “Carbonates in CM Chondrites: Complex Formational Histories and Comparison to Carbonates in CI Chondrites”. *Meteoritics & Planetary Science* 45.4, pp. 513–530.

De Sanctis, M. C. et al. (2015). “Ammoniated Phyllosilicates with a Likely Outer Solar System Origin on (1) Ceres”. *Nature* 528.7581, pp. 241–244.

Desch, S. J. et al. (2009). “Thermal Evolution of Kuiper Belt Objects, with Implications for Cryovolcanism”. *Icarus* 202.2, pp. 694–714.

Dones, L. (1991). “A Recent Cometary Origin for Saturn’s Rings?” *Icarus* 92.2, pp. 194–203.

Emery, J. P. et al. (2024). “A Tale of 3 Dwarf Planets: Ices and Organics on Sedna, Gonggong, and Quaoar from JWST Spectroscopy”. *Icarus* 414, p. 116017.

Fujiya, W. et al. (2013). “Mn–Cr Ages of Dolomites in CI Chondrites and the Tagish Lake Ungrouped Carbonaceous Chondrite”. *Earth and Planetary Science Letters* 362, pp. 130–142.

Furukawa, Y. et al. (2011). “Impact-Induced Phyllosilicate Formation from Olivine and Water”. *Geochimica et Cosmochimica Acta* 75.21, pp. 6461–6472.

Goldreich, P. et al. (1989). “Neptune’s Story”. *Science* 245.4917, pp. 500–504.

Hamilton, V. E. et al. (2019). “Evidence for Widespread Hydrated Minerals on Asteroid (101955) Bennu”. *Nature Astronomy* 3.4, pp. 332–340.

Hedman, M. M. et al. (2025). *Spectral Trends across the Rings and Inner Moons of Uranus and Neptune from JWST NIRCam Images*. arXiv: 2506.18650 [astro-ph].

Howard, K. T. et al. (2011). “Modal Mineralogy of CM Chondrites by X-ray Diffraction: Part 2. Degree, Nature and Settings of Aqueous Alteration”. *Geochimica et Cosmochimica Acta* 75.10, pp. 2735–2751.

Hyodo, R. et al. (2017). “Ring Formation around Giant Planets by Tidal Disruption of a Single Passing Large Kuiper Belt Object”. *Icarus* 282, pp. 195–213.

Karkoschka, E. (2003). “Sizes, Shapes, and Albedos of the Inner Satellites of Neptune”. *Icarus* 162.2, pp. 400–407.

Kokaly, R. F. et al. (2017). *USGS Spectral Library Version 7*. Report 1035. Reston, VA: US Geological Survey.

Leone, G. and H. K. M. Tanaka (2023). "Igneous Processes in the Small Bodies of the Solar System I. Asteroids and Comets". *iScience* 26.7, p. 107160.

Li, D. and A. A. Christou (2020). "The Origin of Neptune's Unusual Satellites from a Planetary Encounter". *The Astronomical Journal* 159.4, p. 184.

Markwardt, L. et al. (2025). *From Colors to Spectra and Back Again: First Near-IR Spectroscopic Survey of Neptunian Trojans*. arXiv: 2310.03998 [astro-ph].

McSween Jr., H. Y. et al. (2018). "Carbonaceous Chondrites as Analogs for the Composition and Alteration of Ceres". *Meteoritics & Planetary Science* 53.9, pp. 1793–1804.

Nakamura, T. (2006). "Yamato 793321 CM Chondrite: Dehydrated Regolith Material of a Hydrous Asteroid". *Earth and Planetary Science Letters* 242.1, pp. 26–38.

Pieters, C. M. and T. Hiroi (2004). "RELAB (Reflectance Experiment Laboratory): A NASA Multiuser Spectroscopy Facility". *Lunar and Planetary Science Conference*, p. 1720.

Pinilla-Alonso, N. et al. (2025). "A JWST/DiSCo-TNOs Portrait of the Primordial Solar System through Its Trans-Neptunian Objects". *Nature Astronomy* 9.2, pp. 230–244.

Porco, C. C. et al. (1995). "Neptune's Ring System". *Neptune and Triton*. Ed. by D. P. Cruikshank. The University of Arizona Space Science Series. University of Arizona Press.

Rivkin, A. S. and J. P. Emery (2010). "Detection of Ice and Organics on an Asteroidal Surface". *Nature* 464.7293, pp. 1322–1323.

Rivkin, A. S. et al. (2025). "Observations and Quantitative Compositional Analysis of Ceres, Pallas, and Hygiea Using JWST/NIRSpec". *The Planetary Science Journal* 6.1, p. 9.

Robuchon, G. and F. Nimmo (2011). "Thermal Evolution of Pluto and Implications for Surface Tectonics and a Subsurface Ocean". *Icarus* 216.2, pp. 426–439.

Rubin, A. E. (2012). "Collisional Facilitation of Aqueous Alteration of CM and CV Carbonaceous Chondrites". *Geochimica et Cosmochimica Acta* 90, pp. 181–194.

Rubin, A. E. et al. (2007). "Progressive Aqueous Alteration of CM Carbonaceous Chondrites". *Geochimica et Cosmochimica Acta* 71.9, pp. 2361–2382.

Rufu, R. and R. M. Canup (2017). "Triton's Evolution with a Primordial Neptunian Satellite System". *The Astronomical Journal* 154.5, p. 208.

Schmitt, B. et al. (2018). "Solid Spectroscopy Hosting Architecture of Databases and Expertise". *SSHADE (OSUG Data Center)*.

Stone, E. C. and E. D. Miner (1989). "The Voyager 2 Encounter with the Neptunian System". *Science* 246.4936, pp. 1417–1421.

Takir, D. et al. (2013). "Nature and Degree of Aqueous Alteration in CM and CI Carbonaceous Chondrites". *Meteoritics & Planetary Science* 48.9, pp. 1618–1637.

Takir, D. et al. (2019). "3-μm Reflectance Spectroscopy of Carbonaceous Chondrites under Asteroid-Like Conditions". *Icarus* 333, pp. 243–251.

Tiscareno, M. S. et al. (2013). "Compositions and Origins of Outer Planet Systems: Insights from the Roche Critical Density". *The Astrophysical Journal Letters* 765.2, p. L28.

Tomeoka, K. and P. R. Buseck (1985). "Indicators of Aqueous Alteration in CM Carbonaceous Chondrites: Microtextures of a Layered Mineral Containing Fe, S, O and Ni". *Geochimica et Cosmochimica Acta* 49.10, pp. 2149–2163.

Wong, I. et al. (2024). "JWST Near-Infrared Spectroscopy of the Lucy Jupiter Trojan Flyby Targets: Evidence for OH Absorption, Aliphatic Organics, and CO2". *The Planetary Science Journal* 5.4, p. 87.

Zhang, K. and D. P. Hamilton (2008). "Orbital Resonances in the Inner Neptunian System: II. Resonant History of Proteus, Larissa, Galatea, and Despina". *Icarus* 193.1, pp. 267–282.

Zolensky, M. E., W. L. Bourcier, and J. L. Gooding (1989). "Aqueous Alteration on the Hydrous Asteroids: Results of EQ3/6 Computer Simulations". *Icarus* 78.2, pp. 411–425.

Zolensky, M. E., A. N. Krot, and G. Benedix (2008). "Record of Low-Temperature Alteration in Asteroids". *Reviews in Mineralogy and Geochemistry* 68.1, pp. 429–462.

Zolensky, M. E. et al. (1997). "CM Chondrites Exhibit the Complete Petrologic Range from Type 2 to 1". *Geochimica et Cosmochimica Acta* 61.23, pp. 5099–5115.

Chapter 6

CONCLUSIONS AND FUTURE DIRECTIONS

The surfaces of icy satellites represent the integrated outcome of their formation environments, geologic histories, and billions of years of competing processes—endogenic emplacement, exogenic delivery, and irradiation-driven chemistry—all operating simultaneously across a vast range of spatial and temporal scales. Interpreting what a surface spectrum is actually telling us about the body beneath it, or the system it inhabits, requires disentangling these contributions with care. This thesis has pursued that goal across three systems spanning Jupiter to Neptune, using multi-wavelength spectroscopy to probe not only the surface composition and distribution of materials across these moons, but the processes that shape these surfaces and the histories they encode.

What Europa's Surface Does—and Does Not—Tell Us About Its Ocean

Europa remains one of the most compelling targets for astrobiological study in the solar system. Its deep subsurface ocean is likely in direct contact with a silicate seafloor, a configuration favorable to the chemical disequilibria required to sustain life, and the geologically young chaos terrains, bands, and ridges on its young surface represent potential windows into that ocean's chemistry. And yet, the work in this thesis along with the broader scope of the literature demonstrates that the composition of Europa's geologically active regions and its relation to the ocean must be interpreted with considerable caution.

Chapters 2 and 3 of this thesis addressed processes operating on Europa's trailing hemisphere, where the exogenic irradiation environment is most intense. Chapter 2 showed that the 2.07 μm absorption feature on the trailing hemisphere, previously proposed to arise from irradiated endogenic Mg-bearing salts—either in the form of sulfate salts like epsomite (Brown et al., 2013) or magnesium chlorate/perchlorate (Ligier et al., 2016)—shows no spatial association with the large scale chaos terrains where oceanic material is expected to reside and where other spectral features associated with radiolytically altered endogenic species are found (e.g. Trumbo et al., 2020). Instead, the distribution of this 2.07 μm feature tracks the irradiation bullseye associated with the radiolytic sulfur cycle, although it is absent from the young Pwyll crater ejecta, pointing toward a radiolytic origin independent of any

endogenic Mg-bearing salt component. Na and K ions have been detected in Europa's exosphere (e.g. Brown, 2001; Brown et al., 1996) and likely originate from sputtered surface salts, providing indirect evidence for Na- and K- bearing salts of oceanic origin, and irradiated NaCl has now been spectroscopically confirmed in the leading hemisphere chaos terrains (e.g. Trumbo et al., 2022, 2019). Mg, however, has no analogous atmospheric detection—upper limits on the Na/Mg ratio rule out a meteoritic or cosmic abundance of atmospheric Mg (Hörst et al., 2013)—and the surface remains the only plausible window into whether Mg-bearing species are present. The presence or absence of Mg in Europa's ocean matters considerably: in relatively simple freezing models, a Mg-rich ocean implies lower pH and a distinct cation balance compared to a purely Na- and K-chloride system (Johnson et al., 2019). By showing that the 2.07 μm band may not be a reliable tracer of irradiated endogenic Mg-chloride, Chapter 2 removes what had been the most prominent proposed spectroscopic handle on the Mg content of Europa's ocean, leaving its abundance essentially unconstrained by current observations.

Chapter 3 reinforces the picture of a powerful radiation environment, but reveals that it may operate at a much slower rate than previously assumed: Pwyll and Manannán craters are depleted in hydrated sulfuric acid relative to the background terrain, placing a lower bound of $\gtrsim$2–4 Myr on the equilibrium timescale of H_2SO_4 production in the radiolytic sulfur cycle. This is several orders of magnitude longer than estimates derived from laboratory irradiation experiments (Carlson et al., 2002; Ding et al., 2013; Strazzulla, 2011), a discrepancy that likely reflects fundamental limitations in extrapolating single-particle, short-timescale (and thus high fluence) laboratory experiments to the complex, multi-particle irradiation environment at Europa and to geologic timescales over which competing production and destruction processes, as well as possible thermal contributions, operate. Together, the results from Chapters 2 and 3 underscore that the trailing hemisphere surface is substantially overprinted on timescales relevant to the crater record, and that interpreting its spectroscopy requires carefully accounting for this irradiation history before any ocean-derived signal can be isolated.

Since the work in Chapters 2 and 3 was originally published, the JWST era has brought a complementary and striking perspective from the leading hemisphere, where the irradiation environment is comparatively shielded. JWST/NIRSpec observations have revealed that CO_2 is concentrated within the leading hemisphere chaos terrains—consistent with an internally derived source of carbon (e.g. Trumbo

et al., 2023). More recently, higher abundances of crystalline water ice has been found to be co-located within these same chaos terrains, which Cartwright et al. (2025) suggest as evidence that these regions might be refreshed on timescales short enough to outpace irradiation-driven amorphization. These results reinforce a picture in which the chaos terrains are the most chemically active and ocean-connected regions of Europa's surface, and they sharpen the significance of the constraints established in this thesis. The carbon-bearing species detected by JWST within the leading hemisphere chaos terrains may be related to a radiolytic carbon cycle that is broadly analogous to the sulfur cycle operating on the trailing hemisphere, and the orders-of-magnitude discrepancy between laboratory-derived radiolytic timescales and the observational constraints from Chapter 3 has direct relevance for interpreting these observations. If the carbon cycle operates on similarly long timescales as the sulfur cycle—as suggested by the apparent survival of relatively unaltered endogenic material in the young leading hemisphere chaos—then JWST may be observing carbon-bearing species that still closely reflect the composition of the material emplaced from the interior. Conversely, if the carbon cycle reaches equilibrium on shorter timescales, the observed CO_2 and associated species may already be substantially altered from their original form. Understanding what the chaos terrains are telling us about the ocean therefore requires knowing not just what species are present, but how long they have had to be altered. The geologic-based stratigraphy approach of Chapter 3 offers the only existing observational method capable of constraining these timescales, and extending this methodology to the carbon cycle—for instance through observations of young impact features on the leading hemisphere—represents a natural and important next step.

Taken together, the Europa chapters of this thesis establish an important point about the relationship between Europa's surface and its ocean: the radiolytic processes that overprint the surface operate on timescales that can be far longer than laboratory experiments suggest, meaning that surfaces younger than a few million years may still retain a relatively unaltered record of the material emplaced from the interior. These results highlight the importance of establishing a nuanced framework for extracting ocean chemistry from surface observations: spectral features must be evaluated not only for their spatial associations but also for their consistency with the timescales of the processes that produce and destroy them. Applying this framework to the growing JWST dataset—and eventually to the high-spatial-resolution observations of Europa Clipper—will be essential for assembling a complete picture of the chemistry of an ocean that remains otherwise beyond reach.

Callisto as a Window into Ancient Solar System Materials

Chapter 4 turns to a body at the opposite extreme of geologic activity. Callisto's surface has been shaped by ~4-4.5 billion years of impact cratering, sublimation-driven modification, exogenic dust delivery, and magnetospheric bombardment, but has experienced no endogenic resurfacing or geologic alteration. Callisto therefore offers a fundamentally different kind of interpretive challenge. Rather than disentangling recent geologic activity from irradiation driven alteration, the question is whether a surface this ancient and thoroughly processed by exogenic inputs can still tell us something about the material that Callisto and the rest of the Jovian system accreted from the proto-Jovian disk.

The first near-global, spatially resolved UV-visible spectral maps of Callisto presented in Chapter 4, reveal a more compositionally heterogeneous surface than previous datasets suggested. The surprising variance in the spatial distributions of the mapped features argue against the simplest version of the hypothesis that Callisto's dark material is dominated by a thick ($\gtrsim$100 m) uniform blanket of irregular satellite dust (Bottke et al., 2013). If the dark non-ice material were simply deposited dust mixed with excavated water ice, one would expect its spectral properties to vary primarily with the dust-to-ice ratio—that is, with albedo—and to show patterns consistent with the known delivery mechanisms of irregular satellite material and radiolytic alteration. Instead, the spectral features reveal at least three compositionally distinct regimes: material associated with the Valhalla and Asgard impact basins, likely reflecting deep subsurface material excavated by those basin-forming events; older surfaces with mixed endogenic and exogenic contributions; and trailing-hemisphere material plausibly related to irradiation-processed carbonized organics. Two previously unreported absorption features near 230 and 450 nm are also identified, which are plausibly consistent with the color center absorptions produced by irradiated NaCl—the same species detected in Europa's leading hemisphere chaos terrains (Trumbo et al., 2022, 2019). If confirmed, this would extend NaCl as a spectral signature to a third Galilean satellite, alongside evidence for the same species on Ganymede (Tosi et al., 2024), suggesting that Na- and Cl- bearing salts may be a relatively common component of Galilean satellite surfaces. A re-examination of the 280 nm absorption feature in Callisto's leading/trailing hemisphere ratio spectra, long attributed to SO_2 (Noll et al., 1997), demonstrates that this band is better explained as a geometric consequence of dividing the 320 nm leading-hemisphere absorption by the 275 nm trailing-hemisphere absorption edge, without invoking SO_2 or any additional absorbing species. This has

implications for the sulfur budget at Callisto: previously proposed sulfur-bearing species may be considerably less abundant than assumed, with the observed spectral properties instead dominated by a carbon-rich chemistry shaped by impacts and irradiation.

The broader implication of the work in Chapter 4 is that Callisto's dark material is not a simple proxy for irregular satellite composition, nor is it a pure record of primordial disk material. It is a complex palimpsest of endogenic (potentially primordial) material, exogenic delivered dust, and radiolytically altered species, and the spatial distributions of its spectral features provide leverage for separating these contributions in ways that disk-integrated or low-spatial-resolution observations could not. In particular, the association of the 320 nm and 820/930 nm features with the Asgard and Valhalla basins—with no corresponding signature in the spatial patterns expected for dust or magnetospheric bombardment—points to the giant impacts themselves as a major contributor to the regional surface composition, perhaps by resetting the dust accumulation clock and exposing deep subsurface material that has not been available to spectroscopic observation anywhere else in the Galilean system.

A Catastrophically Different Evolutionary Path at Neptune

Chapter 5 moves to the outermost giant planet, where the satellite system tells a profoundly different story. Neptune's inner moons—Proteus, Larissa, and Galatea—were the targets of JWST/NIRSpec observations that reveal a compositional signature with no analog among previously observed outer solar system bodies: a sharp 2.72 μm absorption band diagnostic of magnesium-rich phyllosilicates, indicative of extensive and prolonged aqueous alteration. CM2 carbonaceous chondrite-like Mg-serpentine minerals of this type require sustained exposure to liquid water at moderate temperatures ($\lesssim$300–400 K) for durations of at least ~1-10 Myr (De Leuw et al., 2010; Fujiya et al., 2013; Zolensky et al., 1989)—conditions that are thermodynamically impossible within objects as small as Larissa (176 km) or Galatea (194 km). Interior models indicate that even Miranda at 470 km likely never achieved full internal melting without significant tidal heating (Castillo-Rogez et al., 2023). The phyllosilicates therefore cannot have formed in the present-day moons, nor via impact shock, and must instead have originated in the deep interiors of much larger precursor bodies with enough internal heat to melt incorporated ice. The most natural interpretation is that Neptune's current inner moons are reaccreted fragments of a primordial satellite system disrupted during the capture of Triton—itself

a Kuiper belt object on a retrograde, inclined orbit that could not have formed in place (Goldreich et al., 1989). In this scenario, the original large regular satellites were catastrophically destroyed, producing debris from which the present-day inner moons eventually reaccreted (Ćuk et al., 2005; Rufu et al., 2017). The detection of Mg-phyllosilicates on the surfaces of Larissa and Galatea means that this reaccretion process incorporated material from deep within those original differentiated moons. Neptune's inner moons therefore occupy a unique position in solar system exploration: they are the only known objects where the deep interior composition of a large differentiated icy satellite is directly accessible to remote sensing. The alternative scenario—tidal shredding of a large Kuiper belt object within Neptune's Roche limit (Crida et al., 2012; Hyodo et al., 2017)—cannot be fully excluded, in which case the aqueous alteration would have occurred in the interior of the disrupted body rather than in regular satellite precursors. In either case, the fundamental conclusion stands: the present-day surface spectra of Neptune's ring-moons directly sample material formed through interactions with liquid-water in the interior of an object far larger than any of the moons themselves.

The contrast between the Neptune system and the Galilean satellites illuminates a broader point about the diversity of evolutionary pathways among the outer solar system's icy satellite systems. At Jupiter, Europa and Callisto bracket the spectrum of geologic activity among the Galilean satellites, yet both surfaces are substantially shaped by exogenic processes that complicate the extraction of primordial or endogenic signals. At Neptune, the evolutionary path has been more extreme: the entire original regular satellite system was almost certainly obliterated, and the current inner moons are second-generation objects formed from the ruins of the first. This history is spectroscopically legible in the phyllosilicate signature—it is precisely because the original satellites were destroyed and their interiors exposed that remote sensing can access material that would otherwise remain permanently buried. No equivalent access exists for the Galilean satellites, whose interiors—though likely also containing hydrated silicates—remain sealed beneath intact icy shells. More broadly, the results of Chapter 5 suggest that the mechanisms by which satellite systems form and evolve around the ice giants may be far less ordered than around Jupiter and Saturn, and that the spectroscopic record preserved in the surfaces of small, disrupted moons can serve as a direct probe of processes—differentiation, aqueous alteration, catastrophic disruption—that are otherwise inaccessible to observation.

Toward a Broader Picture: Diversity and Divergence in Icy Satellite Systems

The results across all four chapters, taken together, point toward a picture of icy satellite systems that is considerably more diverse—and more historically contingent—than simple formation models would predict. In the Jovian system, Europa and Callisto bracket the spectrum of geologic activity among the icy Galilean satellites, yet both surfaces are substantially shaped by exogenic processes that can obscure the endogenic signals one might hope to read. Comparison between the two bodies reinforces that surface composition reflects not just the initial state of a satellite but the integrated record of everything that has happened since—and that different moons, even at the same heliocentric distance, accumulate those records very differently.

At Neptune, the evolutionary path has been more extreme still. The assumption that regular satellites form in orderly, co-planar circumplanetary disks with their host planets—the standard model for Jupiter's Galilean moons (e.g. Canup et al., 2002)—may not be universal. The ice giant systems appear to have undergone far more chaotic evolutionary pathways. Triton's retrograde capture at Neptune almost certainly erased whatever original satellite system existed (Rufu et al., 2017); and among the large Uranian moons, several lines of evidence point to their potential formation from collisional or tidal reshaping events rather than a simple primordial formation history (e.g. Crida et al., 2012; Ida et al., 2020). The spectroscopic detection of Mg-phyllosilicates on Neptune's inner moons in Chapter 5 provides direct observational evidence that this disruption reached to the deep interiors of differentiated bodies—bodies that must themselves have been at least as large as the present-day Uranian moons. Neptune, at least, did not grow its satellite system once and keep it: the current configuration is the outcome of catastrophic reprocessing.

Furthermore, the compositional convergence between the phyllosilicate-rich inner Neptunian moons and the most aqueously altered main-belt asteroids, despite the vast difference in their heliocentric distances and formation environments, implies that the rocky building blocks present across the protoplanetary disk underwent similar geochemical transformations when heated and hydrated. The solar system's compositional diversity at the surface level obscures a deeper uniformity in the mineralogy of aqueously processed rocky material—a uniformity that may reflect either thorough early mixing of material across the disk, or the convergence of different precursor compositions toward similar geochemical endpoints under aqueous alteration.

Open Questions and Future Directions

This work naturally raises a number of questions that remain open. At Europa, the identity of the 2.07 μm carrier species remains unknown, and its absence at young Pwyll crater places a firm lower limit on the timescale of its formation. Laboratory irradiation experiments at Europa-relevant temperatures, particle energies, and candidate material mixtures—including combined sulfur radiolysis and magnetospheric electron bombardment—are needed to identify plausible products. The multi-order-of-magnitude discrepancy between the observationally constrained sulfuric acid equilibrium timescale ($\gtrsim$2–4 Myr) and laboratory estimates ($\sim 10^4$ yr) suggests that the radiolytic timescales for all of the potential cycles (e.g. radiolytic carbon cycle, color center production) operating across Europa's surface may differ significantly from their laboratory derived estimates. Future analyses targeting different radiolytic products may provide critical observational constraints on these timescales.

For Callisto, the proposed identifications of the UV and visible wavelength absorption bands all require validation through cryogenic laboratory spectra at Callisto-relevant conditions. More broadly, decades of UV-through-near-IR observations have yet to yield unambiguous compositional identifications for Callisto's dark non-ice material, suggesting that laboratory work alone may be insufficient and that extending observations into unexplored wavelength regimes—particularly the mid-infrared, where the fundamental absorption bands of candidate silicate, carbonate, and organic species lie—may be necessary to make definitive progress on its composition. Whether or not a similar 320 nm organic absorption feature exists on Ganymede, as tentatively suggested by the hemispherically averaged STIS data, and if they share the same origins will require careful analysis of the full Ganymede dataset.

At Neptune, the unidentified hydrated mineral responsible for the broad 3 μm OH band is a high priority for future laboratory work. The acquisition of reflectance spectra of candidate highly hydrated materials at low temperatures may help constrain whether the Proteus-like component that is ubiquitous across the observed satellites represents relatively pristine outer solar system material or heavily metamorphosed deep interior rock. Additionally, there are a large number of open questions about how the process of satellite destruction and reaccretion might proceed in an environment that continues to be perturbed by Triton until its orbit has fully circularized. Detailed modeling work of this process, heat transport and

material-dependent trajectories during the destruction of an initial system, and the evolution of the satellite debris through accretion of the inner system may be critical for constraining the initial state of Neptune's satellites and explaining the puzzling lack of water-ice observed on these moons today.

The diversity of satellites and systems studied in this thesis collectively illustrate that the surfaces of icy satellites are neither simple nor static records of their formation environments. They are the product of histories that are often violent, always complex, and in many cases still ongoing. Disentangling these histories through spectroscopy requires not only better observations, but a clearer understanding of the timescales, pathways, and physical conditions under which the processes shaping these surfaces operate. The coming decade, with JWST continuing to reveal the chemistry of outer solar system surfaces in unprecedented detail, Europa Clipper beginning its close-up reconnaissance of Europa's surface, and the prospect of a dedicated mission to the Uranian system, offers an extraordinary opportunity to bring that understanding within reach both within and across the satellite systems of the giant planets.

BIBLIOGRAPHY

Bottke, W. F. et al. (2013). "Black Rain: The Burial of the Galilean Satellites in Irregular Satellite Debris". *Icarus* 223.2, pp. 775–795.

Brown, M. E. and K. P. Hand (2013). "Salts and Radiation Products on the Surface of Europa". *The Astronomical Journal* 145.4, p. 110.

Brown, M. E. (2001). "Potassium in Europa's Atmosphere". *Icarus* 151.2, pp. 190–195.

Brown, M. E. and R. E. Hill (1996). "Discovery of an Extended Sodium Atmosphere around Europa". *Nature* 380.6571, pp. 229–231.

Canup, R. M. and W. R. Ward (2002). "Formation of the Galilean satellites: Conditions of accretion". *The Astronomical Journal* 124.6, pp. 3404–3423.

Carlson, R. W. et al. (2002). "Sulfuric Acid Production on Europa: The Radiolysis of Sulfur in Water Ice". *Icarus* 157.2, pp. 456–463.

Cartwright, R. J. et al. (2025). "JWST reveals spectral tracers of recent surface modification on Europa". *The Planetary Science Journal* 6.5, p. 125.

Castillo-Rogez, J. et al. (2023). "Compositions and Interior Structures of the Large Moons of Uranus and Implications for Future Spacecraft Observations". *Journal of Geophysical Research: Planets* 128.1, e2022JE007432.

Crida, A. and S. Charnoz (2012). "Formation of Regular Satellites from Ancient Massive Rings in the Solar System". *Science* 338.6111, pp. 1196–1199.

Ćuk, M. and B. J. Gladman (2005). "Constraints on the Orbital Evolution of Triton". *The Astrophysical Journal* 626.2, p. L113.

De Leuw, S., A. E. Rubin, and J. T. Wasson (2010). "Carbonates in CM Chondrites: Complex Formational Histories and Comparison to Carbonates in CI Chondrites". *Meteoritics & Planetary Science* 45.4, pp. 513–530.

Ding, J. J. et al. (2013). "Implantation of Multiply Charged Sulfur Ions in Water Ice". *Icarus* 226.1, pp. 860–864.

Fujiya, W. et al. (2013). "Mn–Cr Ages of Dolomites in CI Chondrites and the Tagish Lake Ungrouped Carbonaceous Chondrite". *Earth and Planetary Science Letters* 362, pp. 130–142.

Goldreich, P. et al. (1989). "Neptune's Story". *Science* 245.4917, pp. 500–504.

Hörst, S. M. and M. E. Brown (2013). "A Search for Magnesium in Europa's Atmosphere". *The Astrophysical Journal Letters* 764.2, p. L28.

Hyodo, R. et al. (2017). "Ring Formation around Giant Planets by Tidal Disruption of a Single Passing Large Kuiper Belt Object". *Icarus* 282, pp. 195–213.

Ida, S. et al. (2020). “Uranian satellite formation by evolution of a water vapour disk generated by a giant impact”. *Nature Astronomy* 4.9, pp. 880–885.

Johnson, P. V. et al. (2019). “Insights into Europa’s Ocean Composition Derived from Its Surface Expression”. *Icarus* 321, pp. 857–865.

Ligier, N. et al. (2016). “VLT/SINFONI Observations of Europa: New Insights into the Surface Composition”. *The Astronomical Journal* 151.6, p. 163.

Noll, K. S. et al. (1997). “Detection of SO2 on Callisto with the Hubble Space Telescope”. *Geophysical Research Letters* 24.9, pp. 1139–1142.

Rufu, R. and R. M. Canup (2017). “Triton’s Evolution with a Primordial Neptunian Satellite System”. *The Astronomical Journal* 154.5, p. 208.

Strazzulla, G. (2011). “Cosmic Ion Bombardment of the Icy Moons of Jupiter”. *Nuclear Instruments and Methods in Physics Research Section B: Beam Interactions with Materials and Atoms* 269.9, pp. 842–851.

Tosi, F. et al. (2024). “Salts and Organics on Ganymede’s Surface Observed by the JIRAM Spectrometer Onboard Juno”. *Nature Astronomy* 8.1, pp. 82–93.

Trumbo, S. K. et al. (2022). “A New UV Spectral Feature on Europa: Confirmation of NaCl in Leading-Hemisphere Chaos Terrain”. *The Planetary Science Journal* 3.2, p. 27.

Trumbo, S. K. et al. (2023). “Hydrogen Peroxide at the Poles of Ganymede”. *Science Advances* 9.29.

Trumbo, S. K., M. E. Brown, and K. P. Hand (2019). “Sodium Chloride on the Surface of Europa”. *Science Advances* 5.6, eaaw7123.

– (2020). “Endogenic and Exogenic Contributions to Visible-Wavelength Spectra of Europa’s Trailing Hemisphere”. *The Astronomical Journal* 160.6, p. 282.

Zolensky, M. E., W. L. Bourcier, and J. L. Gooding (1989). “Aqueous Alteration on the Hydrous Asteroids: Results of EQ3/6 Computer Simulations”. *Icarus* 78.2, pp. 411–425.